Perpendicular Transport and Electromechanical Properties of Graphitic Composites and Multilayers

Taylor-Harrod, Isaac

Award date:
2019

Awarding institution:
University of Bath

PERPENDICULAR TRANSPORT AND ELECTROMECHANICAL PROPERTIES OF GRAPHITIC COMPOSITES AND MULTILAYERS

Isaac Taylor-Harrod

A thesis presented for the degree of Doctor of Philosophy

Department of Physics
University of Bath

August 2018

Declaration of authorship

I am the author of this thesis, and the work described therein was carried out by myself personally, with the exception of contributions noted in the acknowledgements.

Candidate's signature:

Abstract

This thesis presents several milestones in the production of flexible electronics utilising quantum tunnelling between graphitic carbon. Two such materials are investigated. The first is a composite material consisting of conducting highly oriented pyrolytic graphite particles embedded in an insulated polydimethylsiloxane (PDMS) matrix. This is referred to as a graphite silicone composite (GSC). The second is a multilayer stack of two graphene electrodes with adsorbed organic molecules (naphthalene diimide-pyridine) between them forming a tunnelling barrier.

The piezoresistive response of GSCs is analysed by applying calibrated stress steps and observing the resistance response of the composite over time. We then fit this response to a tunnelling percolation model, followed by the extraction of material parameters of viscoelastic creep time and tunnel barrier height using the fit. We also investigate the dependence of the piezoresistance of GSCs and similar composites on material parameters using this model. The flexible tunnelling percolation model allows for the effects of perturbations on composites to be predicted without the need to simulate the 3D locations of conducting particles.

To avoid the limitations of GSCs such as viscoelastic delays, we develop a multilayer stack device. This allows us to study a single graphene/insulator/graphene junction in place of a statistical average over a percolation network. We use a new synthesis method utilising thermal deposition and self-release layer graphene transfer to create these devices. This allows for the adsorbed molecules to remain on the graphene and bind together. The IV curves of these devices are tested with varying gate voltage applied to the sample, using two different sample sizes and at 77 and 300 K. The samples demonstrate a tunnelling current that decreases with negative gate voltage and decreasing sample size. Samples at 77 K see higher tunnelling currents.

Acknowledgements

First, I would like to thank my supervisor, Prof Alain Nogaret, for his advice and guidance throughout this project, as well as providing a theory to aid in modelling of the composite strain results.

I would also like to thank Dr Ashok Chauhan for his assistance in learning LabVIEW, loan of old samples and encouraging, endlessly positive attitude.

I am grateful to Dr G. Dan Pantos and Dr Giles Prentice, for fabrication of the naphthalene-diimide molecules and explanation of the chemistry background.

Thanks are also due to Saleh Altarifi for assisting in synthesis and measurement of the multilayer devices.

I am thankful to Dr Mattia Cattelan at the University of Bristol for carrying out the XPS measurements on our samples.

I thank the technical staff in the Department of Physics, in particular Paul Reddish for building the rigs used in experiments and Wendy Lambson for assistance with chemicals. I also thank Dr Stephen Wedge for teaching me how to use the clean room machines for fabrication.

Finally, I would like to thank my family and friends for supporting me through this.

Contents

Chapter 1

Introduction

1.1 Motivation

There is a growing requirement for flexible electronic devices with varying properties. The uses of flexible electronics vary, with examples such as ultra-thin, bendable screens and sensitive skins. For many uses, such as robotic limbs or SONAR-capable coatings, sensitive skins may need to detect pressure applied to them. The sensitivities required are equal to or better than that of human skin. Such requirements for flexible electronics are beyond the capabilities of current silicon technology due to its rigidity. A possible solution is to use rigid silicon electronics integrated with flexible parts, however the flexibility of such a device is limited by the size of the rigid parts, potentially preventing conformal contact with surfaces. Further, the rigid parts create weaknesses in the structure while a mixed device is bent. However, numerous new materials are being designed and created to achieve these requirements. These include composites of graphite and silicone rubber [1], graphene and nanocellulose nanopaper [2], graphene on flexible substrates [3–5] and graphene membranes suspended above cavities [6]. This thesis explores the properties of two such materials: a flexible two phase

composite and a thin multilayer stack of graphene and functionalised naphthalene diimide.

This thesis first details experimental data exploring the piezoresistance of composite materials over time, followed by detailing and fitting to a theory to explain these findings and assist in the creation of future composite materials. The composite used experimentally and modelled is composed of conductive highly oriented pyrolytic graphite (HOPG) particles randomly embedded in an insulating silicone matrix. Throughout the thesis, this product is referred to as a graphite silicone composite (GSC). Unlike previous works analysing the piezoresistance of composite materials, a fast initial spiking response is observed and used in addition to a slower change in resistance [1], allowing for quicker measurements [7]. Previous work done at low temperatures on this GSC has shown it to exhibit a negative differential resistance (NDR) region not present at or above 206 K. [8,9] Rigid models for tunnelling percolation exist and are able to explain the electronic properties of composites in a rest state. [10–12] However, to allow for accurate use of the piezoresistive properties of this composite, it is necessary to gain an understanding of the properties of flexible tunnelling percolation networks and their dynamic response to outside strain perturbations. This includes clarifying the role of bilayer strain and determining both the rise time of the initial resistance response and the timescale of the following resistance decay. This thesis aims to gain new knowledge by comparing the resistance response over time of GSCs with varying graphite filling fractions in response to the application of calibrated stress increments.

Another issue hindering the use of composites of this type as piezoresistors is the lack of a dynamic theory of resistance change in response to a stress perturbation. Static models for the percolation conductivity within a composite exist [13–15], but are insufficient for values that vary with both time and perturbations, due to their nature not

accounting for time. A theory modelling composites as tunnelling percolation networks and utilising an effective medium approximation is fitted to the experimental results of the GSC. This is useful as it allows us to extract material parameters and predict the piezoresistive response of sensors to arbitrary deformation. The first aim of this is to extract key composite parameters such as the tunnelling barrier height between conducting particles and the viscoelastic relaxation time of the composite. The second aim is to allow prediction of composite piezoresistance properties with varying parameters, aiding with the design of future composite materials.

Due to the less desirable physical properties of the GSC material; mainly the slow piezoresistive decay with time and the necessity for a low temperature to enable the NDR region; a new device is constructed and tested. The device is smaller with the aim of studying the properties of individual tunnelling bonds. This device uses a similar principle of tunnelling between carbon conductors, but through an insulating barrier between two graphene electrodes in a nanofabricated multilayer. A similar device based on a graphene and hexagonal boron nitride stack designed by Britnell *et al* [16] was designed to exhibit an NDR region through resonant tunnelling. Piezoresistance is aimed to be achieved by using a flexible insulating barrier. This barrier is formed by using two layers of molecules with a naphthalene diimide core, which can bond to graphene via π-π stacking, and pyridine moieties, which can rotate relative to the core. Building this structure required alterations to existing nanofabrication techniques. While there have been multiple previous piezoresistive devices utilising graphene, to our knowledge there are none using either the tunnelling between layers or exhibiting NDR regions. A common existing approach is the stretching of a single layer of graphene, either in continuous area [3] or utilising the tunnelling between crystals [4, 5].

1.2 Thesis overview

This thesis has been divided into 6 chapters. Chapter 1 introduces the motivations and materials used. Chapter 2 introduces relevant background theory for the remaining chapters. Details about the materials, models and phenomena explored are explained. The fabrication and experimentally observed properties of the GSC materials are described in Chapter 3. Chapter 4 derives a model for resistance change within composites starting from the strain calculated in Chapter 3 and an effective medium approximation. The predictions of the model are then detailed and compared with experimental results. The fabrication of the multilayer device is described in Chapter 5 followed by results examining the device's IV curves. Chapter 6 gives final conclusions and plans for potential future work to develop the materials further.

1.3 Papers and presentations

The work detailed in this thesis has contributed to two published papers, one paper in preparation and two poster presentations. The papers are: Ultrafast pressure sensing with transient tunnelling currents by Ashok S. Chauhan, Isaac Taylor-Harrod, Samuel D. Littlejohn, and Alain Nogaret, published in Nanoscale [7]; and Piezoresistance of flexible tunneling-percolation networks by Isaac Taylor-Harrod and Alain Nogaret, published in Physical Review B [17]. Posters were presented at the GW4 Nanofabrication Workshop in 2017 and the Frontiers in Condensed Matter Physics Conference 2018. Both were authored by I. Taylor-Harrod, S. Altarifi, M. Cattelan, G. D. Pantos and A. Nogaret.

Chapter 2

Materials and background theory

This chapter will focus on background information relevant to the remaining chapters in the thesis. It will start with a brief description of carbon and its relevant allotropes, followed by details on quantum tunnelling. These are then combined with an overview of composite materials to detail tunnelling percolation networks. The following two sections explain effective medium approximations (EMAs) and negative differential conductance respectively. The final section then details the calculations for stress and strain used in chapters 3 and 4.

2.1 Carbon

Carbon is found in a vast variety of different states from the proteins that make up life to a number of different pure carbon forms. Different allotropes of carbon can have widely varying properties, from soft and conductive graphite to hard and insulating diamond. This is due to its electronic structure allowing it to form multiple different types of bonds through hybridisation of electron orbitals. As carbon is the

sixth element in the periodic table, it has six electrons. This results in a ground state with 2 electrons of different spin in both the 1s and 2s states and 1 electron in 2 of the 3 possible 2p states. When the 2s state is excited to give a third 2p electron, carbon has all 4 outer orbitals half-full. This allows the orbitals to hybridise in 3 different ways; referred to as sp hybridisation, sp^2 hybridisation and sp^3 hybridisation. [18, 19]

Sigma, σ, bonds are present in both sp^2 hybridisation and sp^3 hybridisation, with four identical σ bonds present in sp^3 hybridisation, while sp^2 hybridisation consists of three σ bonds and a delocalised electron in a pi, π, bond. The bonds in sp hybridisation are bonds to two nearest neighbours and consist of a single and a triple bond, with both containing a σ bond and the triple bond being surrounded by two π bonds. [18, 19] The four σ bonds in sp^3 hybridisation result in tetrahedral structures such as diamond, while the chain-like bonds in sp hybridisation form structures such as carbynes or hydrocarbon polymers. [19,20] The structures formed by sp^2 hybridised carbon can be arranged in different ways. These include graphene, graphite, fullerenes and carbon nanotubes. Graphite and graphene are relevant to the content of this thesis and are covered in more detail in Sections 2.1.1 and 2.1.2. In both cases, the carbon is arranged hexagonally in one or more basal planes. Although not entirely accurate, both carbon nanotubes and fullerenes can be thought of as graphene sheets rolled into either tubes or spheres respectively.

2.1.1 Graphite

Graphite is the most common allotrope of carbon with sp^2 hybridisation. Graphite consists of multiple stacked basal planes, with each layer consisting of carbon atoms covalently bonded to their three nearest neighbours in a hexagonal lattice. These layers are bonded together arranged parallel to each other by van der Waals interactions. The most common stacking order of these layers is ABAB as shown in Figure

2.1(a) and (c). [19, 21] This is known as hexagonal graphite and is the thermodynamically stable form of graphite and is found in all graphite materials. It can be detected using X-ray diffraction. [21] A second stacking order, ABCABC (Figure 2.1(b)) is also possible, though rarer due to being thermodynamically unstable. This is referred to as rhombohedral graphite and does not exist in a pure form. [19]

Figure 2.1(c) shows three layers of graphite, along with the interatomic separations, the unit cell of graphite and its lattice vectors. The unit cell contains 4 atoms: 2 from each layer. The lattice vector lengths are labelled in the Figure where $\boldsymbol{a}_1 = \boldsymbol{a}_2 = 0.246$ nm and $\boldsymbol{c} = 0.672$ nm. [19, 22] This can be confirmed using X-ray diffraction with Cu Kα radiation. [22] Also shown are the layer spacing $\boldsymbol{c}/2$ and interatomic spacing within each plane $a_0 = 0.141$ nm. [19]

Due to the in-plane sigma bonds being far stronger than the π bonds between layers, graphite is easier to split by separating the stacked layers. This splitting can be carried out repeatedly until a single monolayer remains through repeated exfoliation. This is called graphene and described in more detail in Section 2.1.2.

The properties of graphite often depend on the defects in the material, bringing it away from the non-physical ideal structure described by Figure 2.1. However, many forms of graphite are aggregates of graphite crystallites. Aggregates with larger and parallel-arranged crystallites have properties closer to those of ideal graphite. [19] Single crystal sources of graphite are limited to artificial kish graphite and a small fraction in a few natural ores. Kish graphite has the highest degree of crystallinity and is closest to ideal graphite out of all available sources, but has a limited flake size. Another highly oriented graphite with a wider variety of uses is Highly Ordered Pyrolytic Graphite (HOPG). [23] Examples of HOPG uses are as a substrate used in scanning tunnelling microscopes [24, 25] and for the exfoliation of graphene flakes [26–29].

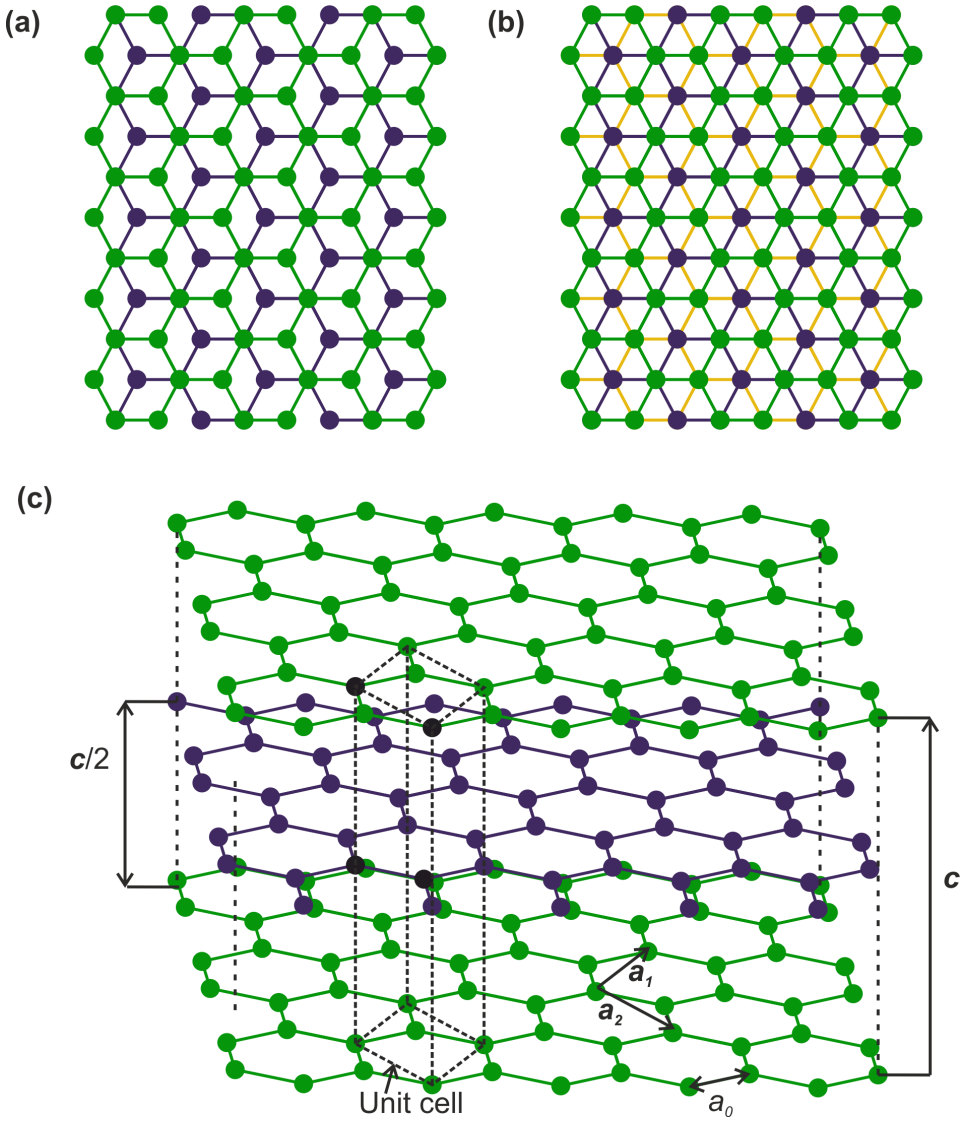

Figure 2.1: Atomic structure of graphite. (a) AB graphite viewed perpendicular to the plane. (b) ABC graphite viewed perpendicular to the plane. (c) Angled view of AB graphite with the unit cell outlined. Atoms coloured black are part of the unit cell.

HOPG is produced from pyrolytic carbon by annealing it under compression. [19, 23] One example of this production is a two-step process, where first pyrolytic carbon is hot pressed at 2800-3000 °C to improve the preferred orientation. This is followed by annealing the graphite between 3400 and 3600 °C under a pressure of 10 kg cm^{-3}. [23]

The electronic properties of graphite can be analysed using the tight-binding model. [30–33] Graphite is found to display semimetallic behaviour with a 41 meV band overlap.

2.1.2 Graphene

The 2D form of graphite is monolayer graphene, which consists of a single layer of carbon in a hexagonal lattice. 2D materials theoretically cannot exist in the free-standing state due to the Mermin-Wagner theorem, which states that the long-range order for 2D crystals is destroyed by long wavelength fluctuations. [34] However, free graphene sheets are not perfectly flat but exhibit slight deformations, allowing them to remain thermodynamically stable. [35] Graphene layers can be stacked vertically to create bilayer, trilayer and few layer graphene. With 11 or more [33] layers of graphene, the electronic properties match those of graphite to within 10%. As with graphite, multilayer graphene basal planes are stacked in the AB formation. The lattice structure of graphene is shown in Figure 2.2(a), as well as the inverse-space lattice and Brillouin zone in part (b). Although not strictly true, graphene is frequently referred to as a two-dimensional material due to monolayer graphene being only one atomic layer thick.

Graphene nanoribbons can be thought of as long strips of monolayer graphene and have similarities to carbon nanotubes. [36, 37] Graphene nanoribbons can be either armchair nanoribbons, cut along the horizontal edges in Figure 2.2, or zigzag nanoribbons, cut along the vertical edges.

Mechanically, graphene is more tensile, durable and flexible than

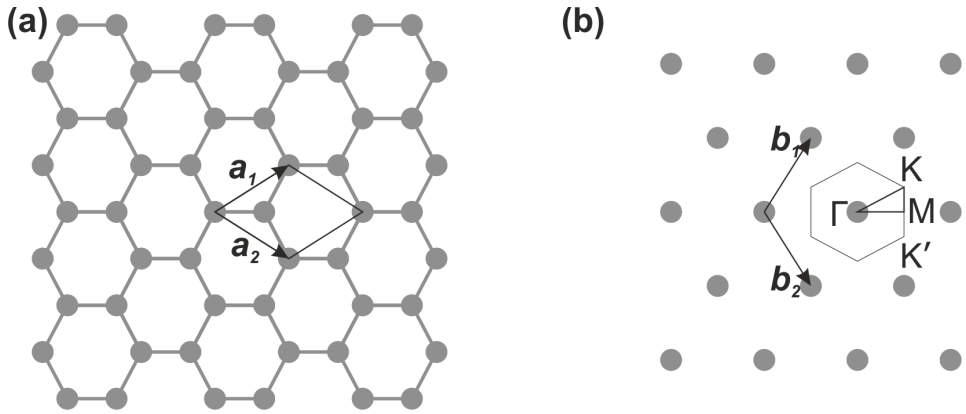

Figure 2.2: Atomic structure and unit vectors of monolayer graphene in (a) normal space and (b) inverse space, along with Γ, K, K′ and M points.

graphite, [38] allowing for its use in flexible electronic materials. [3, 4] Despite the weak interlayer coupling in graphite, graphene and few layer graphene behave notably different electronically. Monolayer graphene acts as a zero bandgap semiconductor, while adding more layers changes the electronic structure to steadily become closer to that of graphite. From bilayer onward, graphene is a semimetal. [33] AB stacked bilayer graphene however, can be used as a tunable direct bandgap semiconductor by electronically gating the two different layers. [39] The energy bands along the path ΓKMΓ in k-space and around the Fermi energy for both monolayer and bilayer graphene calculated using the tight-binding model are shown in Figure 2.3. The tight-binding model uses nearest-neighbour interactions and considers a single π electron per carbon atom. [18, 33, 40]

Graphene can be functionalised with adsorbed molecules. These bonds can be either covalent or noncovalent in nature. Covalent functionalisation breaks the σ bonds between graphene molecules. Two examples of this are hydrogen [41] and fluorine [42, 43] funtionalisation to create graphane and fluorographene respectively. Noncovalent

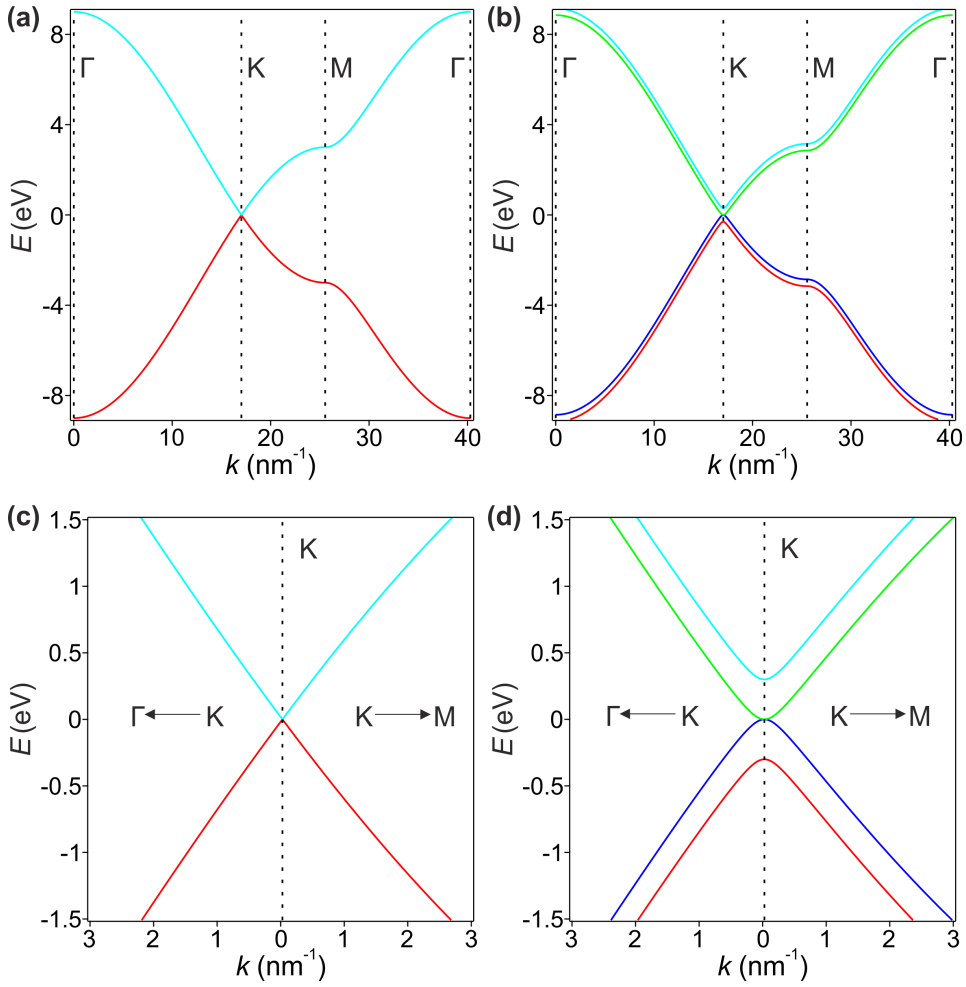

Figure 2.3: Energy diagram along ΓKMΓ for (a) monolayer graphene and (b) bilayer graphene. Zoomed in energy diagram in inverse space around the Dirac point for (c) monolayer graphene and (d) bilayer graphene.

functionalisation can occur through π-π stacking and van der Waals forces. While weaker bonds than in covalent functionalisation, these have the advantage of leaving the sp^2 bonding network unchanged. Molecules containing aromatic rings such as naphthalene diimide, as used in Chapter 5; and dimethylanthracene [44] can bond noncovalently to graphene. These molecules can be deposited by either drop casting or thermal evaporation. [18]

Graphene production

Graphene was successfully exfoliated from HOPG by repeated peeling of small mesas by Novoselov et al in 2004. [45] This method has advantages of being simple and not needing specialised equipment. Further, the crystal domains can be large, even extending into the millimetre range when exfoliated from natural graphite. This level of crystal purity allows for high performance electronics. However, mechanically exfoliated graphene is limited in size to that of the starting graphite, which is too small for many applications, and is unreliable in obtaining graphene of a set number of layers. [46] There are a number of other exfoliation methods for graphene, including ultrasound treatment [47] and intercalation steps [48].

Exfoliation via intercalation is achieved by introducing other materials, frequently alkali metals, into the graphite lattice. These intercalated ions increase the separation between graphene sheets, thus weakening the van der Waals bonds holding the graphite together, and also negatively charge the graphene sheets, causing them to repel each other. This makes exfoliation easier. [46, 49]

A very common method of synthesising large areas of graphene is chemical vapour deposition (CVD) over a catalyst substrate material. [50, 51] The catalyst is normally a metal [52, 53]. The most commonly used metals as substrates are copper and nickel. CVD methods like this can also be used for synthesis of carbon nanotubes. [54–57]

CVD works by passing a feedstock of carbon, most commonly methane, over the substrate at high temperatures; up to 1100 °C in the case of Cu. This feedstock then decomposes to provide a supply of carbon to the substrate. Depending on the carbon solubility of the metal used, carbon is either absorbed and later precipitates out, such as with nickel, or forms graphene as a surface process, such as with copper. Many factors can affect the outcome of the final graphene. These include the carbon source, exposure time, concentration and flow rate, the cooling rate, the oven geometry and the presence of impurities. [18, 46]

One of the disadvantages of CVD graphene is that it has a comparatively small crystal size relative to exfoliated graphene. Fortunately, this effect does not reduce the electronic performance of CVD graphene to a level where it is unusable. Electron mobilities of up to 7350 $cm^2V^{-1}s^{-1}$ have been reported in CVD graphene grown on Cu with grain sizes in the order of 100 μm. [53, 58] This is notably lower than mechanically exfoliated suspended graphene, which has been observed to possess a mobility over 200 000 $cm^2V^{-1}s^{-1}$ at 5 K. [59] The crystal size in CVD graphene depends on the number of nucleation sites. With fewer nucleation sites, larger crystals can be grown within a graphene sheet of the same size as they are able to grow further before meeting another crystal. This allows for some control over the crystal size.

Graphene transfer

For most purposes, including synthesis of devices including graphene or isolating graphene electronically, it is necessary to transfer graphene to a new substrate. The most common target substrate used is silicon dioxide. Exfoliated graphene requires a substrate to handle due to its near two dimensional nature and most applications of graphene require it to be electronically insulating. Thus, it is necessary to remove CVD graphene from its growth metal substrate of Cu or Ni. Graphene

transfer is an active area of research, with many varying methods being employed. [51, 60–66] These transfer methods all cause some damage to either the graphene or target substrate.

The first method of graphene transfer is wet transfer by floating the graphene on the surface of a solution designed to etch away the original substrate. [51, 60] Before etching the substrate, the graphene is coated in a protective layer of polymer, frequently polymethyl methacrylate (PMMA). This helps prevent damage and acts as a scaffold to prevent the graphene from folding or wrinkling. In the case of copper substrates, a variety of etching solutions can be used, including ferric chloride ($FeCl_3$) and hydrochloric acid (HCl). The graphene can then be deposited on the new substrate, normally after washing with deionised water. Although able to transfer large areas of graphene to a wide variety of substrates, this method lacks the ability to accurately align graphene when depositing it on the new substrate. Damage to the graphene is often received during the etching process, where trapped metal particles between the graphene and substrate act as scattering centres and dope the graphene; and from a lack of flatness when deposited on the new substrate, leading to the formation of cracks, tears and wrinkles in the graphene. [64, 67] Further, complete removal of polymer residues on the graphene is difficult to achieve despite the existence of numerous cleaning processes.

A second common method is stamping of graphene onto a new substrate after attaching it to a suitable material such as PDMS [61] or thermal release tape [62]. These methods allow for alignment of the graphene but are generally limited to transferring smaller areas of graphene than wet transfer. It is possible to remove the need for etching of the starting substrate [63], reducing potential damage to the graphene. However, the strains involved in transfer can cause cracks to form [64] and residues from the stamp may still remain on the graphene [67].

Another method, similar to stamping is the use of a self-release layer of a separate polymer in between the graphene and a main stamp polymer. [64–66] This release layer is chosen to adhere to the graphene more than the stamp. After stamping, the release layer detaches from the stamp and remains on the substrate along with the graphene, before being washed away to expose the transferred graphene. Advantages when compared to the standard stamping method are a reduction in cracks formed [64], a higher yield and the ability to transfer to a wider range of target substrates, including flexible substrates [65]. Some progress is still required to remove all damage from transfer however. [68] We use a modified self-release layer method of transfer to construct the samples used in Chapter 5.

2.2 Quantum Tunnelling

This section briefly covers the equations for tunnelling transmission coefficient and current density through a barrier in one dimension.

2.2.1 Obtaining a transmission coefficient in one dimension

A simple case to consider is that of an electron with energy E_x and wavefunction ψ incident on a rectangular energy barrier of height Φ and width w between a and b in one dimension, as represented in Figure 2.4. In region I, ψ is a sinusoidal function before it meets the barrier. Region II is the tunnel barrier, where the presence of the electron is classically forbidden as $\Phi > E_x$. According to quantum physics, ψ decays exponentially as x increases within region II. On reaching region III, ψ once again becomes a sinusoidal function of x, but now with a lower amplitude, corresponding to a lower probability of the electron being present. As w increases, ψ becomes vanishingly small until

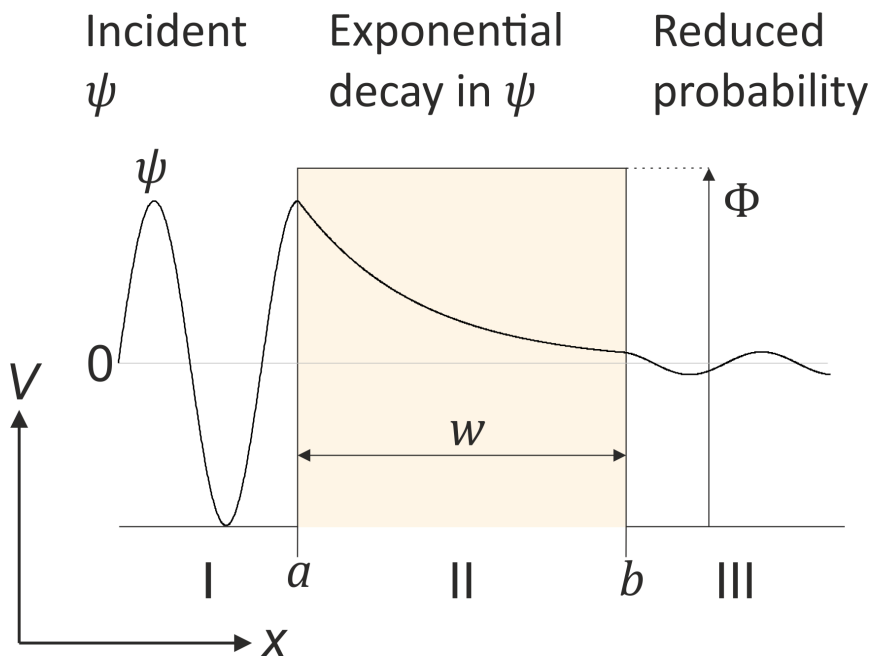

Figure 2.4: Energy diagram and wavefunction of an electron travelling in the x-direction incident. Region I: Incident wavefunction with no energy barrier. Region II: Barrier of higher energy forbidding classical travel of electron. Region III: Zero energy region in which the electron has a lower probability to be present.

the probability of the electron reaching region III is 0 when $w = \infty$. Even with $w < \infty$, the probability of the electron successfully tunnelling through region II rapidly becomes negligible due to ψ decaying exponentially. The electron is reflected if it is not transmitted.

Using the Wentzel–Kramers–Brillouin (WKB) method [69], the transmission coefficient $T(E_x)$ can be calculated as a function of particle energy. In the case of a one-dimensional rectangular barrier in the x direction, the relationship is found to follow the equation

$$T(E_x) = \frac{16E_x(\Phi - E_x)}{\Phi^2} \exp\left[-2\sqrt{2m(\Phi - E_x)}\frac{w}{\hbar}\right] \tag{2.1}$$

where $\hbar$ is the reduced Planck constant and m is the particle mass. The remaining part of the wavefunction is reflected.

Equation (2.1) can be generalised to describe a barrier where Φ is a function of x. This is useful as realistic tunnel barriers are unlikely to be rectangular, but instead have a continuous shape. A value for $T(E_x)$ can be obtained by integrating over the tunnel barrier between a and b, respectively the points where ψ encounters and leaves the barrier. This gives Equation (2.2):

$$T(E_x) = \exp\left[-2\int_a^b \frac{\sqrt{2m(\Phi(x) - E_x)}}{\hbar} dx\right]. \tag{2.2}$$

2.2.2 Tunnel barrier current density

It is often more useful to work with current density J than with the tunnelling probability of individual charge carriers. Approximate relations between J and the tunnel barrier height Φ were derived from a single theory in detail by Simmons in 1963. [70–73] These approximations are applied to electrodes separated by thin films and are for three different regimes: low voltages close to zero; an intermediate range where the voltage across the film $V \leq \Phi/e$; and a high voltage

range where $V > \Phi/e$. [72, 73] In contrast to the Fowler-Nordheim equations used for cold field emission [74], Simmons' equations include dipolar image effects across the barrier [70–73]. Other models including thermally assisted tunnelling are used, such as in the presence of magnetisation. [75]

This derivation starts from the WKB approximation in Equation (2.2). Labelling the electrodes 1 and 2, the number of electrons tunnelling from electrode 1 to electrode 2 can be defined as

$$N_1 = \frac{1}{m} \int_0^{E_m} n\left(v_x\right) T\left(E_x\right) dE_x, \tag{2.3}$$

where E_m is the maximum electron energy in the electrode and $n\left(v_x\right) dv_x$ is the number of electrons per unit volume with x velocity between v_x and $v_x + dv_x$. It is assumed that the velocity distribution is isotropic, and thus $n(v)$ is given by

$$n(v)dv_x dv_y dv_z = \frac{2m^4}{h^3} f(E)dv_x dv_y dv_z, \tag{2.4}$$

where $f(E)$ is the Fermi-Dirac distribution:

$$f(E) = \frac{1}{1 + \exp\left[(E - E_F)/k_B T\right]}, \tag{2.5}$$

with E_F as the Fermi energy and k_B as the Boltzmann constant. This leads to the equation

$$n(v_x) = \frac{2m^4}{h^3} \int \int_{-\infty}^{\infty} f(E)dv_y dv_z = \frac{4\pi m^3}{h^3} \int \int_0^{\infty} f(E)dE_r. \tag{2.6}$$

The integrand is in polar coordinates: ${v_r}^2 = {v_y}^2 + {v_z}^2$ and $E_r = m{v_r}^2/2$, which gives for N_1

$$N_1 = \frac{4\pi m^2}{h^3} \int_0^{E_m} T(E_x)dE_x \int_0^{\infty} f(E)dE_r. \tag{2.7}$$

Using $T(E_x)$ as equal in both directions and electrode 2 at a positive potential V with respect to electrode 1, the number of electrons

tunnelling from electrode 2 to electrode 1 N_2 can be similarly derived. The Fermi-Dirac distribution changes to $f(E + dV)$ and

$$N_2 = \frac{4\pi m^2}{h^3} \int_0^{E_m} T(E_x) dE_x \int_0^{\infty} f(E + eV) dE_r. \tag{2.8}$$

The current density can be obtained through $J = Nev$, where the net flow of electrons is $N = N_1 - N_2$:

$$N = \int_0^{E_m} T(E_x) dE_x \left(\frac{4\pi m^2}{h^3} \int_0^{\infty} [f(E) - f(E + eV)] dE_r \right), \tag{2.9}$$

thus

$$J = \int_0^{E_m} T(E_x) dE_x \left(\frac{4\pi m^2 e}{h^3} \int_0^{\infty} [f(E) - f(E + eV)] dE_r \right). \tag{2.10}$$

For a rectangular barrier at near-zero bias, J can be approximated to

$$J \simeq \frac{3\sqrt{2m\Phi}}{4s} \left(\frac{e}{h} \right)^2 \exp \left[-\frac{4\pi s/h}{\sqrt{2m\Phi}} \right] V, \tag{2.11}$$

where ϕ is the barrier height above the Fermi energy and s is the separation between electrodes 1 and 2. [72] A useful feature of this approximation is that it is linear in V allowing for easier calculations and fitting of the conductance at zero bias voltage. A second feature is that the effective mass can be coupled with the barrier height to treat as a single fitting parameter if necessary.

For the intermediate range, defined as when $V < \Phi/e$, J becomes

$$\begin{aligned} J = \frac{e}{2\pi h s^2} \Bigg\{ & \left(\Phi - \frac{eV}{2} \right) \exp \left[-\frac{4\pi s\sqrt{2m}}{h} \sqrt{\Phi - \frac{eV}{2}} \right] \\ & - \left(\Phi + \frac{eV}{2} \right) \exp \left[-\frac{4\pi s\sqrt{2m}}{h} \sqrt{\Phi + \frac{eV}{2}} \right] \Bigg\}. \end{aligned} \tag{2.12}$$

Away from zero bias, the conductance increases exponentially as shown in Equation (2.12). [72]

Finally, the high voltage ($V > \Phi/e$) approximation derived by Simmons is:

$$J = \frac{2.2e^3F^2}{8\pi h\Phi} \exp\left[-\frac{8\pi\sqrt{2m}\Phi^{3/2}}{2.96heF}\right], \tag{2.13}$$

where $F = V/s$ is the electric field strength in the thin barrier material. [72]

2.3 Effective medium approximations

The use of an effective medium approximation (EMA) allows for the macroscopic properties of composite systems to be modelled without the need to calculate the effects of each individual part. This is particularly useful in composites with randomised distributions of the different phases. The groundwork for such theories was laid out by Bruggeman in 1935 [76] and later continued by Landauer [77]. While Landauer applied the theory to the conductivity of binary metallic mixtures [77], a variety of EMAs have since been developed for differing mixtures. [78–82]

Landauer's model was applied to a random distribution of two different crystal types, 1 and 2 with respective conductivities σ_1 and σ_2. In the model, this distribution around each metal crystal is replaced with a single, uniform effective medium, whose conductivity σ_e is uniform. This is illustrated in Figure 2.5. The two materials are present in volume filling fractions ν_1 and $\nu_2 = 1 - \nu_1$. Further, it is assumed that each crystal can be treated as a spherical inclusion within the EMA. Looking at the charge on the surface of a crystal and following through calculations for the electric field and polarisation, the following equation can be obtained and solved for σ_e:

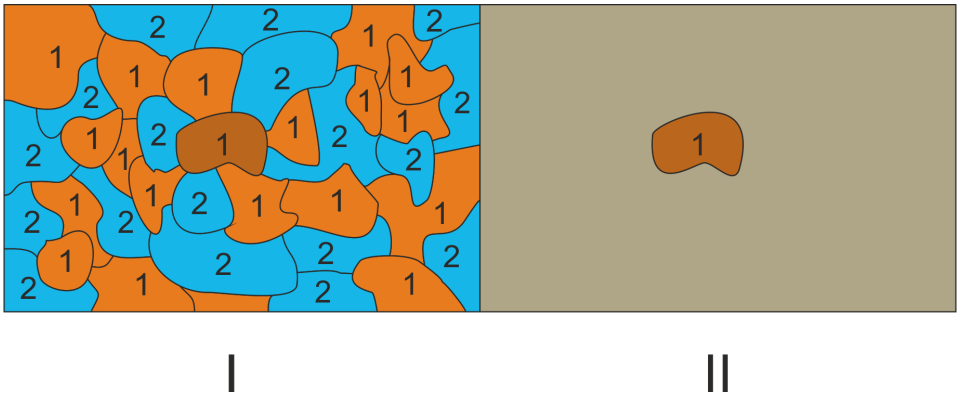

Figure 2.5: The approximation made by Landauer. A binary metallic mixture (region I) is composed of two different metals, 1 (brown) and 2 (blue). Each crystal instead sees the surrounding area as a constant medium with a conductivity equal to that of the random structure in region I. This is illustrated for the dark brown crystal in region II.

$$\nu_1 \frac{\sigma_1 - \sigma_e}{\sigma_1 + 2\sigma_e} + \nu_2 \frac{\sigma_2 - \sigma_e}{\sigma_2 + 2\sigma_e} = 0. \tag{2.14}$$

The solution to Equation (2.14) is

$$\sigma_e = \frac{1}{4}\Big[(3\nu_2 - 1)\sigma_2 + (3\nu_1 - 1)\sigma_1 \pm \sqrt{[(3\nu_2 - 1)\sigma_2 + (3\nu_1 - 1)\sigma_1]^2 + 8\sigma_1\sigma_2}\Big], \tag{2.15}$$

which gives two solutions, although one is negative hence ignored as not physical. [77, 82] Moving away from purely metallic mixtures gives two special cases. The first is a composite of a normal metal and a perfect conductor when σ_2 is finite and $\sigma_1 \to \infty$. The second is that of a metal-insulator composite, with σ_1 finite and $\sigma_2 = 0$. The latter is more relevant to this thesis due to the composites used.

The EMA in the case of a metal-insulator composite can be tied to a percolation threshold. Singular properties are found near a critical

value $\nu_1 = \nu_c = 1/3$. By solving Equation (2.15), it is seen that below this critical value, $\sigma_e = 0$ and above it, σ_e is finite. [82]

Using this basis, EMAs have been used to analyse percolation systems. This comparison was first explored by Kirkpatrick in 1973. [83]. Examples of adaptations of the EMA model include combining EMA with the real-space renormalisation method to model the critical region of composite materials [79] and modifying the EMA to account for particle sizes in granular metal-polymer composites [84]. The Landauer model suffers limitations including being ineffective at modelling mixtures without random distributions or regions that can be approximated by a sphere [77].

2.4 Percolation in composites

The composites used in this thesis consist of conductive particles randomly placed in an insulating matrix. A percolation model could thus be a functional method of modelling these GSCs. Although a basic percolation model is too simple to describe GSCs, it is a useful step more detailed than the EMA from which to introduce a more accurate variant: tunnelling percolation. There have been a number of investigations into the uses of percolation models for GSCs [7,17] and similar materials using metal conducting particles [14,84] or rod-shaped conducting particles [13]. Studies have been carried out analysing the piezoresistivity of tunnelling percolation systems. [7,17,85] These relate to the findings in Chapters 3 and 4. Unlike existing percolation models, our tunnelling percolation model, detailed in Chapter 4, accounts for the change within the percolation paths over time and thus the change in the conductivity of the system in response to an external stimulus: stress.

A percolation system consists of a lattice with randomly occupied sites according to a filling fraction. This gives each lattice site a proba-

bility p of being occupied. A simple model for 2 dimensions to illustrate this is shown in Figure 2.6. A lattice site is considered active and able to conduct electricity if occupied by a conductive particle. Current is only allowed to flow between nearest neighbour sites, with connected occupied sites forming clusters and the resistance between occupied nearest neighbour sites being equal to a set value R_b. At least one cluster of adjacent occupied sites stretching from one end of the lattice to the other is required for the network to be conductive. The first cluster spanning the length of the lattice occurs when $p = p_c$, the critical filling probability.

When $p < p_c$, as shown in Figure 2.6(a), individual clusters are too small to span the lattice. As there is no complete path for current to follow from the input to the output side, the network remains insulating with no change in overall conductivity. At p_c the conductivity of the network is equal to the conductivity of the path connecting both ends of the lattice. In Figure 2.6(b), this is seen to be $9R_b$, where R_b is the resistance of an individual bond. Increasing p further, as in Figure 2.6(c), allows for the formation of multiple conduction paths across the network in parallel, reducing the overall resistance.

A more complicated model, which may be used in 2 or 3 dimensions to look at composites, places conducting particles randomly within the insulating material, preventing any overlap between particles. In this model, current can flow between any conducting particles within a certain distance of each other, to simulate particle size, rather than between nearest neighbours as in a regular lattice model. Due to the nature of this model, the critical filling fraction depends on the shape of the conducting particles. [86]

Further analysis can be carried out using the volume filling fraction (area in two dimensions) of conducting particles ν in place of p due to the lack of defined lattice sites and continuous nature of the parameter space. Likewise, a critical volume fraction ν_c replaces p_c. Investigating

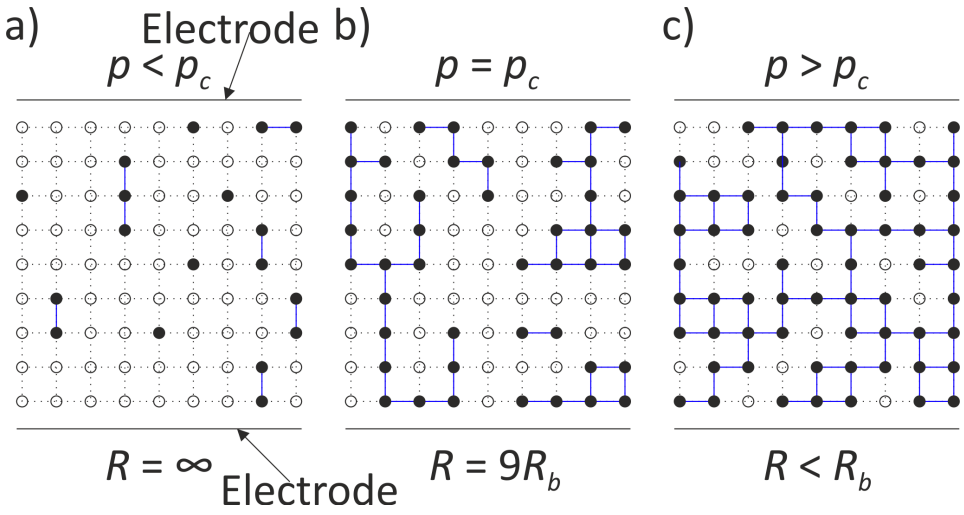

Figure 2.6: Examples of percolation lattices a) below the critical filling fraction p_c; b) at the critical filling fraction and c) above p_c.

the electrical properties of both this model and regular lattices results in a power law relation between conductivity G and ν of the form

$$G(\nu) \propto (\nu - \nu_c)^{\alpha}, \tag{2.16}$$

where α is a critical exponent. [83, 87] In many cases, this exponent is found to be independent of material properties other than dimensionality. This is referred to as the universal critical exponent and is approximately 2 for three-dimensional percolation networks. [88] However, this universality does not always hold true. [10, 89]

Tunnelling percolation

Somewhat surprisingly, conducting particles embedded in a continuous network with tunnelling possible between multiple particles can also exhibit percolation-like properties [11, 90]. This appears paradoxical, as the presence of tunnelling appears to maintain a finite conductivity through the network regardless of ν, does not give a cluster

structure similar to Figure 2.6 and creates conduction networks which are not well described by tortuous paths. [11] This gives rise to tunnelling percolation models. Although not occurring in one dimension, a percolation-like threshold appears in 3D systems due to the exponential decay of tunnelling probability and the distribution function of particle separations. Percolation-like behaviour occurs when particles have separations on the same order as the tunnelling decay constant. [11] Another factor is that the random positioning of conducting particles at high ν values becomes more lattice-like in structure due to packing constraints. [11, 91] While some examples of percolation networks follow universal behaviour patterns ($\alpha \approx 2.0$), many have been proven not to. [90]

In tunnelling percolation models for composites, conducting particles are not in contact with each other and have a tunnelling bond between individual particles with a finite conductivity depending on their separation distance. The size of the particles is modelled by using a hard core. [12] This ensures that the correct value of ν is used in a model.

Within a tunnelling percolation network, the value of ν_c depends on many factors. For example, varying the shape of the conducting particles affects the conductivity at varying values of ν. Spheres give the lowest conductivity, with the use of oblate spheroids increasing conductivity and prolate spheroids increasing conductivity further. [12] A similar effect is seen by comparing different structure particles of carbon black, such as high-structure Ketjen black compared to the less complex Cabot black or "no-structure" spherical particles [90]. Our samples in this thesis use approximately spherical particles of HOPG. Another factor is the relative magnitudes of the tunnelling length λ and conducting particle size, frequently using the diameter d for spherical particles. Decreasing the ratio λ/d decreases conductivity [92], due to larger particle sizes resulting in larger separations between particles

when the value of ν is fixed.

2.5 Calculation of stress and strain in a bilayer from its radius of curvature

Chapters 3 and 4 analyse the effects of strain steps applied to a GSCs by applying a bilayer strain across the composite and its cellulose acetate substrate. This section will explain the calculations used to obtain stress and strain in the context of GSCs. We applied stress and strain increments by applying uniform horizontal compressions to load strain, before removing these compressions to unload strain. The increments were separated by a constant time delay τ. We applied strain using this method because using a bilayer strain allows for the uniform application of stress across the bilayer and for the biaxial stress $[\sigma_{xx}, \sigma_{yy}, 0]$ to be accurately calculated using the material parameters, shown in Table 2.1, [93] and the sample's radius of curvature ρ, as in Figure 2.7. This could be done by balancing the torques and forces in the bilayer to give an equation for the stress component increments. [94] At the nth step, occurring at time $t = n\tau$, the value of ρ changes from ρ_{n-1} to ρ_n and we get the equation

$$\begin{cases} \Delta_n \sigma_{xx} = \dfrac{E_s a_s^3}{6(1-\gamma_s^2)a_c(a_c+a_s)} \Delta_n(1/\rho) \\ \Delta_n \sigma_{yy} = \dfrac{E_s a_s^3 \gamma_s}{6(1-\gamma_s^2)a_c(a_c+a_s)} \Delta_n(1/\rho) \\ \Delta_n \sigma_{zz} = 0 \end{cases}, \tag{2.17}$$

where E_s, a_s and γ_s are respectively the substrate's Young's modulus, thickness and Poisson ratio, a_c is the thickness of the GSC layer and $\Delta_n(1/\rho) = \rho_n - \rho_{n-1}$.

Viscoelastic deformation occurs within the PDMS polymer after the stress increment and until the next increment is applied at $t = (n+1)\tau$.

Property	GSC	Cellulose acetate
Young's modulus (MPa)	$E_c = 1.8 \pm 0.05$	$E_s = 41 \pm 11$
Poisson ratio	$\gamma_c = 0.4999 \pm 0.0001$	$\gamma_s = 0.391 \pm 0.008$
Thickness (μm)	$a_c = 100$	$a_s = 100$

Table 2.1: Properties of the two layers within the bilayer samples. [7]

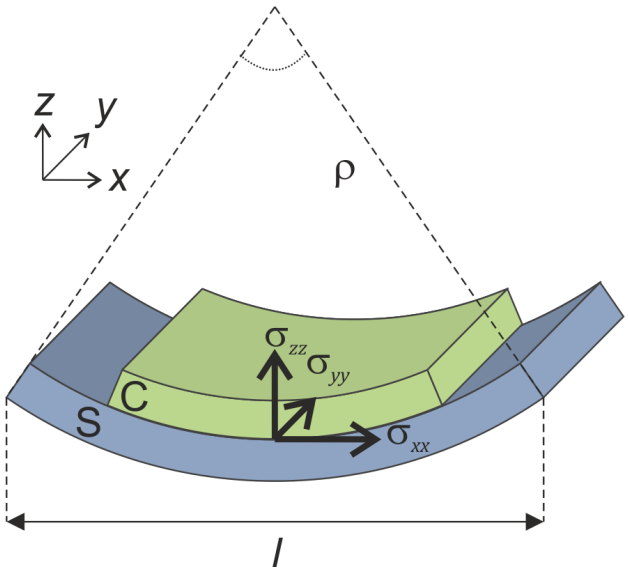

Figure 2.7: Changing the radius of curvature of the composite and the directions of the resulting stresses. Layer C is the composite while layer S is the substrate.

As the PDMS is not a perfect viscoelastic solid, a fraction of the stress applied $0 < \varepsilon < 1$ is retained even at long times after the initial application, [95] causing residual stress to accumulate over time. Over N increments, the accumulated stress components $\sigma_{\alpha\alpha}$ can be written as

$$\sigma_{\alpha\alpha}(t) = \sum_{n=0}^{N} \Delta_n \sigma_{\alpha\alpha}\, H(t - n\tau) \left[(1-\epsilon) e^{-\frac{t-n\tau}{\tau_R}} + \epsilon \right], \tag{2.18}$$

where $\Delta\sigma_{\alpha\alpha}$ are the stress increment components from Equation (2.17), $\alpha, \beta \equiv \{x, y, z\}$, τ_R is the stress relaxation time and $H(t)$ is the heavy-side step function.

We calculate the strain tensor using Laplace transforms due to the incremental nature of the stain steps, giving Equations (2.19) and (2.20) for stress and strain.

$$\bar{\sigma}_{\alpha\beta}(p) = \int_0^\infty dt\; \sigma_{\alpha\beta}(t)\, e^{-pt} \tag{2.19}$$

$$\bar{\varepsilon}_{\alpha\beta}(p) = \int_0^\infty dt\; \varepsilon_{\alpha\beta}(t)\, e^{-pt} \tag{2.20}$$

The composite obeys the three-dimensional Hooke's law as its viscoelastic time constraints are accounted for in the Laplace transforms. [95] As the composite is isotropic, the principle strain components are

$$\begin{pmatrix} \bar{\varepsilon}_{xx}(p) \\ \bar{\varepsilon}_{yy}(p) \\ \bar{\varepsilon}_{zz}(p) \end{pmatrix} = \frac{1}{\bar{E}(p)} \begin{pmatrix} 1 & -\gamma_c & -\gamma_c \\ -\gamma_c & 1 & -\gamma_c \\ -\gamma_c & -\gamma_c & 1 \end{pmatrix} \begin{pmatrix} \bar{\sigma}_{xx}(p) \\ \bar{\sigma}_{yy}(p) \\ \bar{\sigma}_{zz}(p) \end{pmatrix} \tag{2.21}$$

where $\bar{E}(p)$ is the Young's modulus of one tunnelling percolation bond. Following through the relations in Equations (2.17) and (2.18) we note that $\sigma_{yy}(t) = \gamma_s \sigma_{xx}(t)$ and $\sigma_{zz}(t) = 0$. This allows us to write the strain components as functions of x-directional stress.

$$\begin{aligned}\bar{\varepsilon}_{xx}(p) =& \frac{1-\gamma_c\gamma_s}{\bar{E}(p)}\bar{\sigma}_{xx}(p)\\ \bar{\varepsilon}_{yy}(p) =& \frac{\gamma_s-\gamma_c}{\bar{E}(p)}\bar{\sigma}_{xx}(p)\\ \bar{\varepsilon}_{zz}(p) =& \frac{-(1+\gamma_s)\gamma_c}{\bar{E}(p)}\bar{\sigma}_{xx}(p)\end{aligned} \tag{2.22}$$

As $1 > \gamma_c > \gamma_s$ in this case, we note that both $\bar{\varepsilon}_{yy}$ and $\bar{\varepsilon}_{zz}$ always have the opposite sign to $\bar{\varepsilon}_{xx}$. $\bar{E}(p)$ is calculated by using a spring-dashpot link to model the PDMS barrier separating two graphite particles as in Figure 2.8(a). The link used is that of a standard linear solid (SLS) model, with the use of the linear regime justified by the small size of the strain increments applied ($< 0.5\%$). In this model, η is the viscosity of the PDMS (between 20000 and 26000 mPaS) and E_1 and E_2 are the partial Young's moduli. Solving the SLS model then gives us the relationship between σ and ε:

$$\dot{\sigma} + \frac{\sigma}{\tau_R} = E_D\left(\dot{\varepsilon} + \frac{\varepsilon}{\tau_c}\right), \tag{2.23}$$

where $E_D = E_1 + E_2$ is the dynamic Young's modulus, $\tau_R = \eta/E_2$ is the stress relaxation time and $\tau_c = \eta(E_1 + E_2)/(E_1E_2)$ is the strain relaxation time, referred to as the creep time in the rest of this thesis. By taking the Laplace transform of Equation (2.23) we obtain $\bar{E}(p)$ from the viscoelastic Hooke's law:

$$\bar{E}(p) = \frac{\bar{\sigma}(p)}{\bar{\varepsilon}(p)} = E_D\frac{p + 1/\tau_c}{p + 1/\tau_R}. \tag{2.24}$$

We can return to the time domain by taking the inverse Laplace transform of Equation (2.24),

$$\varepsilon(t) = E_D^{-1}\left[\sigma(t) + \int_{-\infty}^{t}\Psi(t-t')\frac{d\sigma(t')}{dt'}dt'\right], \tag{2.25}$$

where

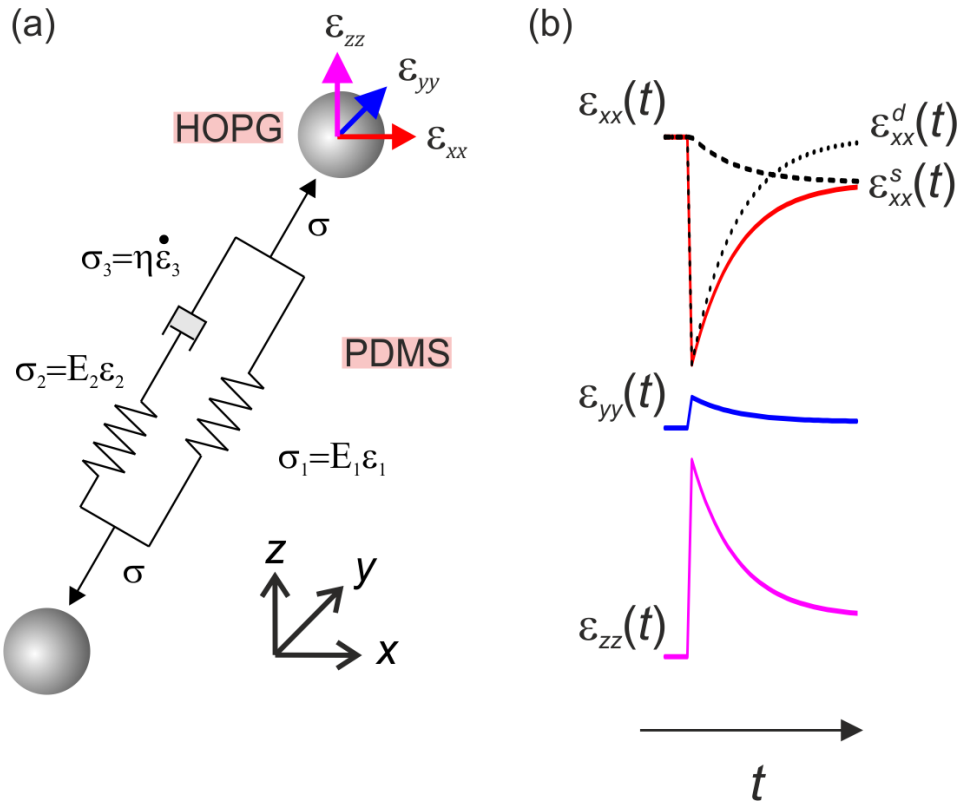

Figure 2.8: (a) The standard linear solid model of the PDMS layer between HOPG particles. E_1 and E_2 are the partial Young's moduli and η is the viscosity of the PDMS. (b) Time evolution of the strain components after a compressive strain increment is applied. Each component is the sum of a static (dashed line) and dynamic part (dotted line). The static part tends towards a finite value and the dynamic part vanishes at large t.

$$\Psi(t) = \frac{\tau_c}{\tau_R}\left[1 - \exp\left(-\frac{t}{\tau_c}\right)\right]. \tag{2.26}$$

We note that there are two terms in Equation (2.25). The first of these terms is the elastic response to the stress increments, relating to the instantaneous increase in strain following each increment. The second term is the viscoelastic relaxation of strain after an applied stress step. It is described by an integral containing the memory of earlier stress changes weighted by $\Psi(t)$, the creep function. As the three-dimensional Hooke's law described by Equation (2.22) only differs from the one-dimensional Hooke's law in Equation (2.24) by a constant multiplicative term, the 3D strain components will obey the dynamics shown in Equation (2.25). Substituting in the stress components from Equations (2.17) and (2.18) allows us to obtain an expression for the strain in three dimensions within the composite, $\boldsymbol{\varepsilon}(t)$.

$$\begin{aligned}
\varepsilon_{xx}(t) =& -\frac{E_s}{6E_c}\frac{1-\gamma_c\gamma_s}{1-\gamma_s^2}\frac{a_s^3}{a_c(a_c+a_s)}\left[f(t,N)+g(t,N)\right] \\
\varepsilon_{yy}(t) =& -\frac{E_s}{6E_c}\frac{\gamma_s-\gamma_c}{1-\gamma_s^2}\frac{a_s^3}{a_c(a_c+a_s)}\left[f(t,N)+g(t,N)\right] \\
\varepsilon_{zz}(t) =& +\frac{E_s}{6E_c}\frac{\gamma_c(1+\gamma_s)}{1-\gamma_s^2}\frac{a_s^3}{a_c(a_c+a_s)}\left[f(t,N)+g(t,N)\right],
\end{aligned} \tag{2.27}$$

where

$$f(t,N) = \sum_{n=0}^{2N-1} \Delta_n(1/\rho)H(t-n\tau)e^{-\frac{t-n\tau}{\tau_c}}, \tag{2.28}$$

and

$$g(t,N) = \sum_{n=0}^{2N-1} \Delta_n(1/\rho)H(t-n\tau)\varepsilon\frac{\tau_c}{\tau_R}\left(1-e^{-\frac{\tau_c}{\tau_R}}\right). \tag{2.29}$$

This strain can be decomposed as $\boldsymbol{\varepsilon}(t) = \boldsymbol{\varepsilon}^d(t) + \boldsymbol{\varepsilon}^s(t)$, where $\boldsymbol{\varepsilon}^d(t)$ is a dynamic strain obtained by removing $g(t,N)$ and $\boldsymbol{\varepsilon}^s(t)$ is a static

strain obtained by removing $f(t, N)$. $\boldsymbol{\varepsilon}^d(t)$ is a strain responsible for the initial increase and vanishing at long times, while $\boldsymbol{\varepsilon}^s(t)$ is a component driven my the stress accumulation and tending towards a finite value of ϵ.

The responses of the principal strain components following a decrease in ρ are shown in Figure 2.8(b). As ε_{xx} is negative, the composite contracts in the x direction and expands in both the y and z directions where $\varepsilon_{yy}, \varepsilon_{zz} > 0$. The y expansion is a result of the differences in Poisson ratios between the two layers ($\gamma_s < \gamma_c$). Switching to an increase in ρ causes the strain to change sign, allowing for study of piezoresistance symmetry with respect to strain sign.

Chapter 3

Sensing with transient tunnelling currents in Graphite Silicone Composites

This chapter details the experimental work done with physical GSC samples. Section 3.1 describes the methods used to fabricate the samples and the experiments performed to examine the piezoresistive properties of the composite. The first experiment investigates the overall effects of applying stress perturbations to a sample, while the second experiment measures the response time of the composite piezoresistance. The results of these experiments are presented and discussed in Section 3.2.

3.1 Methods

3.1.1 Fabrication of GSC

Our composite devices used in this research consist of three parts. The insulating silicone matrix is composed of a 2-part mixture of Alchemix RTV 137, a room temperature vulcanising rubber with a molecular structure as seen in Figure 3.1(a) and (b) in 3D, and C137 Slow (C137 S), the slower option of two catalysts used to aid vulcanisation of the RTV rubber. Both products are from Alchemie Ltd. We have prepared the two parts by mixing them in a 100:5 ratio by weight. [93] They have an appearance matching Figure 3.1(c) when cured. We chose this mixture for its similarity to the discontinued RTV 139, which was used in previous work by the group. [1, 8, 96] HOPG nanoparticles 450 nm in diameter from Nanoamor (Figure 3.1(d)) were used for the graphite parts; also due to their use in previous research. This mixture produces a composite material capable of conducting through use of a tunnelling percolation network. [1, 8, 96]

As we measured the graphite fraction of conducting GSCs using the volume fraction ν, a calculation was required in order to obtain the required weight ratio for mixing into the composite. This required the use of the tabulated values for ρ_s, ρ_c and ρ_g, which are respectively the densities of the silicone, catalyst and HOPG used. These densities are shown in Table 3.1 along with the viscosities of the materials. [93] The equation used for ν is

$$\nu = \frac{\frac{m_g}{\rho_g}}{\frac{m_s}{\rho_s} + \frac{m_c}{\rho_c} + \frac{m_g}{\rho_g}} \tag{3.1}$$

where m_s, m_c and m_g are the masses of the silicone, catalyst and graphite respectively. The values for the masses used varied with both ν and the amount of composite mixed at once. We calculated mass ratios for m_g with varying ν to fit relative to the 100:5 ratio between

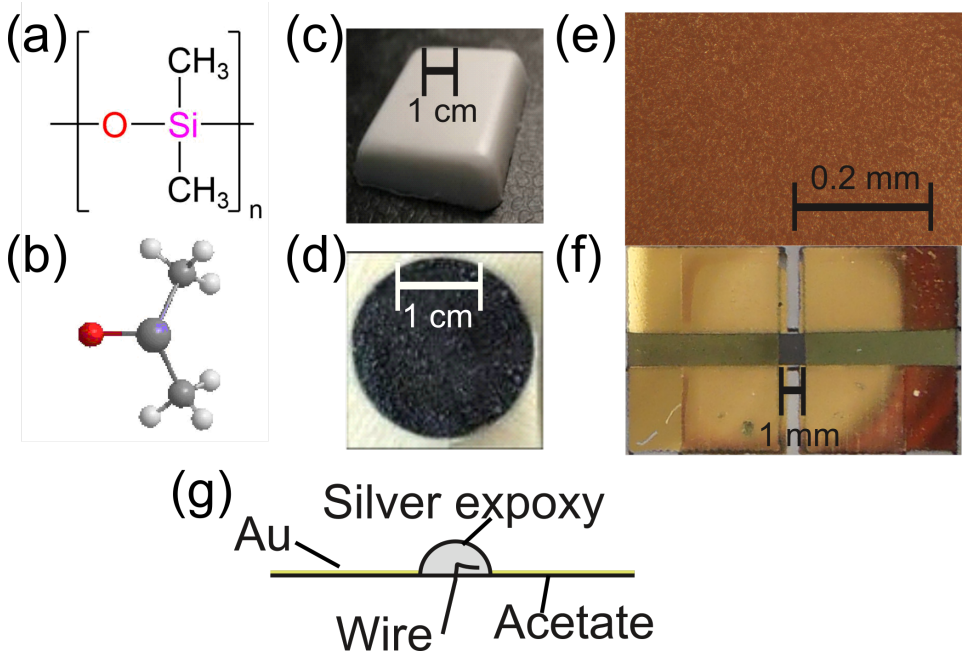

Figure 3.1: The GSC components used. (a) Chemical structure of the monomer in chains of RTV137. (b) 3D representation of this monomer. (c) Cured pristine RTV137. (d) HOPG nanoparticles. (e) Optical image of mixed and cured composite. (f) Top-down view of a sample before the application of wires. (g) Diagram of the connection between the wire and gold contact.

Property	**RTV 137**	**C137 S**	**HOPG**
Density (gcm^{-3})	1.05-1.15	0.93-0.98	2.25
Viscosity (mPaS)	20000-26000	15-25	Powder

Table 3.1: Densities and viscosities of the individual GSC components.

ν	**RTV 137**	**C137 S**	**HOPG**
23.5%	100	5	64.2
25%	100	5	69.7
26.5%	100	5	75.3
28%	100	5	81.3
29.5%	100	5	87.4
31%	100	5	93.9

Table 3.2: Dimensionless mass ratios of GSC components for different HOPG volume filling fractions.

silicone and catalyst and show these values in Table 3.2.

To mix the GSC, we weighed a set amount of RTV 137 out based on how much composite is required. We then calculated the required amount of HOPG using Table 3.2 and measured it out. This range of ν values is used as 23.5% is the percolation threshold and 32% is the miscibility threshold of these HOPG particles in PDMS. Filling fractions beyond these two values are thus less relevant to observe. We then mixed the two parts by adding the HOPG in manageable amounts and fully mixing in before adding more HOPG until the measured amount is used. Mixing was done manually using a mortar and pestle and continued until the mixture became homogeneous. Due to the addition of HOPG, the viscosity of the mixture increased. Next, we weighed out the required amount of catalyst and added it to the composite before also mixing it in fully. This step was done after the mixing of silicone and HOPG to prevent inhomogeneous mixing of the GSC or it being

too dry to spread due to the mixture beginning to cure.

The composite was then spread out onto a cellulose acetate substrate. We used an electrical tape template to limit the composite to the desired areas of substrate and give a controlled thickness of 100 μm to the composite. The composite was then flattened out and limited to the height of the electrical tape using a metal spatula. The GSC was left to cure at room temperature, taking approximately a week to reach optimum properties and taking a form as shown in Figure 3.1(e). The tape template was then peeled off, leaving strips of composite.

To create contacts for measurement, we deposited a 100 nm layer of gold onto the GSC and acetate substrate using a thermal evaporator. A strip of GSC and acetate was masked off for each sample using another, patterned layer of acetate, creating samples as seen in Figure 3.1(f). Following this, we then cut the samples were down to size and made a small pinhole in each of the four contacts to allow a 0.2 mm diameter wire to pass through them. To allow measurements to be made, we folded this wire over and attached it to the gold using a two-part silver epoxy resin.

3.1.2 Calibrated bilayer strain experiment

The first experiment examined the effects of applying multiple successive stress perturbations to a GSC sample. We achieved this by using a specialised strain rig shown in Figure 3.2 to apply bilayer strains by bending the sample and controlling the radius of curvature ρ using horizontal compression. Slanted clamps held the sample in place while it bent. These clamps were attached to the jaws of a set of vernier callipers: one fixed in place, with the calliper jaw holding the other clamp attached to a linear actuator controlled by a stepper motor. As the motor turned, the calliper jaw moved the clamp, applying a strain to the sample as shown in the inset of Figure 3.2(a). The stepper motor was in turn controlled by a circuit (Figure 3.2(b)) which allowed for

calibrated horizontal displacements of the clamp in step sizes of either 20 μm or 200 μm or continuous movement depending on the input to the circuit. Individual steps could be generated using lever switches while continuous movement used a press switch. Displacement step sizes of 200 μm could also be triggered by using an input from a controlling LabVIEW program with a time delay of τ between steps. The values of stress and strain within the GSC were calculated as shown in Section 2.5. This LabVIEW program was also used to continuously measure the 4T resistance of the sample. The direction of displacement was controlled using another switch.

A second experiment was carried out to more accurately measure the amplitude of the change in R directly after applying a strain relative to the strain's magnitude. Although this could be calculated from the strain change due to lower ρ shift in the first experiment, the presence of memory effects within the composite are likely to change the results obtained. Further, the strains obtained by this method are limited. Instead, we applied smaller strains using multiples of the 20 μm displacement step on the strain rig and gave the composite sufficient time to fully relax before applying a following strain. We used a range of strains limited to be within the range theoretically examined in Chapter 4 ($0 < \varepsilon_{xx} < 0.35\%$).

3.1.3 Measurement of piezoresistance rise time

As stated in Section 1.1, when measuring rapid changes it is necessary for pressure sensors to have fast response times. The stepper motor used in the first two experiments took seconds to apply the strain perturbations. Due to this, the set-up described in Section 3.1.2 was insufficient to measure the response time of the GSC, which is of the order of milliseconds. We used a separate rig, shown in Figure 3.3, to allow the application of a small, fast strain to the composite.

The sample was held in place at one edge by a clamp, labelled in

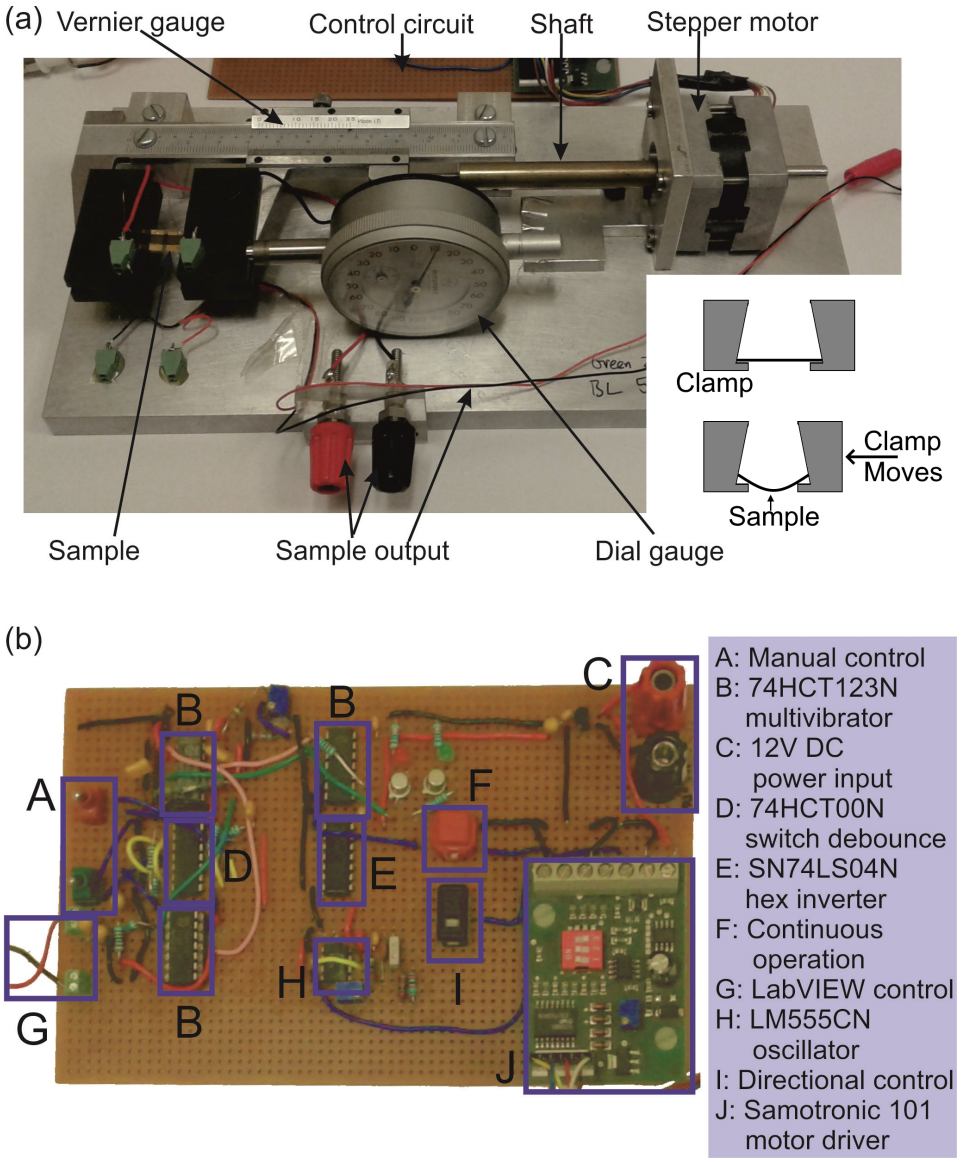

Figure 3.2: Experimental set-up used to test the response of the composite to stress. (a) The system used to apply horizontal compressions to a GSC sample. Inset: Schematic diagram of the sample before and after applying stress. (b) Details of the control circuit for the stepper motor shown in part (a).

Figure 3.3, and held above a groove. Although the acetate substrate is flexible, it holds its flat resting state and returns back to it when bent and released. To create an initial strain compressive in the x direction, the far edge of the composite was raised by placing a glass microscope slide in the groove below it. The strain applied was calculated from the thickness of the glass slide and could be increased by attaching thinner glass coverslips to the slide as shown in Figure 3.3(a). After giving the composite time to fully relax to the new baseline resistance, a rapid tensile strain was applied by removing the glass slide from under it and allowing the sample to spring back to its rest position. This unloaded the stress on the sample. The difference in positions of the glass and sample is shown in the schematic diagram in Figure 3.3(b). The slide was moved by applying a current to a piezoelectric actuator (Piezo Systems, PSI-5A4E), overbalancing a lever arm which in turn knocked the glass slide out of place. The piezoelectric actuator had a response time of 1 μs. [7]

We applied a constant current across the composite and constantly measured the voltage change across it using a DAQ card (NI-PCI6289) attached to a LabVIEW program using a sampling rate of 20kHz. This allowed us to calculate the change in $\Delta R/R$ from current-voltage laws. The response time t_r could then be read from the graph of R against time.

3.2 GSC piezoresistive responses to applied strain steps

3.2.1 Overall piezoresistive response through a cycle

Each stress increment is immediately followed by a rapid increase in GSC resistance, labelled with an S in Figure 3.4; followed by a gradual

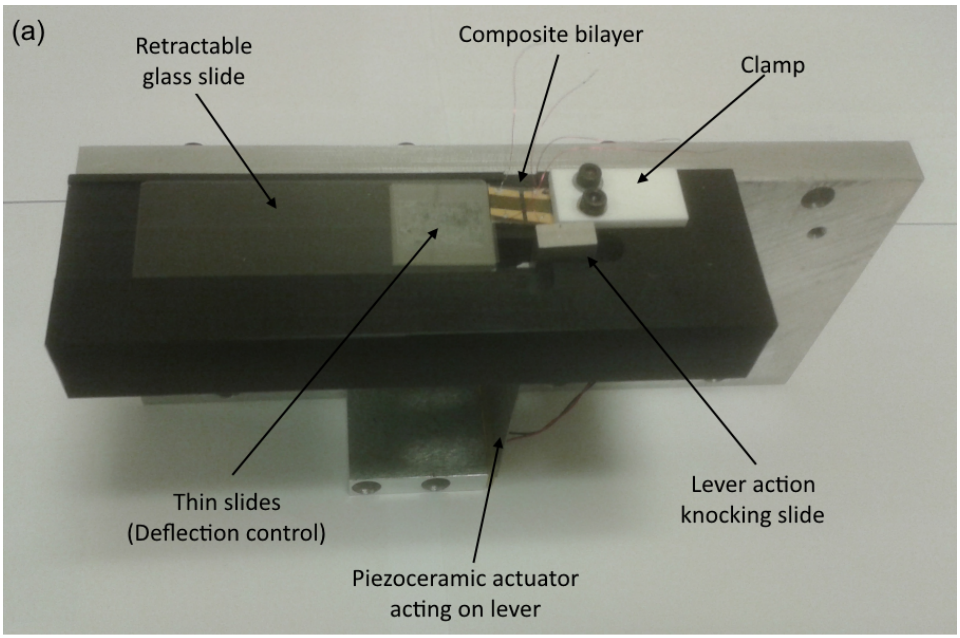

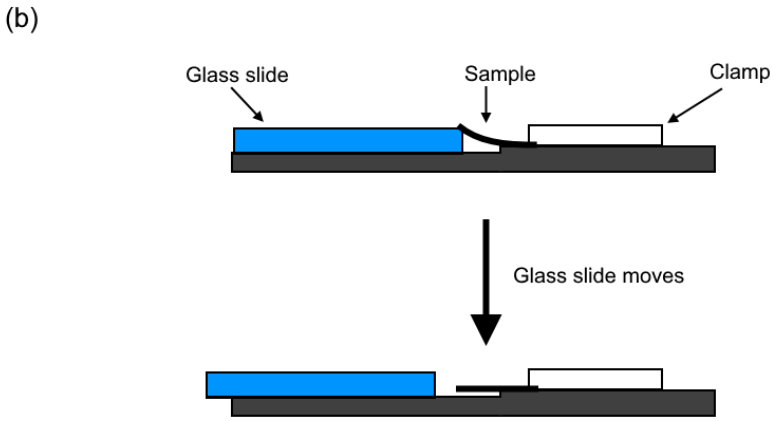

Figure 3.3: (a) The constructed rig used to apply a rapid strain over 1 μs to GSC samples. (b) Simplified cross-section of the clamp around the sample. The lever has been removed for visibility.

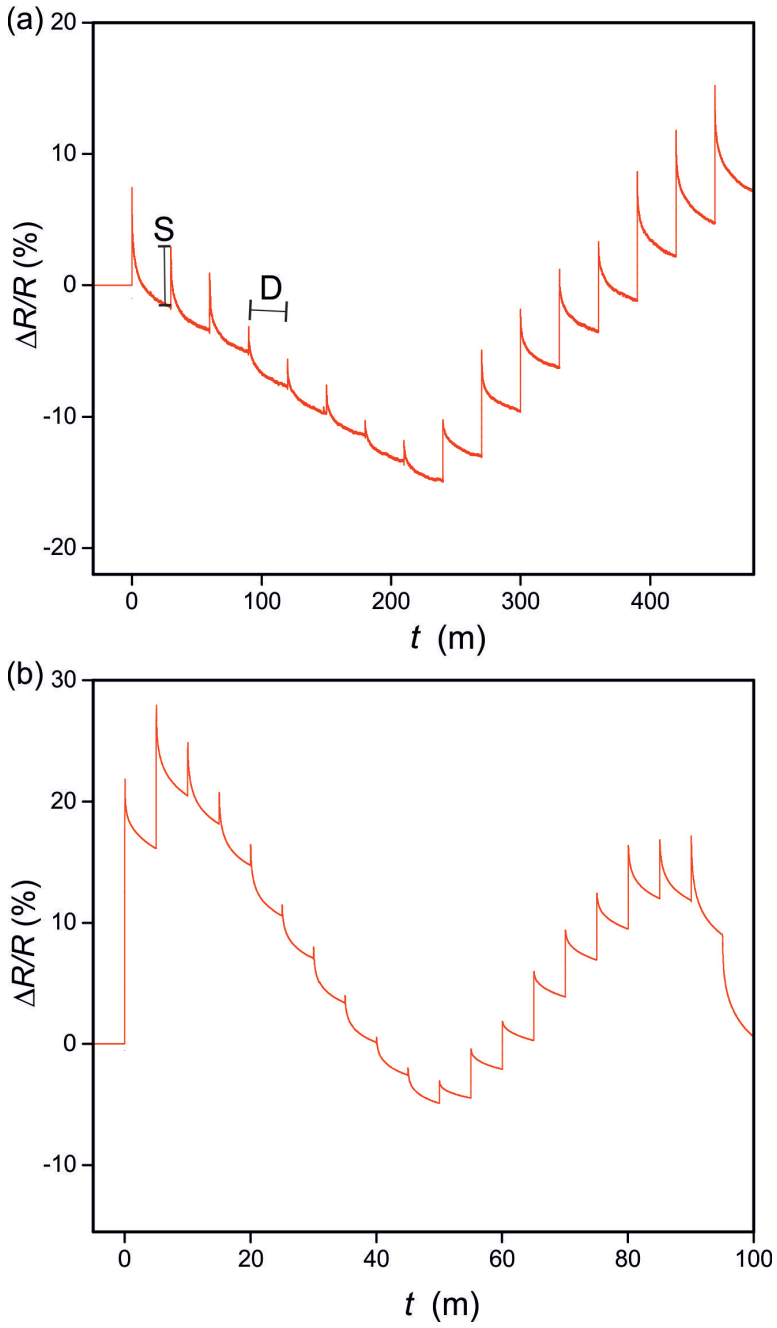

Figure 3.4: Proportional resistance change over stress loading-unloading cycles for a 28% graphite sample. Time allowed between steps: (a) $\tau = 30$ min (b)$\tau = 5$ min.

decay towards a new value, labelled with a D. This decay is analysed in detail in more detail in Section 3.2.3. Although R is measured in the x direction, the presence of the initial increase after a strain ε_{xx} is applied is seen both when σ_{xx} is increased and decreased. However, the new value of the baseline $R(t)$ decays towards decreases with compressive stress and increases with tensile stress. The shape of a resistance curve starting with decreasing ρ and then increasing ρ depends on the value of τ compared to τ_c. With low values of τ, the composite does not have sufficient time to relax close to its new baseline resistance. Over multiple steps, this builds up as an increasing memory effect leftover from previous strains, causing following spikes to reach a higher resistance. Identical changes in horizontal compression give smaller changes in ρ as ρ decreases and thus smaller strain changes, which results in the decay overpowering the spike effect on the overall curve as ρ decreases further. This effect is mirrored when ρ is increased, giving a curve with an overall M-shape across a full loading-unloading cycle. With larger values of τ, the resistance is able to reach a value closer to its new baseline after each increment. Due to this, a V-shaped overall curve is seen instead and memory effects are reduced.

The initial spike increases in R, marked with an S in Figure 3.4(a), are due to the instantaneous dynamic strain caused from the stress increment. The following resistance decay, marked with a D, then depends on the strain decay derived in Section 2.5. As compressive strain reduces the length of x-orientated bonds and extends y and z-orientated bonds, while tensile strains give the opposite effect, we can deduce from the symmetry of the R curve that bonds in all three dimensions are used by the current flow.

3.2.2 Strain dependence

According to the derivation in Section 4.1.2, the relationship between R and ε_{xx} should be exponential in nature. The first 15 seconds of

$\Delta R/R$ against time for three different strains applied to the same 28% HOPG sample are shown in Figure 3.5(a). The increasing effect on $\Delta R/R$ as strain step size increases can clearly be seen.

The dependence of the relative amplitude of resistance spikes on strain increment is shown in Figure 3.5(b) for 3 different samples of 28% HOPG concentration. The data set for sample 1 uses data collected from a strain loading cycle with $\tau = 5$ min, while the other two sets of points use small strains with the subsequent $\tau >> \tau_c$ to allow for complete relaxation of the GSC. Two exponential curves are also plotted for comparison.

It can be seen in Figure 3.5 that while the sample 1 measurements fit close to the exponential curve below 0.2% strain, the points at 0.29% and 0.51% are approximately double the exponential fit. Samples 2 and 3 follow an exponential dependence for a wider range of strain values. This is partially due to the value of τ used for sample 1 being short in comparison to the time taken for stress and strain to decay. This allows viscoelastic memory effects to remain in the GSC and affect the results from following strain increments. For all samples, the dependence begins to change more rapidly than the exponential when $\varepsilon_{xx} > 0.32\%$. This is likely due to the assumption that conducting percolation lines within the sample remain unbroken no longer holding true when the strain increment, and thus HOPG displacement, is larger. As some conducting bonds within the composite break due to the HOPG displacement, current is forced to either find an alternate route through the composite or abandon broken conduction lines completely where the tunnelling barrier becomes too wide for tunnelling events to occur with reasonable probability. This would lead to larger changes in resistance. As the data for sample 1 starts with a strain larger than this, memory effects from this can continue to affect the results for the following, smaller strain increments.

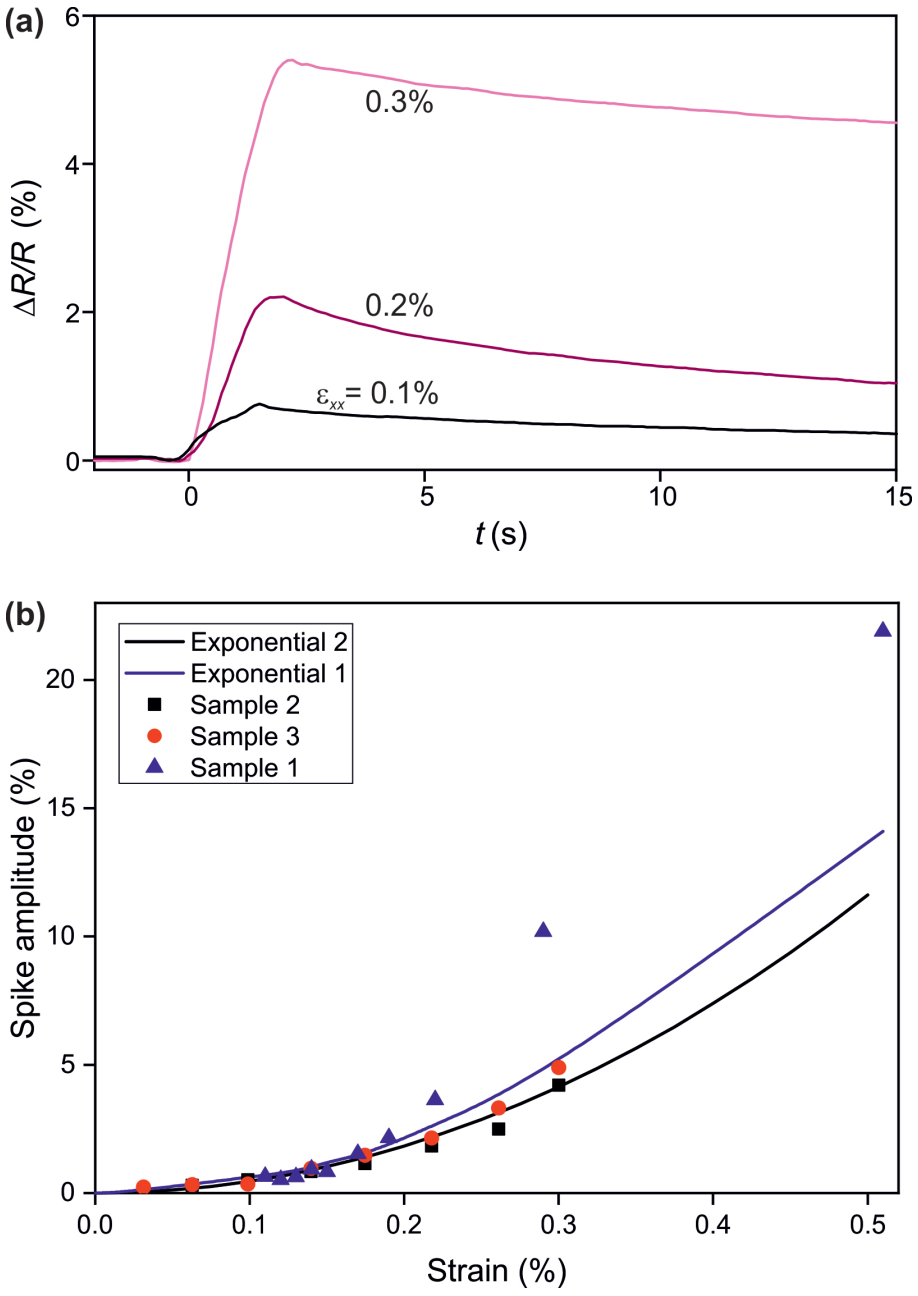

Figure 3.5: (a) Shape of the $\Delta R/R$ dependence on t after an initial x-strain of different values. Strain values used: 0.1%, 0.2% and 0.3%. (b) Dependence of the amplitude of resistance spikes of a 28% graphite sample on the size of the strain applied. $\tau = 5$min.

3.2.3 Response to stress and strain decay

Figure 3.6(a) shows the time decay of the normalised logarithm of GSC resistance following multiple stress increments. The majority of the curve (from approximately 20 s onward) is shown to be linear on a log scale. This implies a double exponential relationship between R and t, as would be expected from tunnelling theory. The first exponential comes from the dependence of tunnelling resistance on tunnelling distance and the second is demonstrated in Equations (2.28) and (2.29). The start of the curve ($t < 20$ s) exhibits a decay faster than the double exponential. This is likely due to the existence of other factors such as the breaking and mending of percolation lines. Despite different strains being applied to the GSC, there is little change in the gradient of the curves, implying the presence of a constant factor within the double exponential. This is as expected from Section 2.5, as the strain decays exponentially with time and resistance is exponentially dependent on strain as shown in Section 3.2.2.

In the range of concentrations used, there is no discernible dependence pattern of this double exponential decay on the value of ν. This can be seen in Figure 3.6(b), where there is little variation in the gradients of the curves plotted for different values of ν.

3.2.4 Concentration dependence

The $\Delta R/R$ spike amplitudes due to the initial strain increment and their following decays with respect to time for samples of 25%, 28% and 31% HOPG are shown in Figure 3.7. It is clear that samples with a lower volume concentration of HOPG display a greater $\Delta R/R$ response to the same strain increment than those with higher concentrations. This higher sensitivity in $\Delta R/R$ is caused by the larger separation distances between HOPG nanoparticles in the composite. As there are fewer HOPG particles, the separations between them are greater.

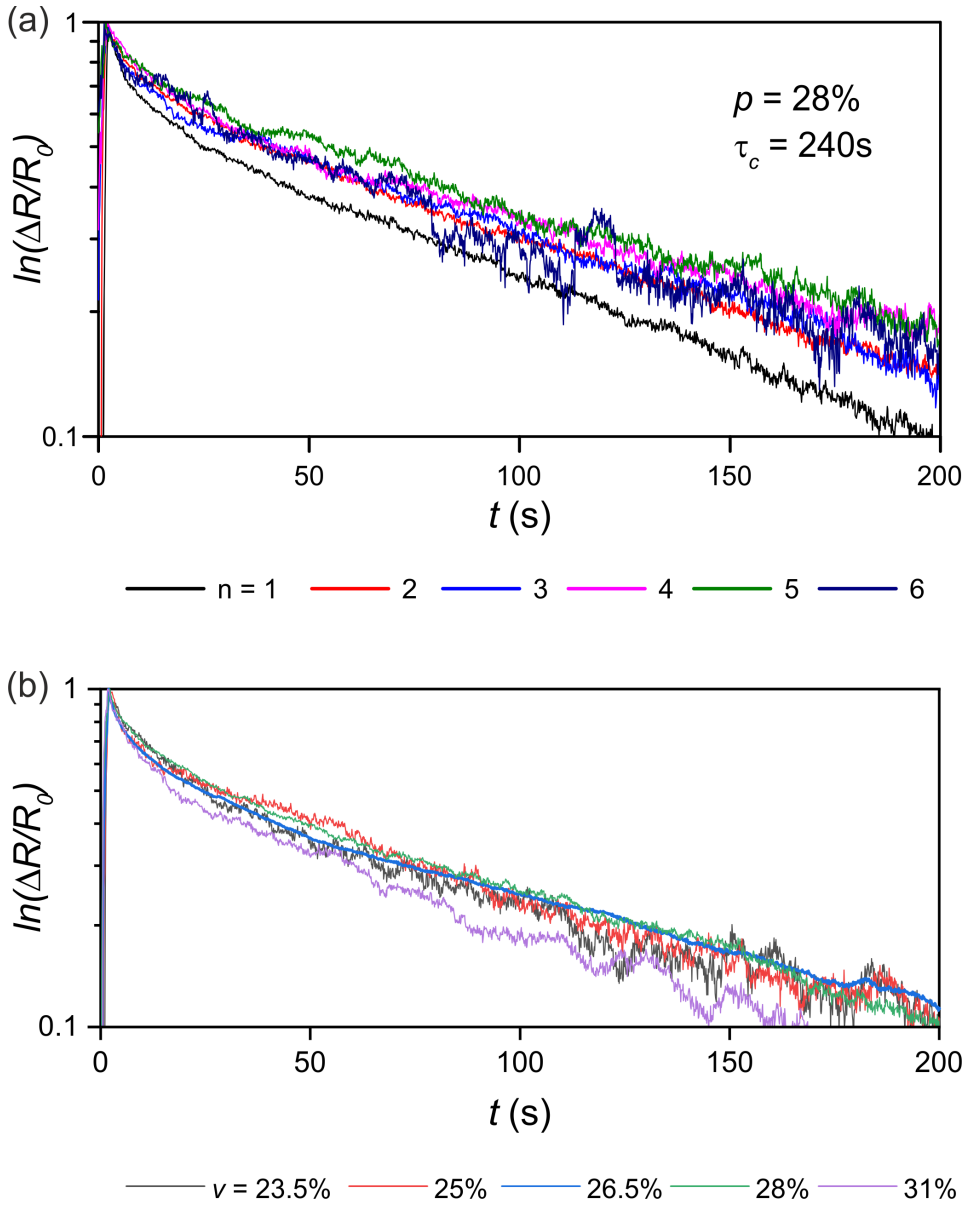

Figure 3.6: Time decay of the normalised logarithm of resistance change plotted on a logarithmic scale for (a) the first 6 stress increments in a loading cycle for a 28% graphite GSC and (b) composites of five different HOPG filling fractions. After 20 s the double logarithm is linear with respect to time.

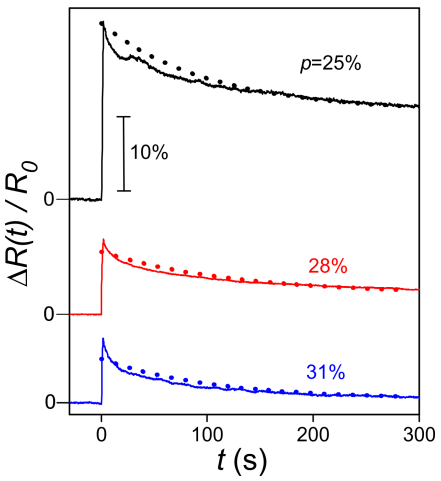

Figure 3.7: The resistance spike from the first compressive strain increment and its following decay for samples of 3 different graphite concentrations. The concentrations used are 25% (black), 28% (red) and 31% (blue). The dotted lines are double exponential fits to the decays in R.

Further, the movement of HOPG particles relative to each other when a strain is applied is also larger. These two factors, coupled with the exponential dependence of R on the tunnelling barrier width between particles lead to a greater ΔR.

3.2.5 Piezoresistance rise time

Examples of the response of R after a small, rapid (1 μs) strain is applied, with respect to t are shown in Figure 3.8(a). Three different graphite concentrations are used. The R increase is seen to be approximately linear and occurs within the first 2 ms for the samples shown. The following plateau is shown to contain some slight resistance fluctuations. These fluctuations in R may arise from a number of different sources. The first of these are oscillations within the GSC/acetate bilayer after it has reached its neutral point due to its excess momentum

after being released from its bent position. These small oscillations until the sample comes to rest are likely to cause a following, smaller increase in R. A second cause is noise within the circuit due to low bias voltages being used. As with larger strains, the resistance change is seen to be greater with lower concentrations of graphite within the sample.

The response time T_R for samples of 4 different graphite concentrations is shown in Figure 3.8(b). The overall trend shows that T_R increases as p_0 decreases. This is due to the lower concentrations of graphite particles resulting in a larger displacement of individual nanoparticles, taking longer to occur. All samples are shown to have a response time in the millisecond range. This is important as it allows for much faster measurement and repeats than the gradual exponential decay following after it. A measurable response within this time frame is vastly more practical for applications of a flexible strain sensor than one requiring multiple minutes. Although not the fastest flexible strain sensing device, [97] the GSC is shown to have a faster response time than a number of other sensors. [98, 99] Further improvements to both the response and recovery times could potentially be made by changing the materials within the composite.

3.3 Conclusion

In this chapter, we have observed the response of GSC samples to applied strains. We have seen that in response to a strain increment, the resistance first increases rapidly, with a response time in the range of 1 ms, before gradually decreasing with time according to a double exponential dependence. The value this decay approaches is either lower or higher than the initial resistance value, according to whether the strain is compressive or tensile respectively in the direction of current flow through the samples. The spike amplitude follows an exponential

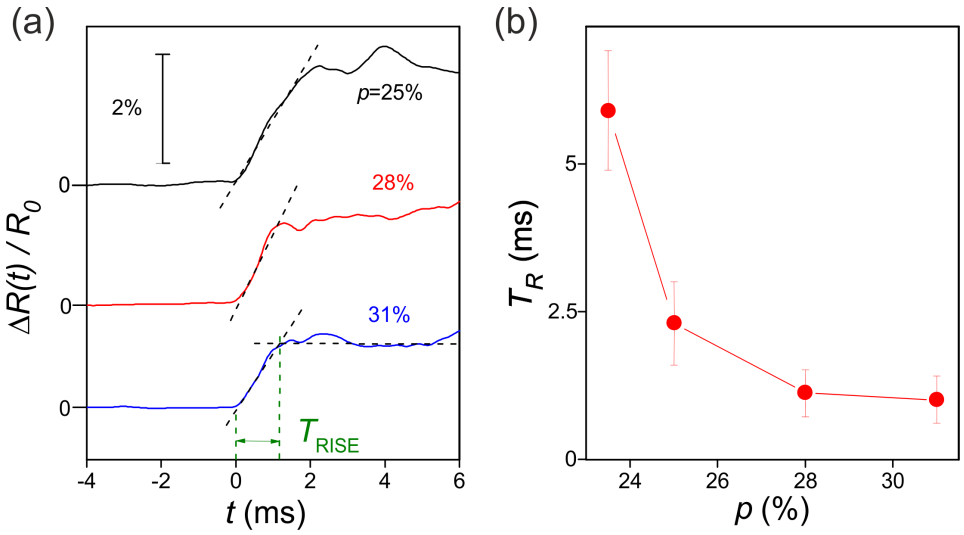

Figure 3.8: (a) The resistance change with time for 3 GSCs with different graphite concentrations when a small, fast stress (1 μs) is applied. (b) Average rise time, T_R for 4 samples with different graphite concentrations.

dependence on the magnitude of the strain applied and increases with decreasing volume fraction of HOPG above the critical filling fraction.

A theoretical model would help to explain these effects of strain on the composites. A basic theory is presented in Chapter 4 with this aim in mind.

Chapter 4

Tunneling-percolation network model of composite piezoresistance

4.1 Derivation

In order to explain the results seen in Chapter 3, a model was produced. The model was to produce a quick estimate of the time-dependant resistance change in response to a one-dimensional stress perturbation, without needing to calculate the positions and movements of individual conducting particles. The strain and stress relations to the radius of curvature derived in Section 2.5 and an effective medium approximation (EMA) to obtain the bond conductivity were combined to create a perturbative piezoresistance model. The theory is generalised to be applicable to composites of a similar nature, with varying spherical conductive materials and insulating polymers.

4.1.1 Average length of percolation bonds

When in the steady state, the conductivities of tunnelling bonds between particles in the composite follow a distribution [100] centred around the average bond conductivity g_0. This conductivity is calculated from the EMA and used to infer an average tunnelling barrier width between nearest neighbour conductive particles b_0. We will then compare this to the average interparticle distance $\bar{b}$. In three dimensions, the nearest neighbour probability distribution function $P(b)$ for randomly dispersed hard spheres of radius d can be written as [101,102]

$$\begin{aligned} P(b) =& \frac{24\nu\left(\gamma_1 X^2 + \gamma_2 X + \gamma_3\right)}{d} \exp[-8\nu\gamma_1(X^3-1) \\ & - 12\nu\gamma_2(X^2-1) - 24\nu\gamma_3(X-1)], \end{aligned} \tag{4.1}$$

where ν is the volume fraction of conductive nanoparticles, $X \equiv 1 + b/d$ and

$$\begin{aligned} \gamma_1 &= \frac{1+\nu}{(1-\nu)^3}, \\ \gamma_2 &= \frac{-(\nu/2)(\nu+3)}{(1-\nu)^3}, \\ \gamma_3 &= \frac{(1/2)\nu^2}{(1-\nu)^3}. \end{aligned} \tag{4.2}$$

The average tunnelling gap between neighbouring spheres can be obtained from an integration $\bar{b} = \int_0^\infty db\, bP(b)$. For HOPG nanoparticles of 450 nm diameter in the range of filling fractions $23.5\% < \nu < 32\%$, the average interparticle distance can be approximated by $\bar{b} \approx d/4[(\pi/6\nu)^{1/3} - 1]$ [8] to within a few percent. This results in a value of $\bar{b}$ varying between 20 and 34 nm as ν decreases from 32% to 23.5%. Values of ν within this range are most relevant to GSCs similar to the ones described in Section 3 as $\nu = 23.5\%$ is the critical value for percolation, ν_c while $\nu = 32\%$ is the miscibility threshold.

We calculate the average length of conductive interparticle bonds used in percolation lines b_0 from the average EMA conductivity of a three dimensional tunnelling-percolation network, [10, 100]

$$\int_0^\infty db\, \frac{P(b)}{g(b)+2g_0} = \frac{p-p_c}{2g_0 p}, \tag{4.3}$$

where p is the bond occupancy probability and p_c its critical value for tunnelling-percolation. These values correspond to ν and ν_c. As in the composite modelled, $\nu_c = 23.5\%$ is not vanishingly small, a reasonable approximation can be made by substituting in $(\nu-\nu_c)/\nu$ for $(p-p_c)/p$ in Equation (4.3). [10, 12]

The conductivity of the tunnelling barrier $g(b)$ between neighbouring spheres was calculated using the tunnel current density through a rectangular barrier as demonstrated by Simmons [70, 72],

$$J(b) = \frac{3}{4\pi} G_0 \kappa \frac{e^{-2\kappa b}}{b} V, \tag{4.4}$$

where $G_0 = 2e^2/h$ is the quantum conductance and κ is the inverse of the tunnel decay length, equal to

$$\kappa = \sqrt{\frac{2mV_0}{\hbar^2}} \tag{4.5}$$

for charge carriers of effective mass m and a potential barrier of height V_0 and width b. Integrating Equation (4.4) over the cross-sectional area Figure 4.1 gives the tunnel current between spheres:

$$I = \int_0^{2\pi} d\phi \int_0^{\pi/2} d\theta \left(\frac{d}{2}\right)^2 \sin\theta\cos\theta J[s(\theta)], \tag{4.6}$$

where $s(\theta) = b + d(1-\cos\theta)$ is the tunnel gap at angle θ relative to the axis of symmetry. Following through, the equation for bond conductivity is obtained as:

$$g(b) = \frac{3}{16} G_0 \left(u_T \int_{u_T}^{u_T} du\, \frac{e^{-u}}{u} + e^{-u_T} - e^{-u_L} \right), \tag{4.7}$$

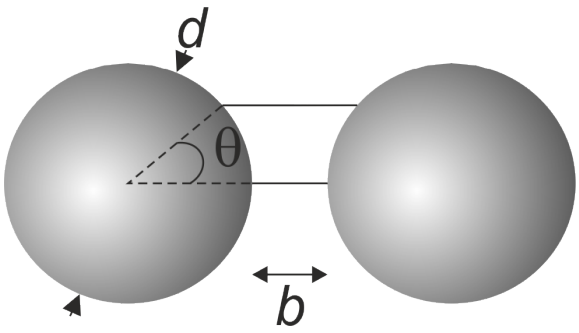

Figure 4.1: The width of the tunnelling barrier between two different spherical conducting particles varies depending on the values of b and d as well as the point on the sphere surface that an electron tunnels from.

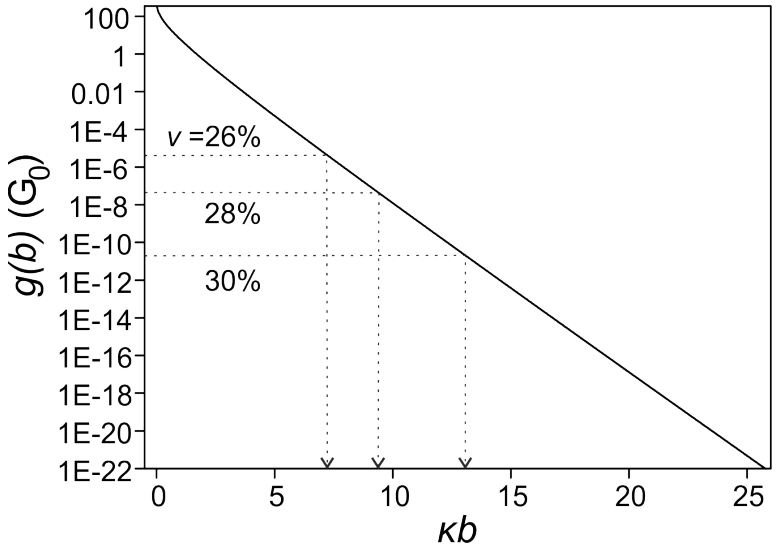

Figure 4.2: Conductivity of the bond between conductive nanoparticles for varying κb.

where $u_L = 2\kappa b$ and $u_T = 2\kappa(b + d)$.

Figure 4.2 plots $g(b)$ as a function of the dimensionless parameter of inverse tunnelling length multiplied by barrier width. [10] Substituting Equation (4.7) into Equation (4.3) allows for g_0 to be calculated. Using three example filling fractions of $\nu_0 = 26\%, 28\%$ and 32% for nanoparticles 100 nm in diameter, we can read values of κb_0 off the horizontal axis in Figure 4.2. This gives values for κb_0 of 7.23, 9.4 and 13.1 for 30%, 28% and 26% respectively. Comparing the barrier widths of these tunnelling bonds to the average interparticle distances calculated from filling fractions show them to be shorter. The calculated values for $\kappa\bar{b}$ are 17.2, 19.6 and 22.2 respectively for 30%, 28% and 26%.

4.1.2 Perturbative piezoresistance model

The final step of the derivation is to calculate the effect of the strain increments on composite resistance. We start by assuming that a small (<0.5%) strain allows us to neglect the potential re-routing of percolation paths and also that all conducting bonds are of similar length before applying any stress increments. The length of conduction bond k in percolation path l is b_{kl} and initially all $b_{kl} \simeq b_0$. Applying a strain increment will change the interparticle distance $b_0 \to b + \Delta b_{kl}$ where b is the new mean interparticle separation and Δb_{kl} the relative change in b_{kl}. Assuming each percolation line has K bonds within it, we can apply Kirchhoff current and voltage laws to L parallel percolation lines spanning the composite. This gives a conductivity of

$$G = \sum_{l=1}^{L} \frac{b_0^{-1} \exp(2\kappa b_0)}{\sum_{k=1}^{K} b_0^{-1} \exp(2\kappa b_{kl})} g_0(b_0), \tag{4.8}$$

where $g_0(b_0)$ is the EMA conductivity in the initial state. We make the substitution $b_0 \to b + \Delta b_{kl}$ in Equation (4.8) and retain the first-order terms in $\Delta b_{kl}/b_0$. This gives the conductivity to a first order

approximation in strain as a product of two terms:

$$G = G_s(b) P \Gamma_d, \tag{4.9}$$

where $G_s(b) = (L/K) g_o(b)$ is the new baseline conductivity of the composite and is defined by the new average particle separation b. Γ_d is dimensionless and describes the transient dynamics of the system:

$$\Gamma_d = \frac{1}{L} \sum_{l=1}^{L} \frac{1}{\frac{1}{K} \sum_{k=1}^{K} \exp\left(2\kappa b \frac{\Delta b_k l}{b}\right)}. \tag{4.10}$$

As the composite films used in Chapter 3 are several orders of magnitude larger in length than the average percolation bond ($d + b \approx$ 600 nm), $K \sim 10^4$ at least in each tunnelling-percolation path. Due to the large value of K, we are able to replace the discrete sum over k with a continuous integral over the 4π solid angle. This gives a resistance of

$$R(t) = \frac{R_s(b)}{4\pi} \int_0^{2\pi} d\phi \int_0^{\pi} d\theta \, \sin\theta e^{2\kappa b \frac{\Delta b(\theta,\phi,t)}{b}} w(\theta, \phi), \tag{4.11}$$

where $R_s(b)$ is the inverse of $G_s(b)$, $w(\theta, \phi)$ is a weight function used to describe the anisotropy of the hopping rate and described below and $\Delta b(\theta, \phi, t)$ is the magnitude of a change in bond length. $\Delta b(\theta, \phi, t)$ is related to the orientation of the bond in dynamic strain through the equation

$$\frac{\Delta b(\theta, \phi, t)}{b} = \frac{\sqrt{\sum_{\alpha=x,y,z} (b_\alpha = \Delta b_\alpha)^2} - b}{b} \simeq \boldsymbol{n}^T \boldsymbol{\varepsilon}^d(t) \boldsymbol{n}, \tag{4.12}$$

where $\boldsymbol{n} \equiv (\sin\theta\cos\phi, \sin\theta\sin\phi, \cos\theta)$ is the unit vector and $\boldsymbol{\varepsilon}^d$ is the dynamic strain given by Equations (2.27) and (2.28). Two examples of the weight function $w(\theta, \phi)$ are considered in Section 4.2.2. They are $w(\theta, \phi) = 1$, which assumes a tunnelling probability equal in all

directions and $w(\theta, \phi) = 2 \sin\theta \, |\cos\phi|$, which gives more weight to the tunnelling probability in the x direction.

The change in baseline resistance $R_s(b)$ can now be calculated. R_s is the inverse the static conductivity of the composite $G_s \ (\nu - \nu_c)^\alpha$. A change in the tunnelling barrier width $b_0 \to b = b_0(1+\varepsilon^s_{xx})$ is related to a change in the filling fraction $\nu_0 \to \nu$. For the GSC samples used, this is done using the relationship between average barrier width and filling fraction $b \simeq d/4[(\pi/6\nu)^{1/3} - 1]$. [8] The new effective filling fraction can be calculated as

$$\nu \simeq \nu_0 \left[1 - 12 \frac{b_0/d}{1 + 4b_0/d} \varepsilon^s_{xx} \right]. \tag{4.13}$$

The resulting ν is then inserted into the static conductivity to obtain its relation with static strain:

$$G_s(\nu) \simeq G_s(\nu_0) \left(1 - 12 \frac{\nu_0}{\nu_0 - \nu_c} \frac{b_0/d}{1 + 4b_0/d} \alpha \varepsilon^s_{xx} \right). \tag{4.14}$$

This can be rewritten by substituting in $b_0 \simeq d/4[(\pi/6\nu_0)^{1/3} - 1]$ to get the steady state resistance normalised by the initial resistance as

$$\frac{R_s(b)}{R_s(b_0)} \simeq 1 + 3 \frac{\nu_0}{\nu_0 - \nu_c} \left(1 - \left[\frac{6\nu_0}{\pi} \right]^{1/3} \right) \alpha \varepsilon^s_{xx}(t). \tag{4.15}$$

There are two notable predictions of Equation (4.15). The first is that the baseline resistance depends linearly on stress. This is in good agreement with experimental observations in Section 3.2 and Figure 3.4. The second is that the rate of change of the baseline resistance will become increasingly steep as ν_0 approaches ν_c.

The output results of this theory are compared to the experimental results obtained from Chapter 3 and analysed further in Section 4.2.

4.2 Results

4.2.1 Predicted piezoresistance through a complete strain cycle

As described in Section 4.1.2, percolation bonds aligned with the compressive component of the applied strain will shrink and thus become more conductive. Bonds aligned with the tensile components of the strain extend and therefore increase in resistance. Due to the exponential dependence of tunnelling resistance on barrier width, these bonds form resistance bottlenecks and have a larger initial effect on resistance than the compression-aligned bonds. Changing from decreasing the curvature radius ρ to increasing ρ swaps the directions of compression and extension. This section first describes the overall resistance pattern of a stress loading-unloading curve, then explores the symmetry of the composite piezoresistance using the weight function.

Fitting with what is observed experimentally, resistance spikes are seen after a strain is applied. The first 10 of these spikes seen in Figure 4.3(a) are described by the following picture. These are generated by the effects of the three dimensional strain field on the tunnelling percolation network. Decreasing ρ elongates the tunnelling percolation bonds in the y and z directions as seen Figure 2.8. These bonds become the weak links in the percolation path due to their exponential increase in resistance. The resultant resistance bottlenecks determine the overall resistance of percolation paths and the composite as a whole. Bonds more closely aligned to the x direction are compressed and therefore have their resistance contribution decrease exponentially. The percolation network relaxes to a new steady state over time t between these stress-induced spikes.

The second half of 4.3(a) shows 10 resistance spikes that occur when stress is unloaded and the composite is moved back towards its flat

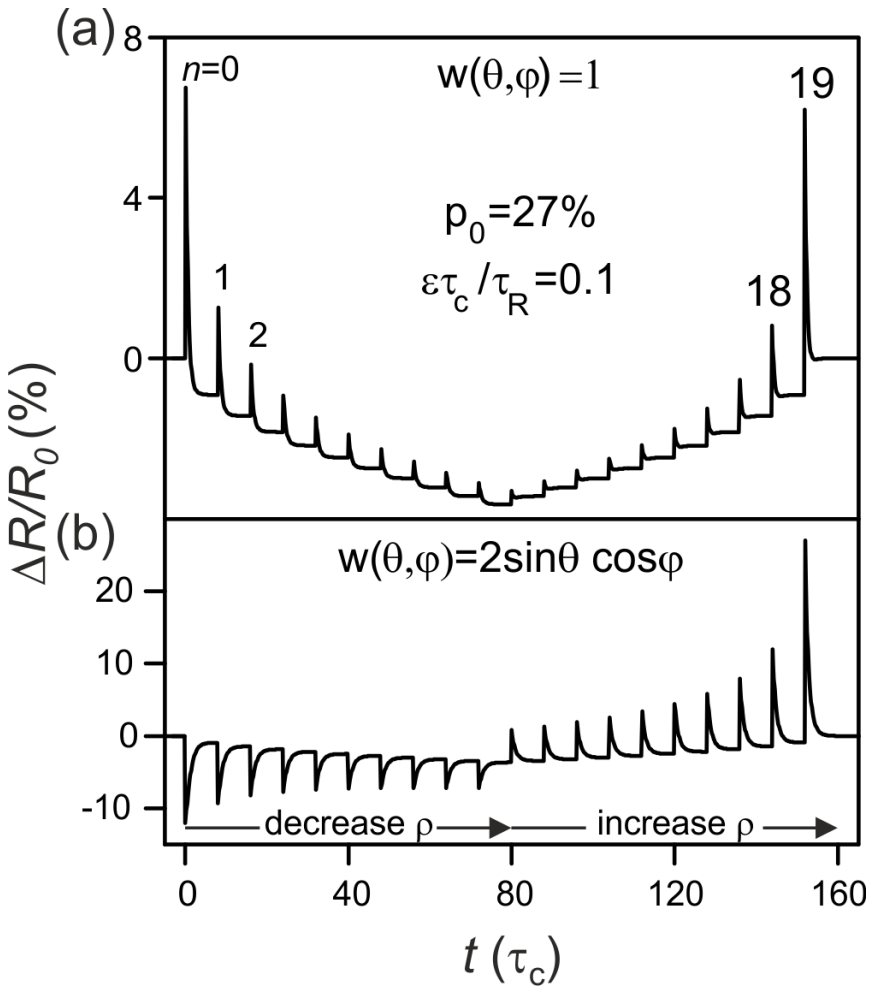

Figure 4.3: Variation of resistance against time over a full stress loading-unloading cycle for two different weight functions. (a) $w(\theta, \phi) = 1$. (b) $w(\theta, \phi) = 2 \sin\theta \, |\cos\phi|$.

state. Due to the change in sign, x direction bonds are now elongated and the cause of resistance spikes, with bonds aligned in the y and z directions contributing exponentially smaller to the resistance. The weight function used in Figure 4.3(a) assumes an isotropic hopping rate ($w(\theta, \phi) = 1$), which results in predicted resistance spikes symmetrical with respect to stress loading and unloading. The resistance increases equally with resistance bottlenecks created with different orientations and at different locations. By comparing to Section 3.2, we can see that this situation matches well with experimental observations.

Contrasting with this, a weight function assuming a directional hopping preference predicts a piezoresistance strongly asymmetrical over the same loading-unloading cycle. This is demonstrated in Figure 4.3(b), which models hopping directed by the measurement electric field, (where $w(\theta, \phi) = 2 \sin\theta \, |\cos\phi|$) giving x-orientated bonds most control over the resistance. The first 10 resistance spikes, when stress is loaded in the x direction, are seen to be negative due to compression of the bonds in this direction, before relaxing back up towards the new baseline resistance. Resistance spikes caused by unloading stress are positive, similar to Figure 4.3(a), caused by the expansion of bonds in the x direction. However, the spikes in Figure 4.3(b) are greater in amplitude than the spikes in Figure 4.3(a). This is because there is less weight given to bonds in the z direction, resulting in the resistance increases in the x-orientated bonds not being compensated for.

As all results observed in Section 3.2 show resistance symmetry through stress loading-unloading cycles, the tunnelling rate is implied to be isotropic.

4.2.2 Theoretical fits of experimental piezoresistance

Figure 4.4 contains comparisons of the model results with experimental results as found in Chapter 3. The graphite filling fraction in the

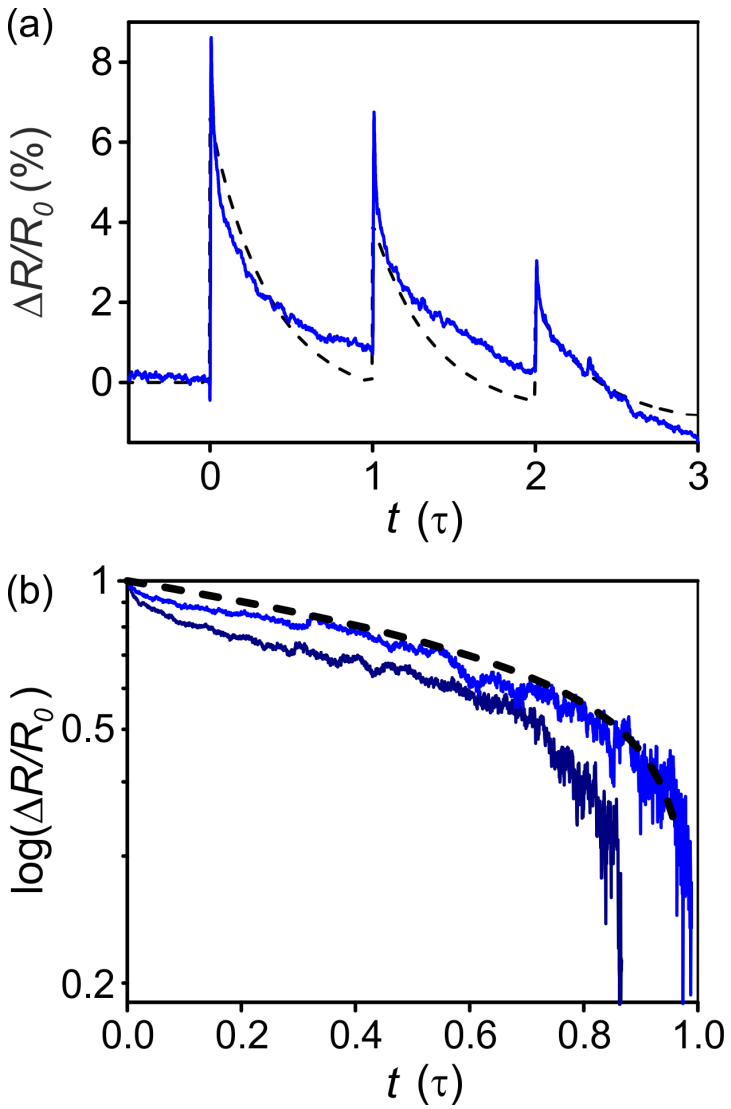

Figure 4.4: (a) Linear plot of the relative resistance change against time over three stress increments for both experimental and modelled results. (b) Comparison of the double exponential resistance decay against time for both model and experiment. The HOPG filling fraction is 31%. Solid blue lines are experimental results while the dashed black line is the model.

sample used is 31%. The model uses parameter values of $\tau_c = 180$ s and $\varepsilon = 0.1$ to fit the experiment as closely as possible over three stress increments. Figure 4.4(a) shows a linear comparison of ΔR with time while part (b) compares the rate of resistance decay of the model and the first two stress increments from the experiment.

Qualitatively, the model follows the experiment well in Figure 4.4(a). However, noticeable errors can be seen when following more quantitatively. The decay rate of the model does not match that of the experiment, which leads to different values after a time of τ has elapsed. This then causes the resistance spikes to begin at different values and the series of inaccuracies to build up over multiple stress increments. Due to this, modelling over multiple consecutive stress increments becomes increasingly difficult. The model can follow a single strain more accurately.

Some explanation for the discrepancy in decay rate can be seen in Figure 4.4(b). While the model can match the rate of decay accurately in the double exponential region, the experimental curve does not follow a double exponential decay for all values of t following an applied strain. The experimental resistance drops more rapidly to begin with. The absence of this in the model is most likely due to the assumption that all bonds within the composite remain unbroken under the small strains applied. In reality, some tunnelling bonds within the percolation lines across the composite may extend to lengths where tunnelling events are too unlikely to occur in comparison to other bonds. Due to this, alternate percolation lines are followed by the current instead. The relaxation of these bonds and change back to current following the original percolation lines could explain the more rapid initial experimental decay. A second, smaller factor could be variation of the initial tunnelling barrier width around b_0 in real samples.

Parameters of GSCs with different filling fractions extracted from fitting the model to experimental results are shown in Table 4.1. The

ν_0 (%)	V_0 (eV)	τ_c (s)	ϵ
23.5	0.225 ± 0.035	200 ± 30	0.11 ± 0.025
25	0.246 ± 0.035	200 ± 30	0.07 ± 0.025
26.5	0.281 ± 0.035	225 ± 30	0.07 ± 0.025
28	0.216 ± 0.035	240 ± 30	0.11 ± 0.025
31	0.268 ± 0.035	175 ± 30	0.10 ± 0.025

Table 4.1: Extracted parameters from experimental results for five different HOPG filling fractions, using $m = 0.1m_0$.

parameters extracted are the tunnel barrier height through the silicone V_0, the creep time τ_c and the residual creep factor ε. The value for m used is $0.1m_0$, where m_0 is the electron mass. Despite a wide variation within the error limits, none of the parameters are observed to vary with ν_0. This is as expected for V_0, as the tunnel barrier consists of the same material in all cases. The lack of change in τ_c and ε imply that these parameters are mostly determined by the silicone matrix within the range of ν_0 examined.

4.2.3 Dependence on delay between stress increments

Varying the interval between stress steps τ relative to the viscoelastic creep time τ_c, allows for the viscoelastic memory of the composite to be examined. It can be seen from Figure 4.5 that for shorter values of τ such as $0.5\tau_c$, there is incomplete relaxation between stress-steps, resulting in an M-shaped curve. This agrees qualitatively with the experimentally observed results. When sufficient time for complete relaxation of stress is allowed, the resistance pattern evolves towards a V-shaped curve. This is demonstrated in Figure 4.5 for $\tau = 3\tau_c$ and is also observed experimentally.

As can be seen in Figure 4.5, the quantitative details do not fit

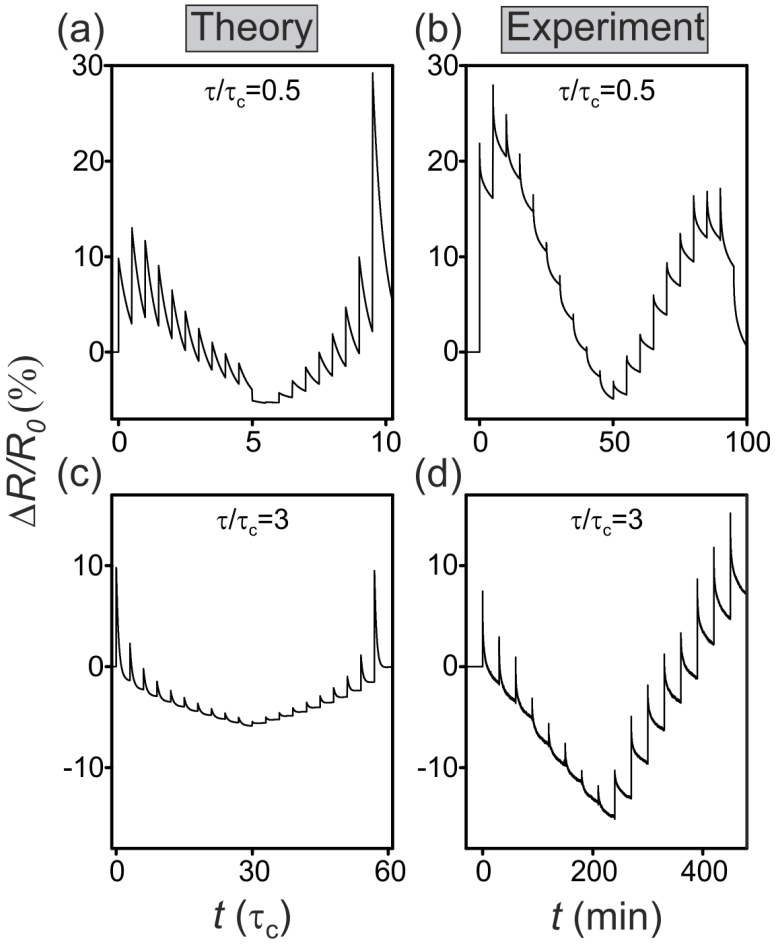

Figure 4.5: Variation of resistance against time over a full stress loading-unloading cycle for two different values of τ/τ_c for both experimental and theoretical model results. (a) Theory $\tau/\tau_c = 0.5$. (b) Experiment $\tau/\tau_c \simeq 0.5$. (c) Theory $\tau/\tau_c = 3$. (d) Experiment $\tau/\tau_c \simeq 3$. Other model parameters: $\nu_0 = 28\%$, κ =0.65 nm^{-1}, $\epsilon = 0.2$. Experimental $\nu_0 = 28\%$.

as accurately over a cycle with multiple strain steps as variations can be seen in the magnitude of ΔR. The main factor causing this is the assumption in the theory that all percolation paths are merely perturbed, with no existing paths being broken and no new paths being formed. The inaccuracy of this assumption is most evident immediately following the larger, initial strain steps, but is able to create a lasting and growing error as more strain increments are modelled.

A second inaccuracy in the theory is the presence of an excessively large final strain spike as ρ is returned to its initial value in the case of $\tau < \tau_c$. This arises from the above error combined with the accumulated effect of residual strains within the model.

4.2.4 Piezoresistance dependence on input parameters

The effects of different composite mixtures on the resistance dependence can be predicted by varying the material parameters within the model.

Variation in the dimensionless parameter $\varepsilon\tau_c/\tau_R$, which appears in Equation (2.29), allows for probing the effects of incomplete stress relaxation. Figure 4.6 shows the resistance pattern over a stress cycle when increasing this parameter from 0 to 0.3. The incomplete stress relaxation has no effect on the resistance spike amplitudes, but does effect the baseline resistance change. Incomplete stress recovery causes stress accumulation and decreases the interparticle tunnelling distances with each compressive step, resulting in a larger baseline resistance change with larger $\varepsilon\tau_c/\tau_R$.

Figure 4.7 shows the resistance dependence of the composite on ν_0 between 26% and 30%. Increasing ν_0 decreases the relative amplitude of resistance spikes when compared to the baseline resistance. This is due to the shortening of the tunnel barrier between graphite particles when their filling fraction is increased. The effect of this is that

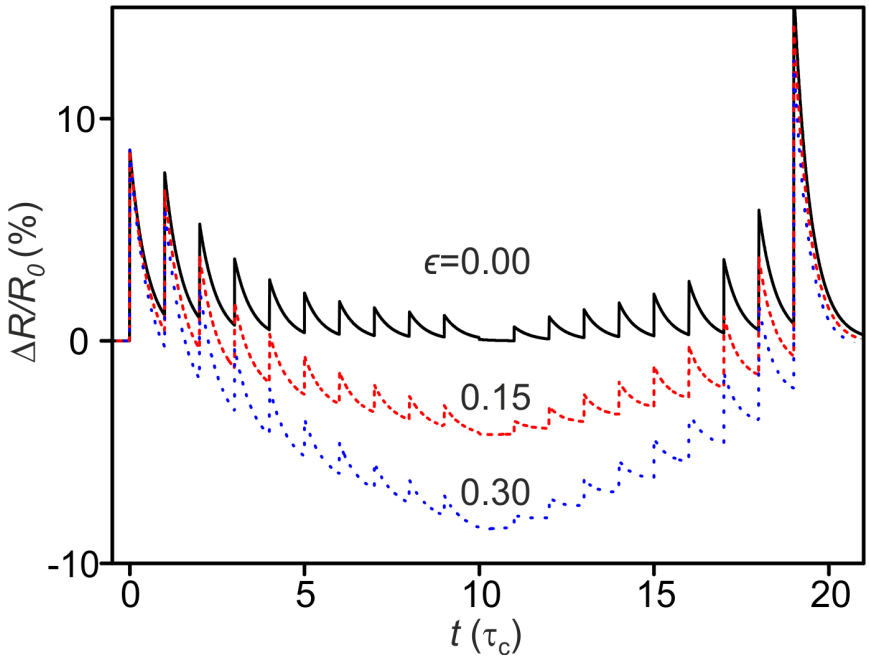

Figure 4.6: Resistance against time over a full stress loading-unloading cycle with varying residual stress $\epsilon = 0.00, 0.15$ and 0.30. Other model parameters: $\tau = \tau_c$, $\nu_0 = 28\%$, κ =0.65 nm^{-1}.

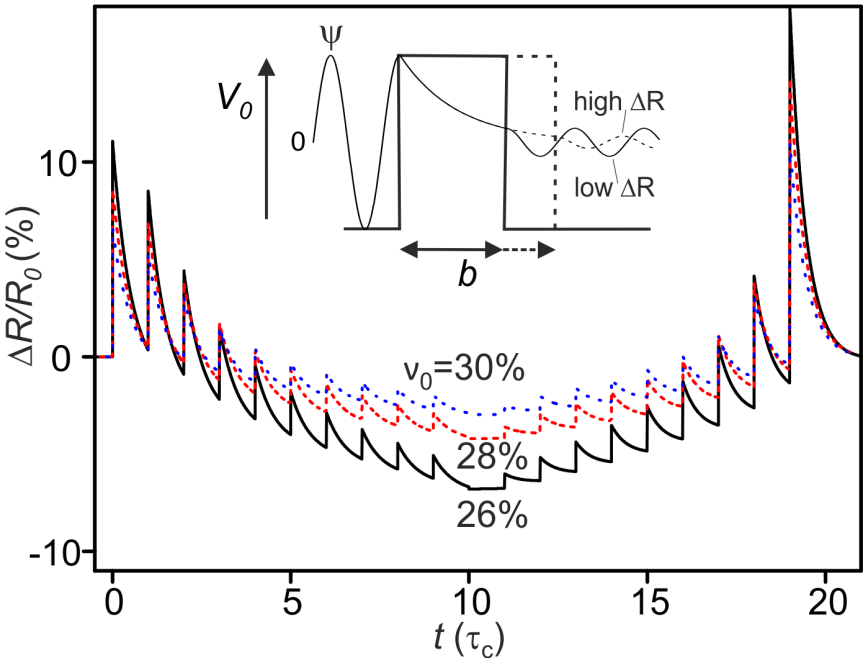

Figure 4.7: Change in the resistance over time during a stress loading-unloading cycle for samples modelled with different graphite filling fractions $\nu_0 = 26\%, 28\%$ and 30%. Other model parameters: $\tau = \tau_c$, κ =0.75 nm^{-1}, $\epsilon = 0.1$.

an identical applied strain produces a greater absolute change in barrier width for lower values of ν_0, thus resulting in a greater resistance change. The baseline resistance shift also varies with ν_0. Lower values of ν_0 cause $R_s(b)$ to drop more rapidly as the strain prefactor diverges when ν_0 approaches ν_c. This can be seen in Equation (4.15).

The resistance curve changes with tunnelling barrier height V_0 as well as width. This is shown in Figure 4.8, which plots the theoretical resistance pattern over a loading-unloading curve for three different values of the inverse tunnelling length $\kappa = 0.5, 0.75$ and 1.0 nm^{-1}. The change in κ can be linked to a change in V_0 through Equation (4.5). Increasing κ results in resistance spikes of greater amplitude when stress increments are applied on an exponential scale. This allows

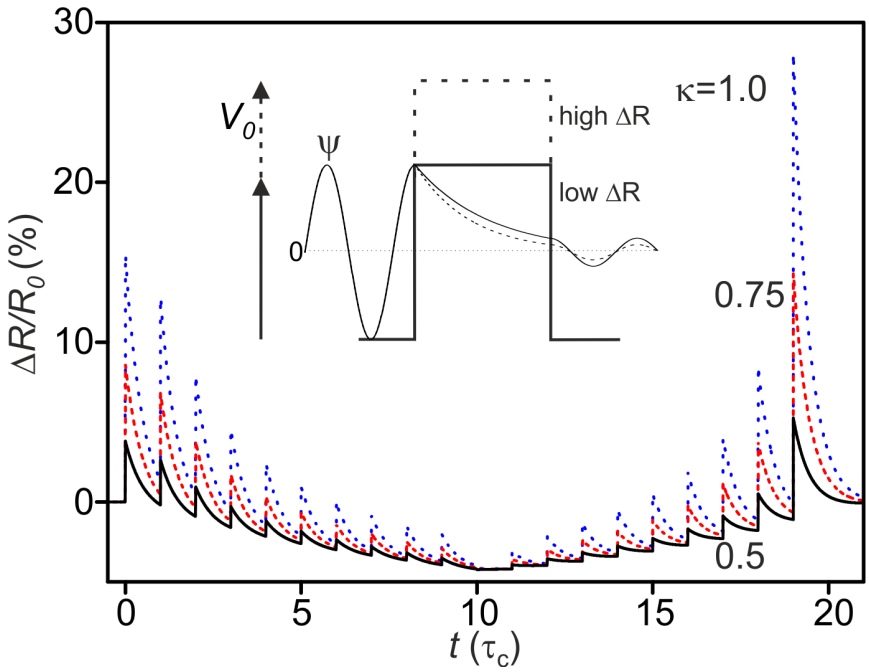

Figure 4.8: Resistance change over a stress loading-unloading cycle for samples modelled with different inverse tunnel lengths $\kappa = 0.5$, 1.0 and 30 nm^{-1}. Other model parameters: $\tau = \tau_c$, $\nu_0 = 28\%$, $\epsilon = 0.1$.

for greater sensitivity to stress at higher values of κ. Unlike variations in ν_0, the change in baseline resistance over a stress cycle is unaffected by changes in κ.

4.2.5 Dependence on strain

The height of resistance spikes is plotted against strain magnitude in Figure 4.9. This serves to measure the dependence of the piezoresistance on strain. The lines show the calculated piezoresistance for varying values of barrier height V_0 using Equation (4.11). These curves demonstrate that the sensitivity to stress may be increased by choosing composite materials with a large band offset between the nanoparticles and polymer. This could allow for mixtures more sensitive than

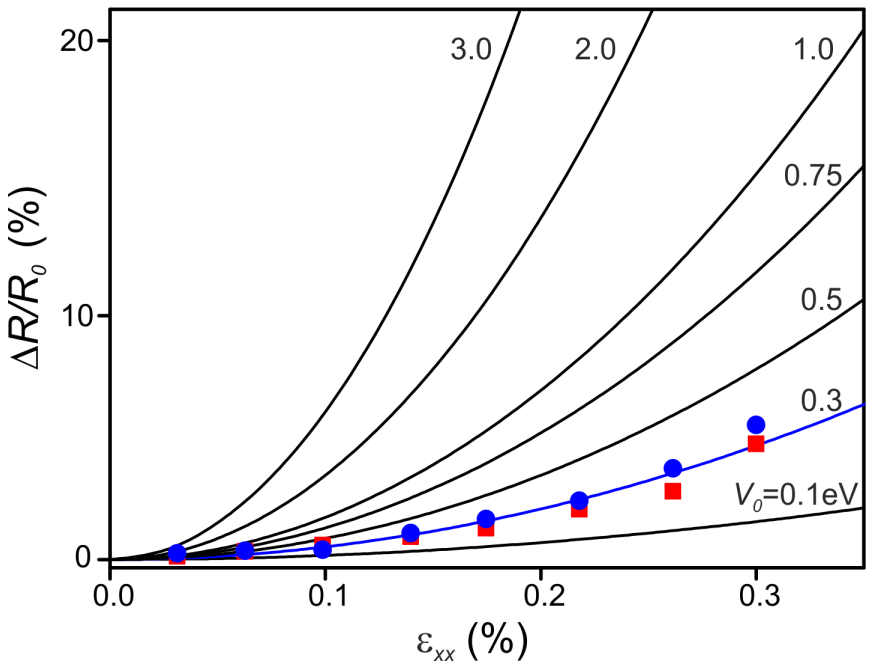

Figure 4.9: Resistance spike amplitude relative to strain for varying values of tunnelling barrier height V_0 (lines) and experimental results for two different samples (symbols).

the GSC used. The relation also shows a larger change in resistance with strain than inorganic crystal within the low strain region (<0.5%) [103–105]. By comparing the calculated results with those observed experimentally, a tunnelling barrier height can be extracted for composites using the line of best fit. Two GSC samples are plotted using the circular and square symbols, with both fitting closest to the line giving a barrier of $V_0 \approx 0.3$ eV.

4.3 Conclusion

This chapter has compared experimental results to a model for the time-dependent resistance change in response to stress perturbations and studied the further predictions of the model.

The model is derived from EMA and tunnelling-percolation theories in composite materials. It is able to qualitatively predict the resistance curve in response to multiple bilayer strain perturbations. Fair quantitative accuracy may be obtained from fitting to the resistance change from a single stress perturbation. From fitting the model results to those obtained from experimental curves, parameters from the composites can be obtained. Parameters from the GSCs synthesised in Chapter 3 were extracted using this method. By using these parameters along with the predicted dependencies on them, new composites with desired properties can be designed.

The model does not quantitatively fit well to multiple stress perturbations due to the assumptions used in it. The main cause of these inaccuracies is in the assumption that percolation paths through the composite remain unbroken due to low strain. A model accounting for the breaking and creation of percolation paths could provide more accuracy at the cost of modelling speed.

Chapter 5

Perpendicular transport in a graphene naphthalene diimide graphene multilayer.

5.1 Methods

5.1.1 Fabrication of multilayer

Following the results in Chapters 3 and 4, we began work on a nanofabricated device designed to have similar properties to the composite materials. The design was influenced by previous graphene tunnelling structures [16]. Our nanofabricated device consists of a multilayer stack of thin materials on an insulating substrate. The top and bottom layers of this stack are both monolayer graphene acting as electrodes. The graphene layers were purchased from Graphenea before being patterned as shown in 5.1(a) and arranged in a cross formation to allow transport from one layer to the other. The remaining layers act as a tunnelling barrier separating the graphene electrodes. These consisted of two layers of naphthalene diimide pyridine ($C_{28}H_{20}N_4O_4$),

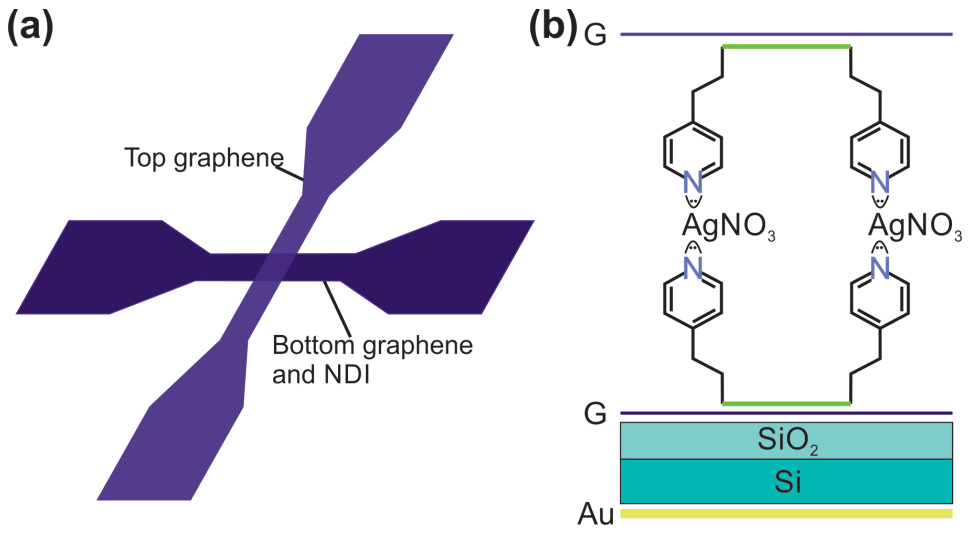

Figure 5.1: Schematic of the multilayer device. (a) Shape of the device and contacts. (b) Cross-sectional view of the complete device (not to scale).

shortened to NDI-Py and shown in Figure 5.2 bound around a layer of silver nitrate ($AgNO_3$). Of the two NDI-Py layers, each is bound to one of the graphene electrodes by van der Waals interactions between the naphthalene diimide cores and the rings in graphene's structure. The bonds around the $AgNO_3$ are co-ordinate bonds between the Ag ions and the N atoms at the ends of the pyridine rings. A cross section of the structure is illustrated in 5.1(b).

The chains attaching the pyridine rings to the NDI cores should be able to rotate around the N-C bonds to the NDI and are approximately 400 pm in length, including the pyridine ring. We designed the structure so that this rotation should continue to make strain sensing possible, while also allowing for negative differential conductance to occur, as in the GSC samples [1, 8, 96].

Our procedure for synthesising the multilayer stack is summarised in Figure 5.3. We synthesised the bottom and top layers separately before combining the two around the $AgNO_3$ near the end of the pro-

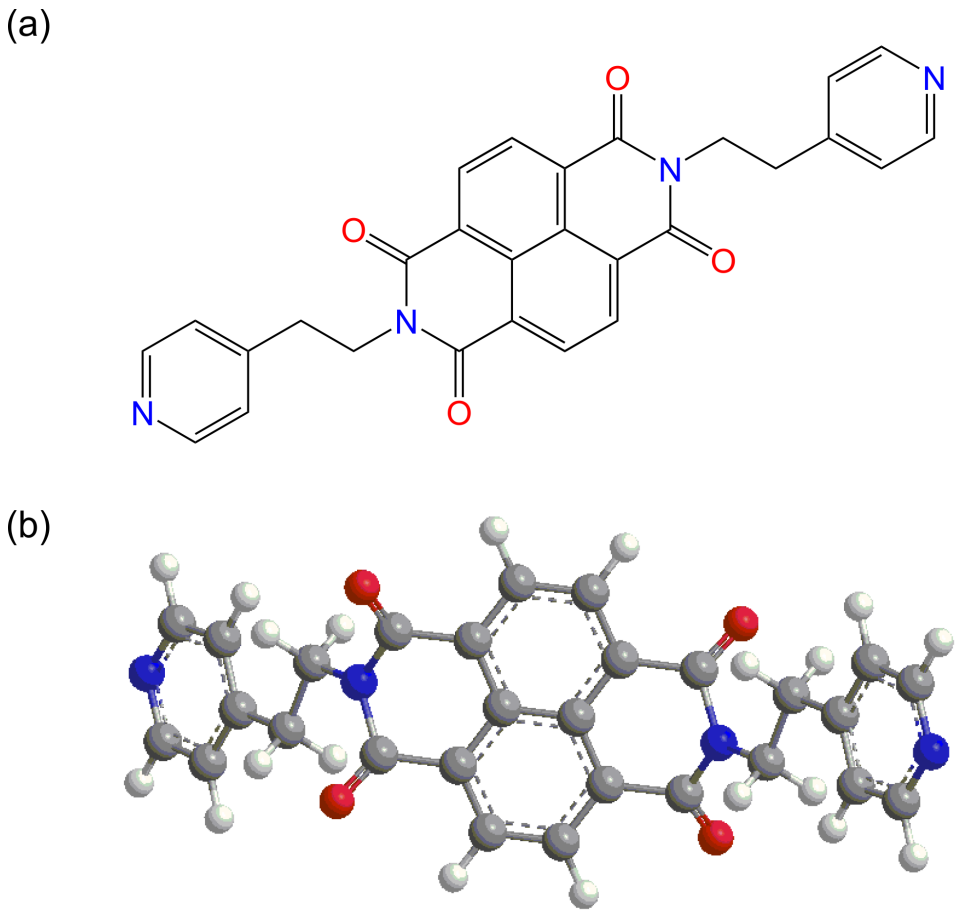

Figure 5.2: a) Chemical structure of the NDI-Py molecule used for the middle layer. The remaining bonds were linked to single hydrogen atoms. b) Three-dimensional representation of NDI-Py.

cess.

The bottom graphene electrodes were more simple to prepare than the top graphene. We bought commercially produced graphene films on SiO_2 in 1 cm^2 square chips from Graphenea. These chips consisted of a 300 nm layer of SiO_2 on top of a thicker, 525 μm layer of Si. The substrate was p-doped with boron and the mobility of the graphene at the charge-neutral point was 3760 $cm^2V^{-1}s^{-1}$ at 4.2 K [106]. Due to the following fabrication steps, the doping level and mobility of the graphene differ in the final devices. Given time, the mobility of the graphene after processing could be measured using the Hall effect. A 100 nm gold backgate was added using an Edwards AUTO 306 thermal evaporator.

The graphene layer was patterned using optical lithography in a MBJ 3 Karl Süss mask aligner with S1813 resist and etched via reactive ion O_2 etching in an Oxford PlasmaPro System 100 Cobra. The mask we used in the optical lithography was designed in KLayout to consist of a pattern within a square, which was then regularly repeated over a grid. The pattern within the square had rotational symmetry, allowing it to be used for both the top and bottom layers, as well as aiding alignment of the two different layers. The pattern used within each square is shown in Figure 5.4, with the measurements shown in μm. Following this, we washed the samples to remove the photoresist, before depositing the NDI-Py by thermal evaporation.

In order to estimate the amount of NDI-Py needed in the crucible during an evaporation, it was necessary to calculate the area of a single adsorbed NDI-Py particle and the surface area the particles expanded to fill during the evaporation. We assume that during the evaporation, the NDI-Py molecules expand evenly through the surface area of a hemisphere after leaving the crucible. Thus, we can obtain the mass M of NDI-Py required in the crucible from

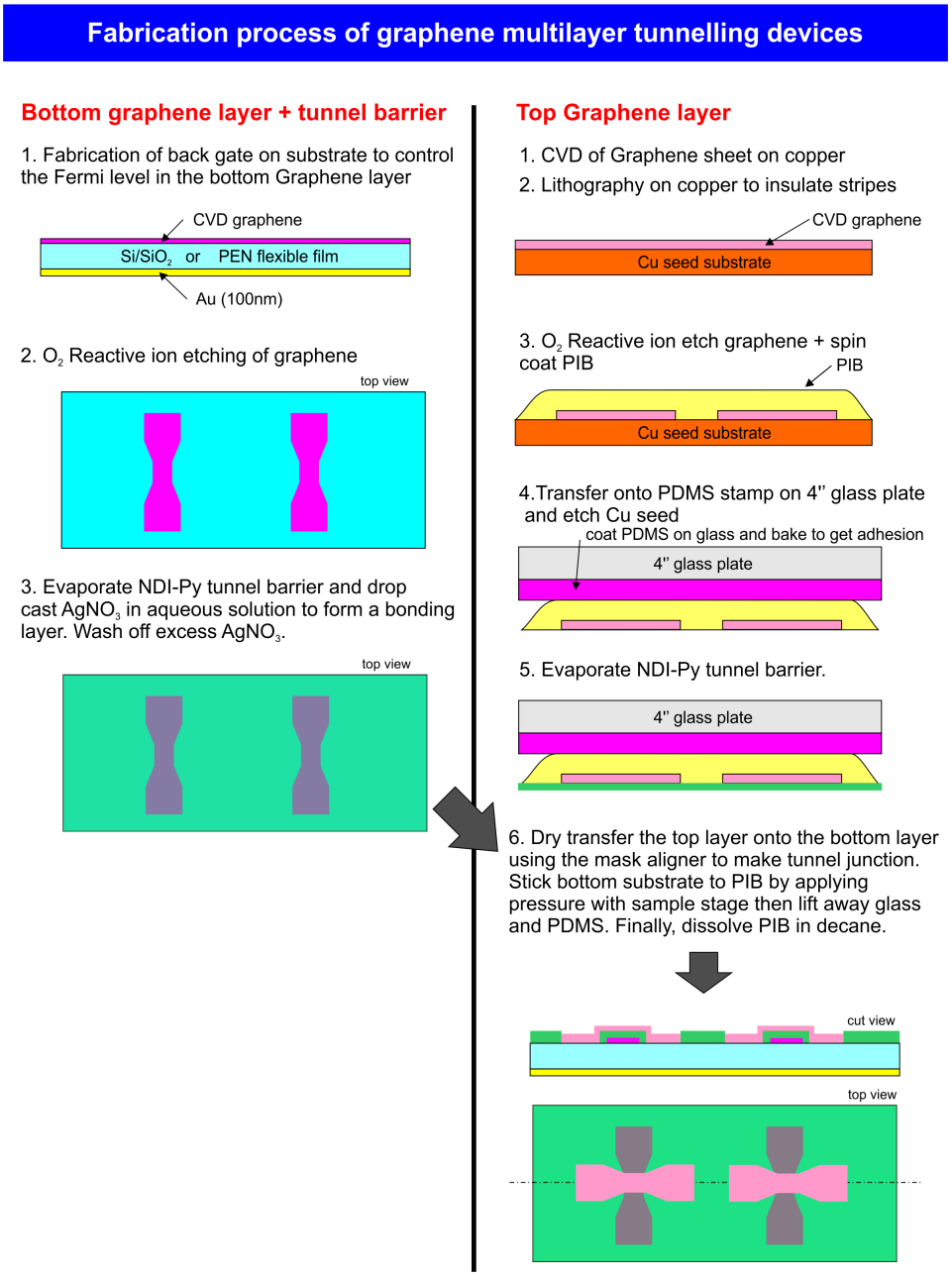

Figure 5.3: Summary of the construction method for multilayer stacks.

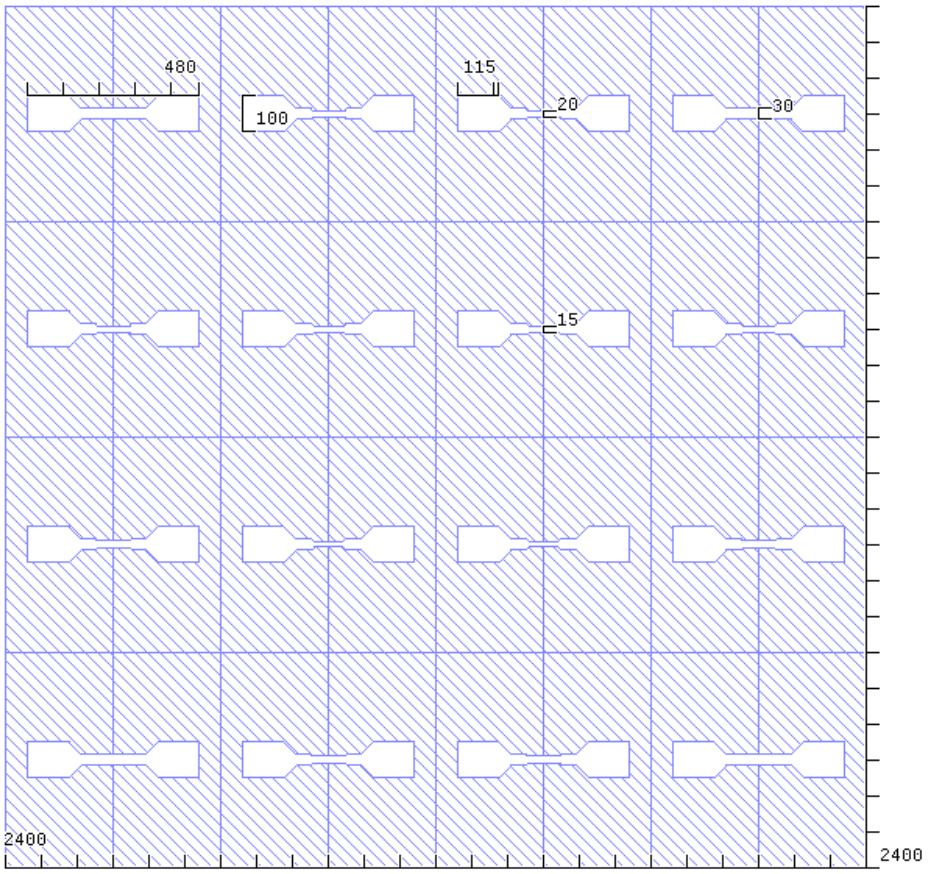

Figure 5.4: View of the mask pattern used in the optical lithography step of sample synthesis. Distance measurements shown are in μm.

$$\frac{A_s}{2\pi r^2} = \frac{m_s}{M}, \tag{5.1}$$

where A_s is the area of the sample(s) to be evaporated on, m_s is the mass of NDI-Py required to cover this area and r is the distance between the crucible and samples. As m_s is likely to vary and M should not be dependent on it with uniform particle distribution, its presence within Equation (5.1) is unhelpful. We can define the number of NDI-Py molecules required to cover A_s as $n \approx A_s/A_m$ where A_m is the area assigned to a single NDI-Py molecule. From simple multiplication to get the mass of n particles we obtain $m_s = nm_m \approx (A_s m_m)/A_m$ where m_m is the molecular mass of NDI-Py. Arranging this in terms of A_s gives:

$$A_s \approx nA_m = \frac{m_s A_m}{m_m}. \tag{5.2}$$

Substituting Equation (5.2) into Equation (5.1) and rearranging we obtain

$$M = 2\pi r^2 m_s \frac{m_m}{m_s A_m} = \frac{2\pi r^2 m_m}{A_m}. \tag{5.3}$$

We can calculate that $m_m = 476$ g mol^{-1} from the atomic structure of NDI-Py (Figure 5.2) and measure $r = 50$ mm for the evaporator used. To obtain values for A_m, we need to look more closely at the structure of NDI-Py.

Using the chemical structure of NDI-Py and the length of atomic bonds within it [107], we can assign an area for each NDI-Py particle to occupy. As the ~ 400 pm carbon-pyridine chains are able to rotate around the N-C bond to the NDI core, we allow for two extremes, depending on how they align on the graphene. In the first case, when the chains are perpendicular to the graphene, we assign a minimum area A_{min} around the area of the core. For the latter case, we assign a maximum area A_{max}, allowing for the chains to rest parallel to the graphene.

As the molecules do not tessellate well, we will assign the area of the smallest rectangle within which a single NDI core can fit to A_{min}. Using the documented lengths of the interatomic bonds [107] and their angles, this rectangle is found to be approximately 6.73 Å by 7.28 Å. This gives $A_{min} = 0.491$ nm^2. To obtain a value for A_{max}, we give a simplified view of the space available to the carbon-pyridine chains by alowing for a circle 400 pm in radius around the nitrogen atoms they are bound to. Calculating the area for two intersecting circles, plus the remaining exposed parts of the core gives $A_{max} = 0.996$ nm^2. While this shape also does not tessellate well, some overlap is required to ensure that bonding can occur between the two NDI-Py layers.

Substituting A_{min} and A_{max} into Equation (5.3) gives a range of between 14 μg and 25 μg to be placed in the crucible. Raman mapping of graphene on a SiO_2 substrate was carried out when using both of these NDI-Py masses placed in the crucible to get a view of the overall surface coverage of NDI-Py after deposition onto samples.

Finally, we drop cast $AgNO_3$ in 0.01 molar aqueous solution on top to bond with the nitrogen atoms in the pyridine rings. After drying, we washed the sample with distilled water to remove excess silver nitrate.

The top graphene started on thin copper films of 1 cm^2, also bought from Graphenea. We carried out optical lithography and reactive ion etching on this graphene similar to the bottom graphene. Following this, in order to enable deterministic transfer of the graphene, it was necessary to transfer it to a polymer stamp. To aid with alignment, we deposited a thin 40 nm layer of SiO_2 onto the copper film in the areas without graphene using an electron-beam evaporator.

This stamp has two different polymer layers and is based on those developed by Bousa *et al* [68] and then refined by both Song *et al*, [65] and Choi *et al* [64]. [51] Our stamps consisted of a 1 mm thick layer of PDMS and a thin layer of polyisobutylene (PIB).

After removing the photoresist, a thin layer of PIB was spin-coated

onto the graphene on copper at 3000 rpm for 30 seconds. The PIB used was dissolved in decane at 30 mg mL^{-1}. [64] We then annealed the film at 100 °C for 8 minutes to remove any excess decane. The PIB-coated side was then brought into conformal contact with the PDMS stamp.

Following this, we etched away the Cu film by floating the stamps, Cu down, in aqueous $FeCl_3$ solution. We then removed the stamps from the solution and cleaned them with deionised water. After the samples dried, we deposited a layer of NDI-Py was using a thermal evaporator, as with the base graphene layers.

We transferred the PDMS/PIB/graphene stamp to a glass slide, then aligned and brought it into contact with the bottom substrate of the sample in the same MBJ 3 Karl Süss mask aligner used in the lithography process. The two parts were left held in contact in the mask aligner for 15 minutes. After this, the PIB layer of the stamp was firmly stuck to the base substrate. We heated the parts to 115 °C for 15 minutes on a hot plate, before slowly peeling the base off. Graphene from the stamp was transferred to the substrate. Similar attempts were made using PMMA in place of PIB for comparison.

After this, we washed off the remaining PIB residue in decane and the samples were ready for testing.

5.1.2 Fabrication of glass samples

To analyse the bonding process between the NDI-Py, $AgNO_3$ and graphene, we synthesised four different sample types on glass substrates. These were classified as follows. Sample type 1 consisted of graphene, NDI-Py and $AgNO_3$ on the glass substrate. Sample type 2 was graphene and NDI-Py on glass. Sample type 3 was NDI-Py and $AgNO_3$ on glass without graphene and sample type 4 was a clean glass substrate acting as a control sample. These samples were produced as shown in Figure 5.6.

For all sample types, the glass used was a thin coverslip. We first

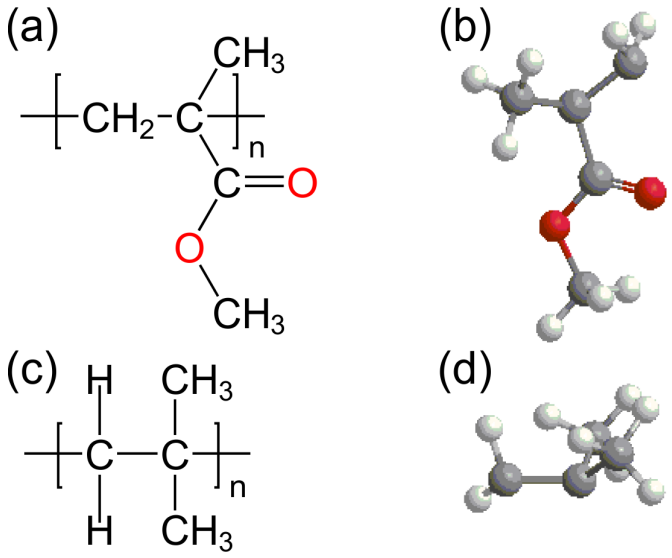

Figure 5.5: Comparison of PMMA and PIB. (a) and (b) the structure of PMMA. (c) and (d) the structure of PIB.

washed the coverslips to ensure that they were chemically clean. Sample types 1 and 2 then had graphene attached using the wet transfer method described in Chapter 2. We used graphene on 1x1 cm Cu foil from Graphenea.

Finally, we thermally evaporated NDI-Py onto all sample types except type 4, followed by the addition of $AgNO_3$ to sample type 1 and sample type 3. These steps were carried out in the same procedure as described in Section 5.1.1

5.1.3 Experimental methods

The first test we performed was Raman mapping of the NDI-Py deposition onto both patterned and non-patterned graphene. Raman spectra of graphene after the deposition were compared to spectra from before the deposition to identify the peaks of the adsorbed NDI-Py molecules. This was done to ensure that the NDI-Py molecules covered the full

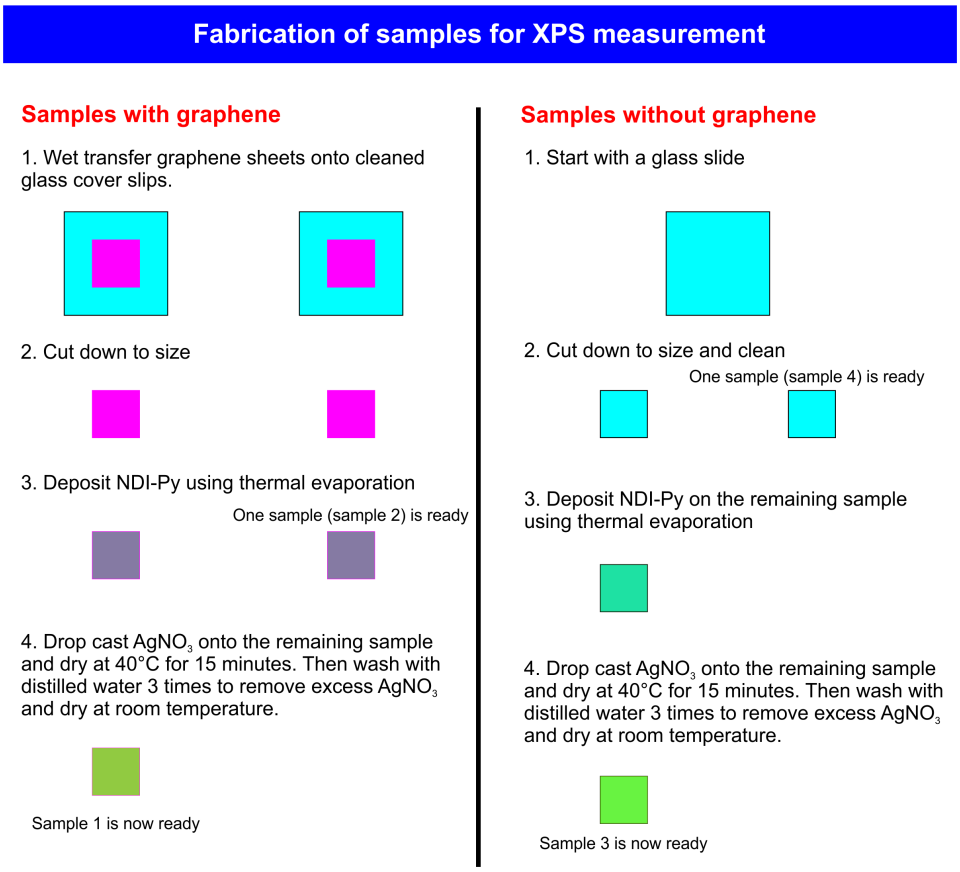

Figure 5.6: Method of construction for glass substrate samples used in adhesion testing and XPS measurements.

area of the graphene.

Following this, we carried out two tests on the glass substrate samples. The first was to determine if the sandwich of NDI-Py and $AgNO_3$ was able to hold together. This was done by attempting to stick together matching pairs of samples of each of the four types shown in Figure 5.6. We placed the samples together after washing them in distilled water and allowed to them dry. This was done to aid the initial adhesion using the water's surface tension while NDI-Py and $AgNO_3$ bonded. After 24 hours, we tested the adhesion within sample pairs against gravity and shear forces caused by tapping the edge of samples.

The second test on glass substrate samples was X-ray photoelectron spectroscopy (XPS), carried out at the University of Bristol. These measurements allowed for comparison of the amounts of different elements present. From this, the success rate of the bonding between NDI-Py and $AgNO_3$ could be inferred, along with the efficiency of the construction method. XPS was chosen as initial tests showed that there were insufficient amounts of NDI-Py to be detected by optical or infra-red spectroscopy. This test was carried out on sample types 1 to 4.

Due to the XPS measurements being more sensitive to certain electrons than others, along with some differences in measuring individual peaks, it was necessary to normalise the results in order to obtain the number of atoms of each element present n_a. This was done through the equation

$$n_a = A_N = \frac{A_p}{\Delta t \, n_s \, S}, \tag{5.4}$$

where A_N is a normalised area, A_p is the area under the peak plotted (relative to the curve background), Δt is the duration of time spent measuring each step, n_s is the number of scans carried out and S is the sensitivity factor for the peak. The values of S for the relevant elements are shown in Table 5.1. The ratios between elements could

Element	Transition	S
Carbon	1s	0.00161816
Nitrogen	1s	0.00290818
Oxygen	1s	0.00473956
Silicon	2p	0.0011035
Silver	3d	0.0255278

Table 5.1: Sensitivity factors of different element transition peaks.

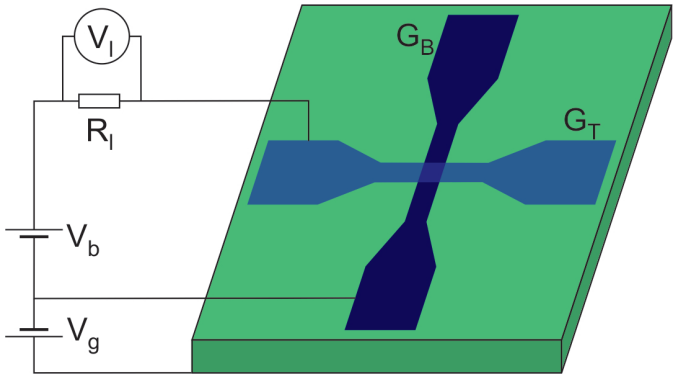

Figure 5.7: Connections and circuit for measuring the IV curves of multilayer samples.

then be compared using the ratios between n_a for each element.

We measured IV curves of complete samples on SiO_2 using a LabVIEW program connected to a Keithley 2400 sourcemeter and a Keithley 2000 multimeter. Connections to the device were made using an Alessi REL-4100A probe station to place conducting tips onto the contact pads on the device. The sourcemeter supplied power, while the multimeter measured the voltage across a known resistor in series with the sample, allowing for the current through the circuit to be calculated. The circuit used is shown in Figure 5.7. Measurements at 77 K were carried out by resting the sample on a metal block, which was surrounded by liquid nitrogen contained in polystyrene.

5.2 Multilayer characterisation

5.2.1 Raman spectroscopy of NDI-Py deposition

Figure 5.8 shows the Raman spectrum of the base graphene electrode on SiO_2. The main visible peaks are labelled. G corresponds to the G peak, a doubly degenerate E_{2g} vibrational mode in-plane with the graphene at 1580 cm^{-1} [108]. A D peak, labelled D, is also observed at 1350 cm^{-1}. This peak is caused by fundamental zone-boundary phonons, and is only present when there are inelastic scattering and elastic recombination due to defects within the graphene. A peak due to second-order phonons, known as the 2D peak, are observed both with and without defects near 2700 cm^{-1}. [108] This is indicated on the graph with a $2D$ label. The G and 2D peaks are useful for detecting graphene as the G peak is generally 3-5 cm^{-1} higher in graphene compared to graphite, while the 2D peak is sharper and more intense than graphite. The 2D peak also shifts its position towards higher Raman shift values with a greater number of layers. [108]

Averages of the Raman spectra for several readings over bottom layer samples are shown in Figure 5.9. Observing the black line, representing NDI-Py on graphene on SiO_2, shows that the G peak is seen at 1590 cm^{-1}. This is shifted slightly from the normal position of 1580 cm^{-1} due to some doping and defects caused by the wet transfer process. [18,109] The G and D peaks are indicated on Figure 5.9 with a G and D respectively. Some further contaminant traces, labelled as C, are seen at both 1555 and 1604 cm^{-1}, and are present separate from the graphene, as seen by the red curve of NDI-Py on SiO_2. These are not present in Figure 5.10, which plots the Raman spectra of non-patterned graphene samples on SiO_2 with and without the deposition. This supports the theory that they are not caused by the presence of NDI-Py itself.

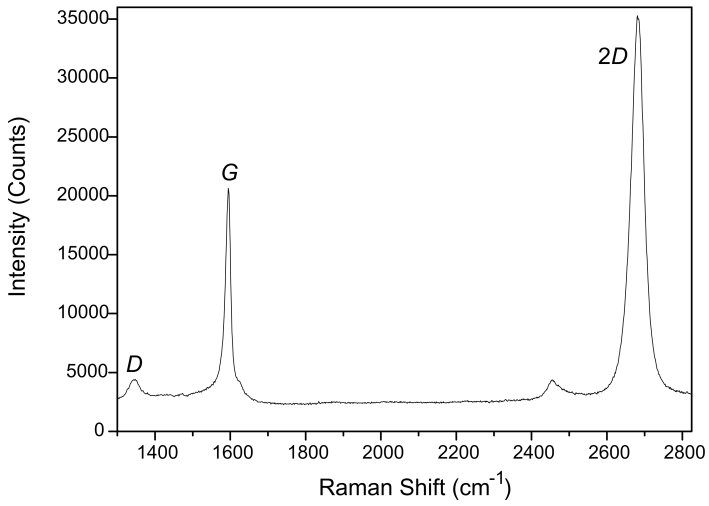

Figure 5.8: Raman spectrum of the base grapehen layer before sample fabrication, with the G, D and 2D peaks marked.

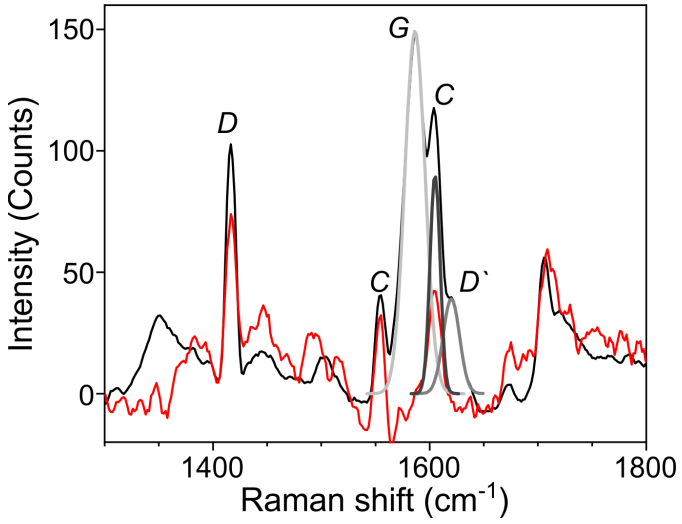

Figure 5.9: Average Raman spectra over several points of a NDI-Py on patterned graphene and SiO_2 sample. Red line: Points without graphene. Black line: Points with graphene. Grey lines: Deconvoluted peaks for the G (light grey), D' (grey) and contaminant (dark grey) modes.

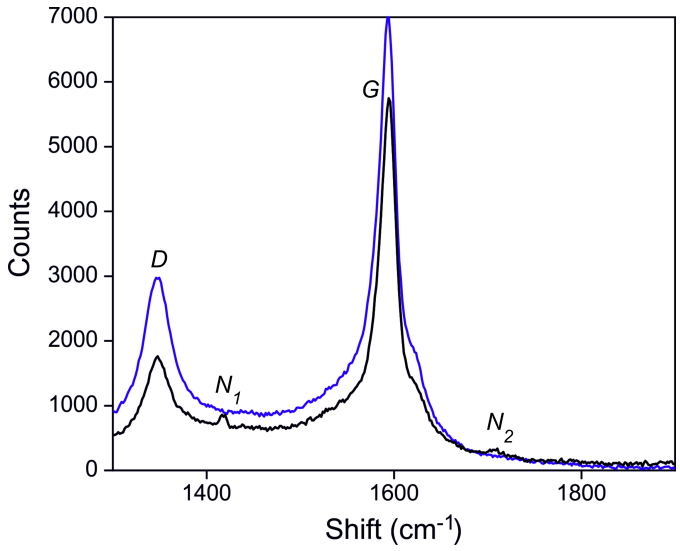

Figure 5.10: Average Raman spectra over several points of samples with and without NDI-Py on graphene on SiO_2. Blue line: Points without NDI-Py. Black line: Points with NDI-Py.

The peaks seen at approximately 1417 and 1707 cm^{-1}, labelled N_1 and N_2 respectively, appear to be Raman modes caused by the presence of NDI-Py, as they are not present in samples before NDI-Py deposition and occur over area both with and without graphene, as well as on samples without graphene patterning steps. The evidence of these peaks occurring across the entire sample is supported by the Raman maps in Figure 5.11. In Figure 5.11, Raman maps of one end of a bottom layer bar are shown for both 2681 cm^{-1} in part (a) and 1417 cm^{-1} in part (b). Figure 5.11(a) maps the presence of graphene using the 2D peak and shows the shape of both the contact pad and the beginning of the narrow bar. In Figure 5.11(b) mapping the presence of NDI-Py however, very little of the pattern is visible, apart from the top left corner of the contact pad. At this scale, the NDI-Py appears to give full coverage of the sample. This implies that while there may be slightly more NDI-Py adhering to graphene due to the

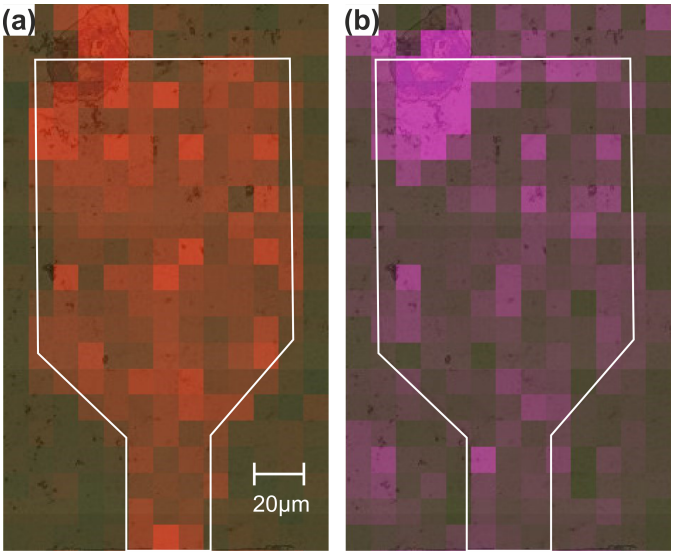

Figure 5.11: Raman maps of a NDI-Py deposition at one end of a patterned graphene base layer carried out at (a) 2D peak of graphene at 2681 cm^{-1} and (b) a small peak indicating NDI-Py at 1417 cm^{-1}.

similar hexagonal structures aiding in the van der Waals bonding, this effect is not sufficient to disrupt the deposition of a thin NDI-Py layer.

5.2.2 X-ray photoelectron spectroscopy of NDI-Py and $AgNO_3$ depositions

The survey results of all 4 sample types up to a binding energy of 1200eV are shown in Figure 5.12. This provides a quick initial look at the elements present within each sample before closer results zoomed in on individual atomic peaks were collected. Useful data can also be collected from the survey results.

A common feature in all measured samples is the presence of large amounts of carbon, oxygen and silicon. There are two reasons for these large values. The first is that all three elements are much more numerous than the silver and nitrogen in the deposited molecules. Oxygen

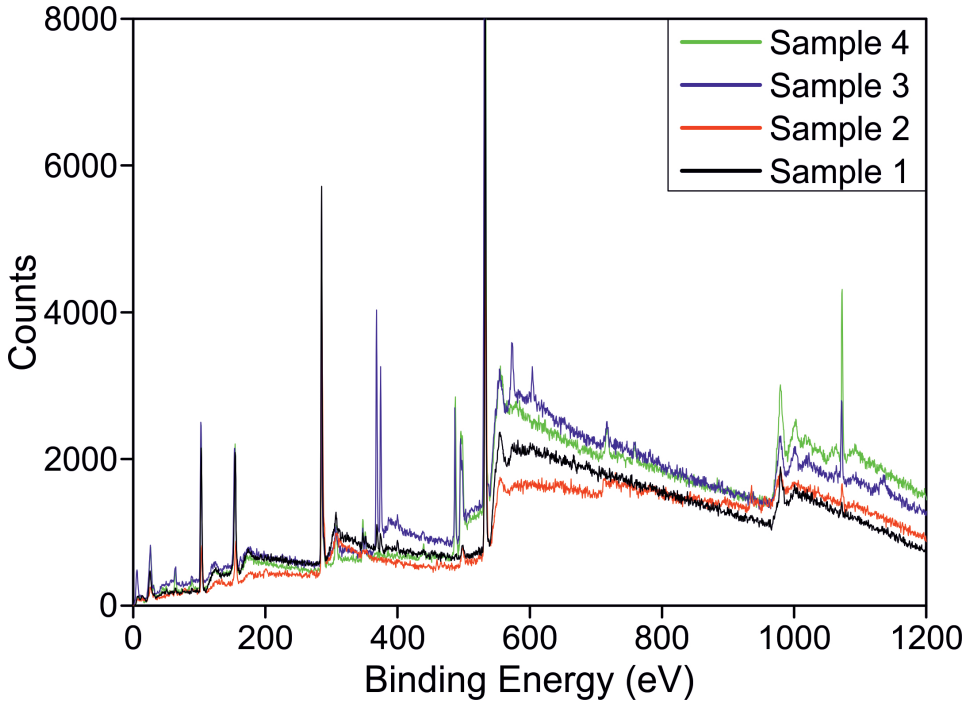

Figure 5.12: XPS survey results for all 4 sample types. Pass energy used = 50eV. Step size = 0.5eV. $dt = 0.25$s.

and silicon make up the majority of the silica glass substrates, with further oxygen being present in both the silver nitrate and NDI-Py. The samples with graphene have comparatively large amounts of carbon due to this. Further, the NDI-Py molecules consist mostly of carbon and hydrogen atoms. The second reason is that the XPS process overestimates the presence of both carbon and oxygen atoms, in part due to being unable to clean the samples as the cleaning process would damage or remove the NDI-Py molecules. The number of silicon atoms detected is likely underestimated for all sample types except type 4 due to the decreasing sensitivity of XPS for layers deeper within a sample. Despite this, we see the quantitative shift in the numbers of carbon and oxygen atoms relative to each other expected from the materials present in each sample.

The next point of interest is that the majority of the contaminant peaks such as sodium, calcium, aluminium and tin are shown to be part of the glass substrate (sample 4). These are also visible in other sample types, most notably sample type 3, but become harder to see as more layers of material are placed on top of the glass. The visibility of these impurities gives evidence for the deposition of NDI-Py being a thin layer. Contaminants of copper, iron and chlorine can be seen in sample type 2. These are due to the wet transfer of graphene from Cu to the glass substrate. Interestingly, these are less visible in sample type 1 where $AgNO_3$ has been added in aqueous solution. This is most likely caused by the extra layer obscuring the small number of these dopant atoms. Due to the lack of other contaminant materials, it can be seen that the depositions of NDI-Py and $AgNO_3$ are clean processes without introducing other materials to the multilayer stack.

More detailed scans of the N1s and Ag3d peaks are shown in Figure 5.13. Only the data for samples where these elements were present are shown. The graphs allow for a visual comparison between different samples of the numbers of atoms detected. Notably, the sample with-

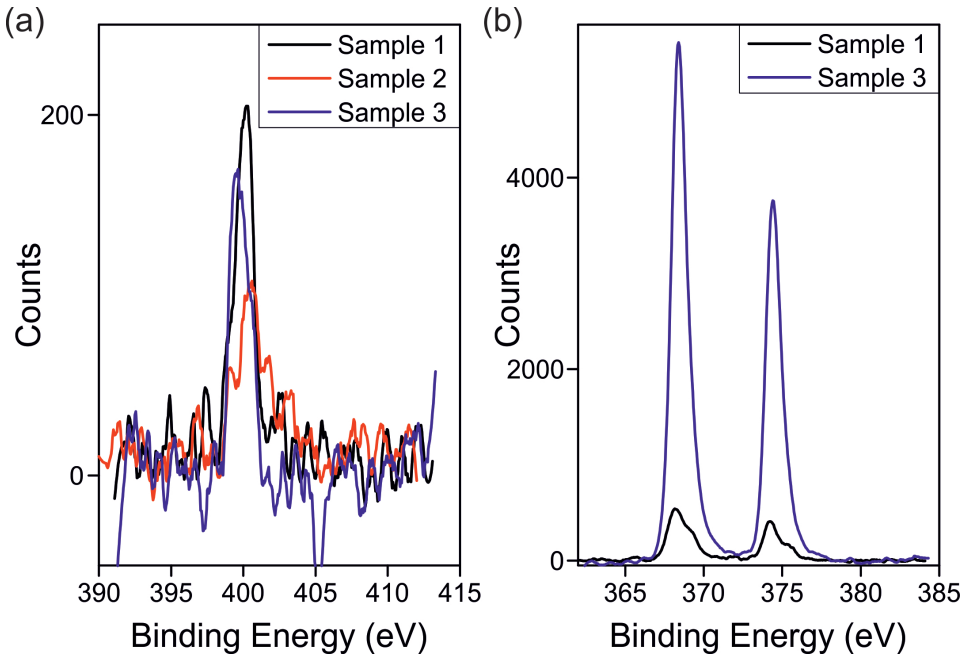

Figure 5.13: Focussed XPS scans over (a) the nitrogen 1s peak, and (b) the silver 3d peaks for samples where these elements were present. The baseline has been subtracted. Pass energy used = 20 eV. Step size = 0.05 eV. $dt = 0.5$ s.

out $AgNO_3$, of type 2, had the lowest N count. This makes sense as it is missing one source of nitrogen atoms. Sample 1 has a higher N count and a much lower Ag count when compares to sample 3. This implies that more successful bonding between $AgNO_3$ and NDI-Py has occurred in sample 1, with more $AgNO_3$ degrading to atomic silver in sample 3.

Using data from the curves in Figure 5.13 as well as curves for the C1s and O1s peaks, data was processed according to Equation (5.4) to obtain the ratios of atoms for the elements present. These findings are shown in Table 5.2. Using Equation (5.4) on data from Figure 5.13 shows that the number of nitrogen atoms present in sample type 1 is 1.51 times more than in sample type 2. In the case of perfect bonding

Sample	Correction	C:O	C:N	C:Ag	N:Ag
Type 1	None	1:1	73:1	127:1	2:1
	Removal of background C	1:1	50:1	91:1	2:1
Type 2	None	2:1	105:1	N/A	N/A
	Removal of background C	1:1	71:1	N/A	N/A
Type 3	None	1:2	44:1	10:1	1:4
	Removal of background C	1:3	22:1	5:1	1:4

Table 5.2: Ratios of elements detected in XPS for sample types 1, 2 and 3.

between $AgNO_3$ and NDI-Py, this ratio should be 1.50 as each NDI-Py molecule contains 4 N atoms and bonds to two $AgNO_3$ molecules, adding 2 more N atoms per NDI-Py present. This implies that the bonding process occurs nearly perfectly. However, a closer inspection of Table 5.2 shows that the ratio of N to Ag within sample 1 is approximately 2:1. This indicates a higher level of silver than expected in the perfect case (ratio 3:1). Considering that this ratio for sample 3 is 1:4, it can be determined that this is due to the formation of atomic silver on the surface of the sample via photochemical decomposition. If the silver remained bonded to its nitrate counterpart, it would be impossible for more silver to be present than nitrogen. Due to this, the most likely cause of the excess silver is $AgNO_3$ degrading to atomic Ag with the rest being washed away. The results indicate that the presence of graphene vastly reduces the formation of this atomic Ag. As the atomic structure of graphene is similar to that of the NDI core while glass is irregular, the NDI-Py molecules should adsorb in a more regular pattern on sample 1. The NDI-Py molecules are more likely to clump together in samples of type 3. Due to this, $AgNO_3$ has fewer NDI-Py molecules available to bond with and more space available to potentially settle and form atomic Ag. The formation of atomic Ag is

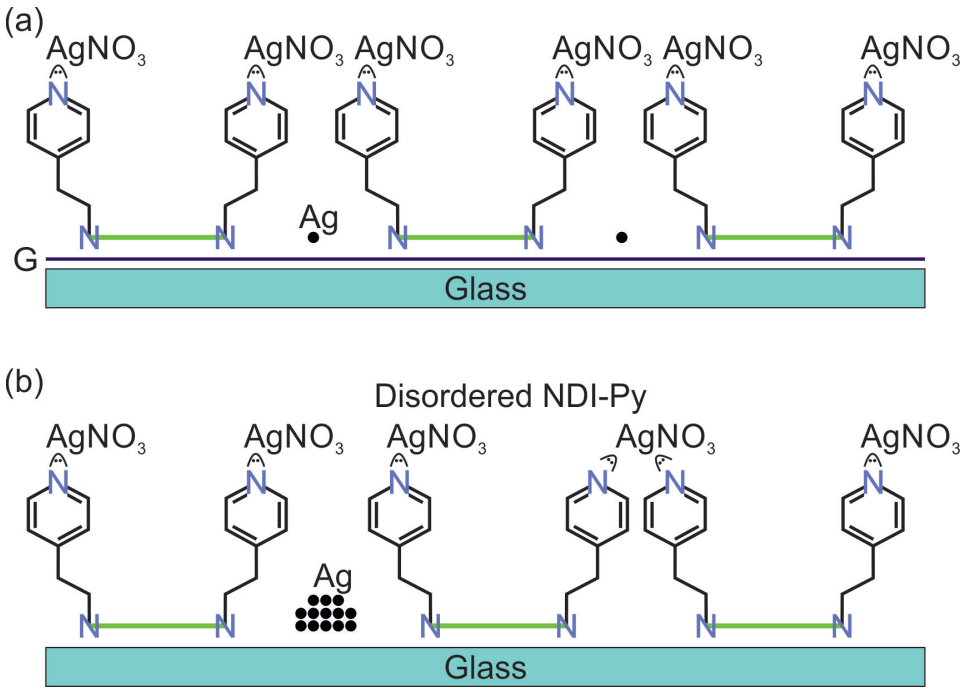

Figure 5.14: Cross section of a small are of (a) sample type 1, and (b) sample type 3. The disordered spacing of NDI-Py in the absence of graphene affects bonding to $AgNO_3$ and allows for the formation of larger amounts of atomic Ag.

likely to occur in gaps in the NDI-Py adsorption pattern, where the absence of N atoms to bond with allows Ag atoms to settle on the exposed graphene or glass surface. Possible examples of this are shown in Figure 5.14.

Qualitatively, the change in the ratio of carbon to nitrogen atoms between the samples in Table 5.2 fits with what is expected. Type 2 has the highest ratio of carbon to nitrogen due to the absence of $AgNO_3$. Type 3 has the lowest as there is no graphene. However, due to XPS overestimating the quantities of carbon and oxygen present, quantitative findings can not be deduced from this.

5.2.3 Patterned graphene transfer method results

Micrographs of different stages of sample production are shown in Figure 5.15. These are used to help demonstrate the findings in the following subsections.

Adhesion to polymer

The graphene was found to stick to the PIB stamps far more efficiently than the PMMA stamps. This can be seen by comparing parts (b), (c) and (d) in Figure 5.15. Several areas were seen to be missing on the PMMA stamps and there was considerably more visible damage as shown in Figure 5.15(c) and (d). Examining literature on the subject shows that this was caused by the PMMA reacting with the $FeCl_3$ etching solution and applying large strains to the graphene. [65]

Additionally, the PMMA did not detach well from the PDMS stamps. This, combined with the reason above leads to the conclusion that PIB is the superior polymer for this graphene transfer method, while PMMA is unusable.

Further, wet etching of the initial copper substrate was found to be inefficient when already attached to a glass slide, thus also reducing the yield of usable graphene. This was due to physical limitations of the system. Etching the Cu with the samples fully submerged and facing upwards caused the graphene to be lifted away with the etched Cu. Etching the Cu substrate by holding the glass slide so that the Cu was just submerged into the solution was unreliable and impractical to keep steady. The solid glass slide also limited the flexibility of the samples during etching. These issues were not observed in floating stamps.

Checking the resistance of the graphene at this stage showed it to be in the kΩ range when using a PIB on PDMS stamp.

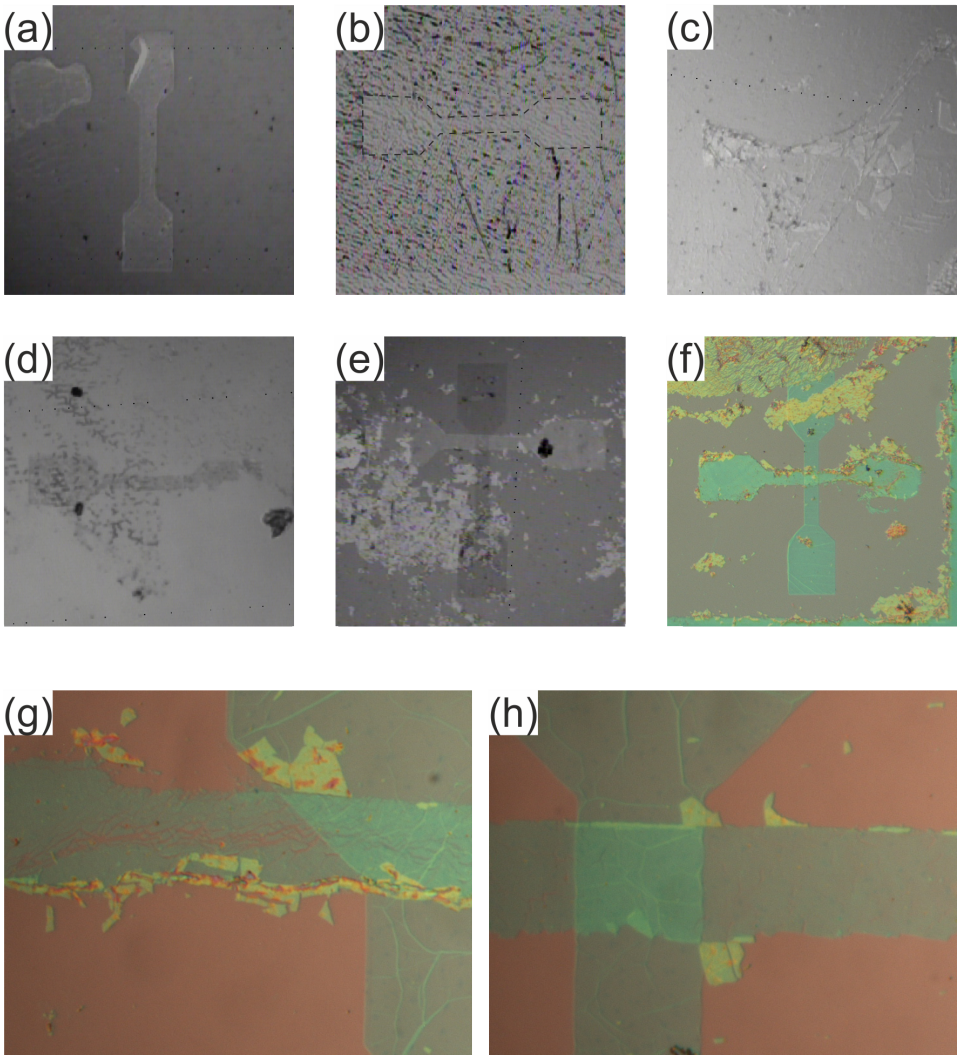

Figure 5.15: Micrographs of the sample at different points in development: (a) the base graphene layer on SiO_2 and (b) the top graphene layer on the polymer stamp with NDI-Py before combining the two layers; (c) and (d) the damaged top layer on a PMMA stamp; (e) the transfer quality when using PIB as the release layer and a thin PDMS layer; (f) improved alignment using a thicker PDMS layer; (g) a transfer with a cracked top layer; (h) a successful transfer.

SiO_2 base

No graphene was successfully transferred to the SiO_2 base when using a PMMA and PDMS stamp. Transfer quality from PIB on PDMS stamps varied according to a number of factors.

The first of these was the time the stamp was pressed against the base for within the mask aligner. The amount of graphene and PIB transferred to the base from the PDMS increased as this time increased. This was however a small effect and beyond 15 minutes, no appreciable difference in transfer yield was observed.

The second factor was the heating of the stamp while in contact with the base substrate. Contrary to previous research [65, 66], heating the stamp was found to reduce the yield of transferred graphene. During heating, the PIB layer began to detach from the SiO_2 base. The exact reason for this is unknown, but it is likely due to either the fact that this transfer was to rigid SiO_2 instead of a flexible substrate or that no device was available to heat the stamp while it was still in the mask aligner, causing the PIB to begin detaching due to lack of pressure. An attempt to prevent the latter was made by applying weights to the stamp on SiO_2 while heating it, but did not solve the issue.

The third factor was the thickness of the PDMS layer in the stamp. Thinner PDMS stamps allowed for the PIB layer to shift and twist more during the stamping process. This caused the top graphene layer to break, bend and/or be misaligned as in Figure 5.15(e), where a 0.5 mm PDMS layer was used. Due to the greater compression and flexibility allowed by a thicker PDMS layer, these effects could be reduced. Figure 5.15(f) shows improved alignment when using a 1 mm layer of PDMS compared to part (e). This effect could be reduced further by increasing the PDMS layer beyond 1 mm, but could not be achieved using this mask aligner as it reduced the graphene visibility and would not fit between the glass mask and sample stage. Using a

thicker PDMS layer also helped reduce, although not remove entirely, the amount of cracks and discontinuities in the transferred top layer graphene. The presence of these discontinuities in PIB-based stamping has been reported before by Bousa *et al.* [68] Figure 5.15(g) shows a cracked graphene layer from the strains of transfer compared with an intact layer in Figure 5.15(h). Due to the discontinuities, the sample in part (g) is non-conducting.

As mentioned in Section 5.1.1, future characterisation of the graphene sheets in completed devices is required, including Hall measurements to determine the mobility, atomic force microscopy to analyse defects and spectroscopy to determine dopants.

5.2.4 IV curves of complete devices at 300 K and 77 K

Figure 5.16 compares the IV curve across a sample with 30x30 μm overlap between the top and bottom graphene with that of a control sample consisting only of the top and bottom graphene electrodes brought together using the same stamping process. Both samples are observed to have similar shapes, with the current I displaying an exponential dependence on the bias voltage V_s applied across the sample. However, the current observed across the control sample is six times higher. This suggests the presence of a tunnelling barrier in both samples, with that of the complete sample providing a significantly larger resistance. This is due to the increased separation between the two graphene electrodes created by the presence of the NDI-Py and $AgNO_3$ in the completed sample.

A room temperature measurement (~300 K) is shown in Figure 5.17 alongside a lower temperature (~77 K) IV curve. Both curves are taken across a sample where the crossed area between the two graphene layers is 30x30 μm. Somewhat unexpectedly, the current is observed to be higher for the same voltage at lower temperatures. This

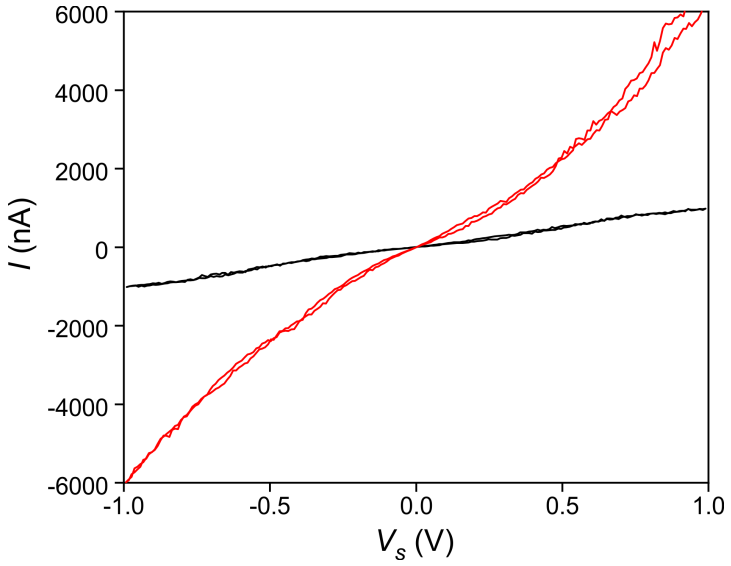

Figure 5.16: Room temperature IV curve for a 30x30 μm cross (black line) compared to that of a a control sample prepared without depositions of NDI-Py and $AgNO_3$ (red line).

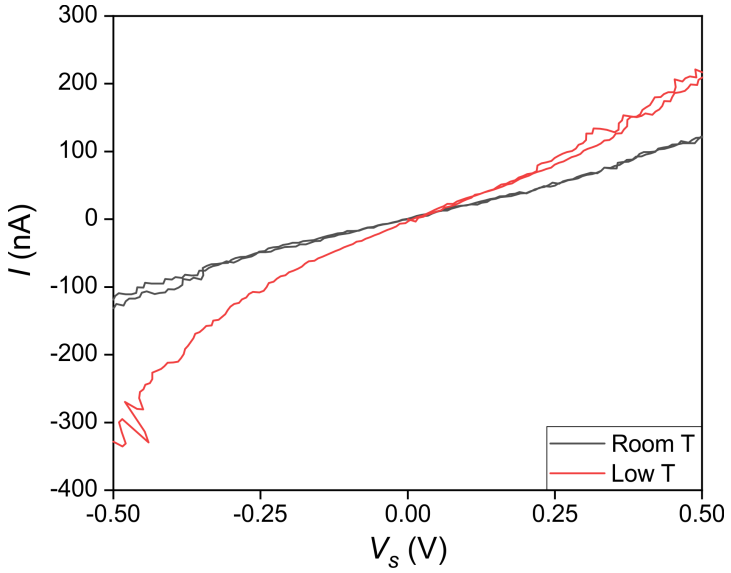

Figure 5.17: IV curve at 77 K for a 30x30 μm cross compared to a room temperature IV curve for the same cross.

decreased resistance could be due the lower temperatures resulting in pyridine moieties of the NDI-Py molecules which are angled away from the plane of the graphene rotating around the N-C bond with the NDI core and flattening back down to be in plane with the graphene layers. This effect would result in a reduction of the tunnelling barrier width, decreasing the resistance of the sample. This appears to be a gradual effect, as measurements taken as the sample is cooled by liquid nitrogen or soon after have higher resistances than the room temperature measurements, as would be expected from the higher energy $1/2k_BT$ of the charge carriers. A multi-value region appears in the curve for 77 K measurements near its most negative values. This is unlikely to be physical, but instead due to ice and vibrations affecting the connections between the probe station tips and the graphene, preventing accurate measurements from being acquired.

IV curves taken across two different cross samples at room temperature are shown in Figure 5.18 along with a curve of the intermediate voltage range in Simmons' approximation fitted to each sample. [72] The two different areas used are 15x15 μm and 30x30 μm. If the tunnelling barrier height and width remained the same across both samples, then the expected current across the 30x30 μm cross would be 4 times higher than across the 15x15 μm cross due to the relation between area and resistance. This is not the case however.

The value used for effective mass in this model is one electron mass. The approximation was fitted to the positive side of each curve as the positive data was collected first. The best fits when using an effective mass equal to the rest mass of an electron were found to use $s = 1.0$ nm and $\phi = 5.9$ eV for the 30x30 μm and $s = 0.97$ nm and $\phi = 5.9$ eV for the 15x15 μm. This suggests the possibility that the current across the 15x15 μm cross is higher than expected compared to the 30x30 μm cross due to a shrinking of the barrier width as area decreases. This effect could be caused by rotation of the NDI-Py moieties, with the

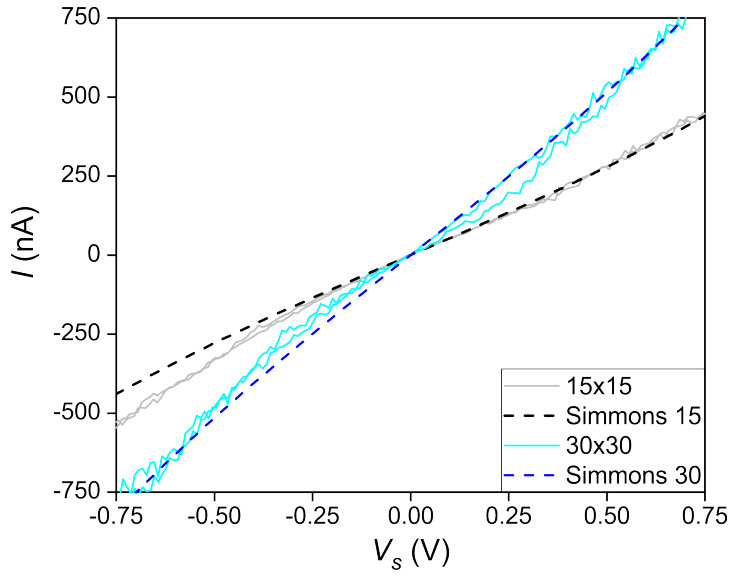

Figure 5.18: Room temperature IV curves for both a 30x30 μm and a 15x15 μm cross sample, along with fits to Simmons' intermediate voltage range approximation for a rectangular tunnelling barrier.

chains being flatter in the 15x15 μm cross. Using Simmons' equation for low voltage measurements on a 30x30 μm cross also gives the best fit with $s = 1.0$ nm and $\phi = 5.9$ eV for samples with an effective mass of $1m_e$ This indicates good agreement and that parameters remain consistent in different regions.

Potential Coulomb blockade

Preliminary analysis of the IV curve of samples at 77 K with a lower bias voltage (<60 mV) shows another feature that may be present in these devices. This can be seen in Figure 5.19, which plots the current with increasing bias on one axis, and the conductivity G calculated from I on the other. I appears to form a staircase shape as V changes, with 4 vertical steps and 5 plateaus, although 3 are shifting somewhat, before continuing on with a different pattern. This pattern is traced

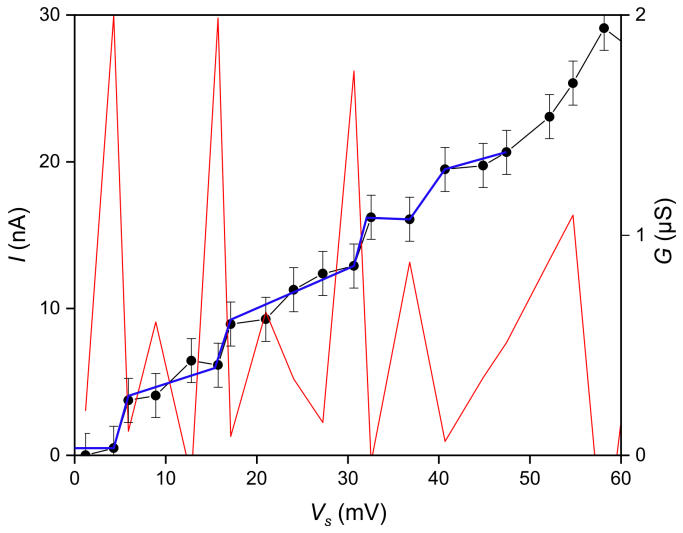

Figure 5.19: (Black line) 77 K and low voltage results from a 30x30 μm cross sample. (Blue) Trace to guide the eye on the possible Coulomb staircase. (Red) Conductivity calculated from the change in the IV curve.

out with the blue line to act as a guide for the eye. The value of G can be seen to spike at each of the vertical steps in I. This effect is largest for the first three steps and matches well with the expected values for the differential of the current in a Coulomb staircase.

A potential cause of this effect is Coulomb charging across the Ag atoms around which the pyridine rings in NDI-Py are bonded. Due to the presence of multiple (likely millions) quantum dots formed by the large number of separated silver atoms, these effects may be blurred and multiplied by the differing and similar conditions for the various quantum dots. A second possible cause is tunnelling beginning to occur at different points in the cross-section of the device, starting with quantum dots that have the lowest resistances. [110] However, due to the small area of the adsorbed NDI-Py molecules (~1 nm^2) and the normal size of quantum dots (~10 nm) [110–112] relative to the area of the sample (900 μm^2) and a step number as low as five,

this seems unlikely. Cooling samples to a temperature below that of liquid nitrogen should give a more detailed analysis of these features and show smaller step sizes due to the reduced effect of high energy electrons.

In order for the Coulomb staircase to be visible on the IV curve, the charging energy across the device $E_C = e^2/(2C_T)$ must be larger than the thermal energy $1/2k_BT$, where C_T is the total capacitance of the double tunnelling barrier, k_B is the Boltzmann constant and T is the temperature. If this is not the case, then electrons can pass through the barriers by thermal excitation. As E_C becomes larger compared to the thermal energy, the steps in the Coulomb staircase become more well-defined. [113] Due to this, no Coulomb staircase is observed in low voltage measurements of these samples carried out at room temperature. The thermal energy is calculated to be 3.3 meV at 77 K and 13 meV at 300 K. Using measurements taken from the step sizes across low temperature samples gives a value of $E_C \approx 5$ meV. The discreet appearance of the IV curve at this level is observed in less than half of samples, although with similar apparent step sizes when comparing samples. Further measurements at lower temperatures to reduce the effects of thermal energy and improve visibility should be carried out to confirm or deny the presence of a Coulomb staircase. An estimate of a possible Coulomb staircase, if real, based on the observed E_C values is shown in Figure 5.20. However, due to the number of currently unknown parameters for NDI-Py and the devices, this estimate is unlikely to be accurate.

The energy levels across the sample under these conditions are looked at in Figure 5.21. For simplicity, the effects of doping on the top layer are assumed to be negligible in this Figure and will be discussed later. At bias voltages close to zero, shown in Figure 5.21(a), the chemical potentials of the two graphene electrodes are close together across the tunnelling barriers and there are no free energy levels between them

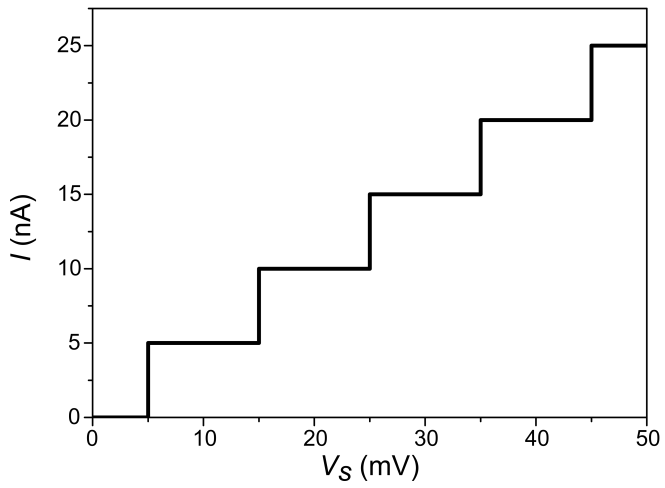

Figure 5.20: An estimate of what the Coulomb staircase could be under ideal conditions.

in the Ag^+ ion. Due to this, electrons carrying charge are required to tunnel over a larger distance in a single hopping event. This results in a low tunnelling current at voltages close to zero. In reality, there will also be energy levels within the the NDI-Py molecules. Due to a lack of research on NDI-Py, the exact values of these energy levels are unknown, but it is possible that tunnelling may also occur through these energy levels. This would further decrease the tunnelling barrier widths and decrease the visibility of any potential Coulomb staircase.

As V_s increases (Figure 5.21(b)), the chemical potential difference between the two graphene electrodes also increases. This results in electron energy levels in the silver ion being placed between them. This allows for electrons to tunnel first to the Ag^+ ion, then to the second graphene electrode in two events with a much higher tunnelling probability. The number of electrons that can do this is limited by the number of available energy levels and Pauli exclusion. Only two electrons, one spin up and one spin down, can occupy each energy level at the same time. The steps in Figure 5.19 correspond to these energy

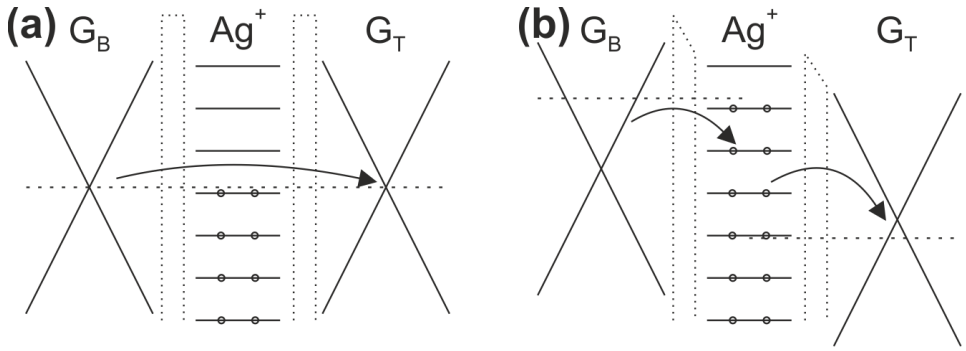

Figure 5.21: Energy level diagram across the height of the sample at (a) low bias voltage and (b) high bias voltage. Regions contained within the dotted lines are the tunnelling barriers and the dashed lines represent the Fermi energies of the graphene electrodes. Arrows indicate the tunelling of electrons.

levels becoming available. As the tunnelling junction uses a Ag^+ ion, the 5s electron orbital starts empty and all new energy levels opened up allow for two additional electrons to tunnel across the sample at once, providing an explanation for why the steps in Figure 5.19 are approximately the same size.

In reality, due to doping and the large number of QDs across the sample area, there are still a few positions on the sample where electrons can tunnel to Ag ions. The variation in QD parameters also results in the step size variations and slopes between steps seen in Figure 5.19.

Varying gate voltage

The effects on the high voltage IV and RV curves of varying the gate voltage V_g are displayed in Figure 5.22. A pattern is demonstrated where the resistance of the sample increases as V_g becomes more negative, and decreases when V_g is positive. This pattern is also present in a control sample without the presence of NDI-Py or $AgNO_3$, as shown in

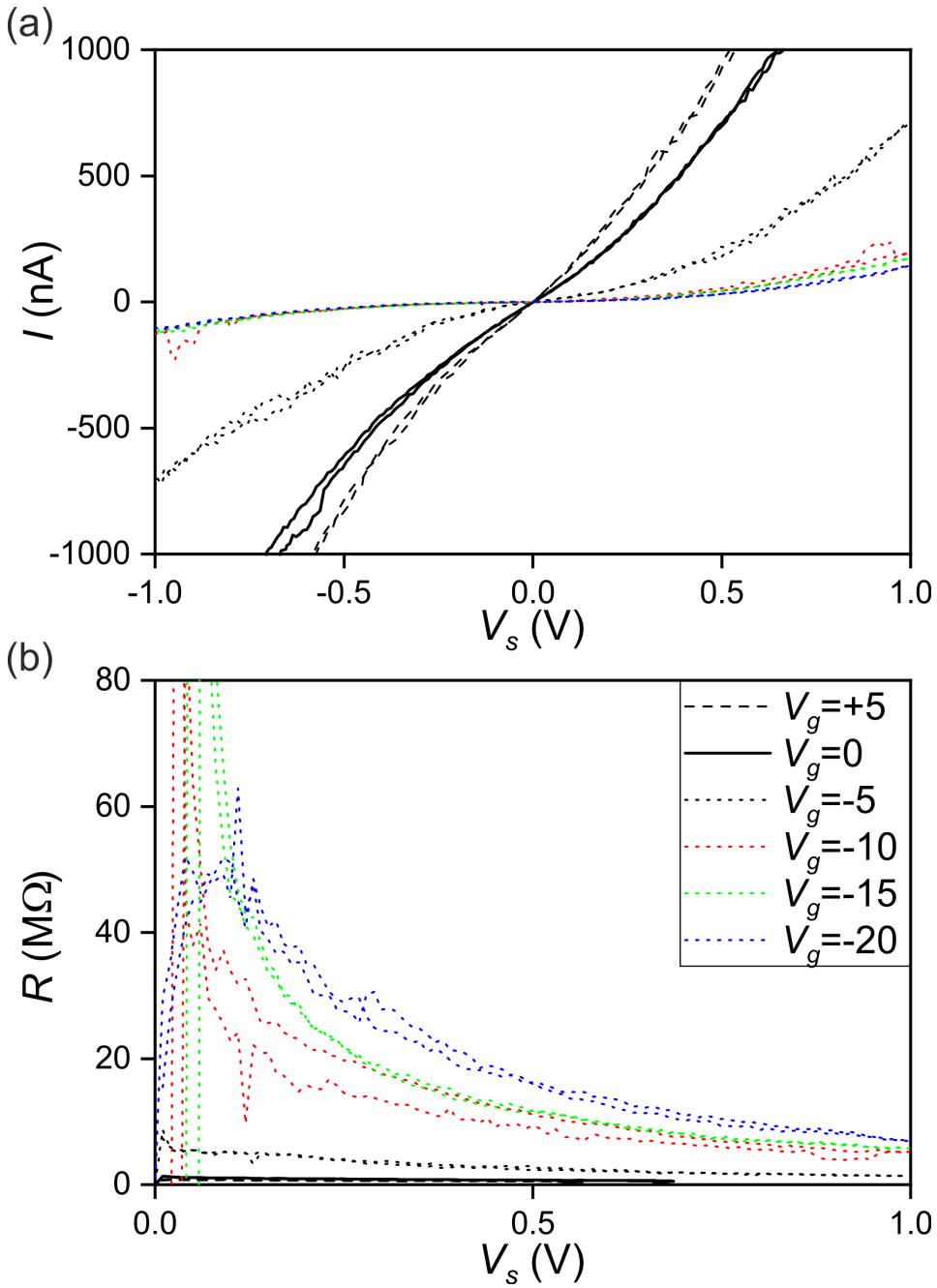

Figure 5.22: Room temperature results from a 30x30 μm cross sample. (a) IV curves with varying gate voltage and (b) RV curves for the same sample.

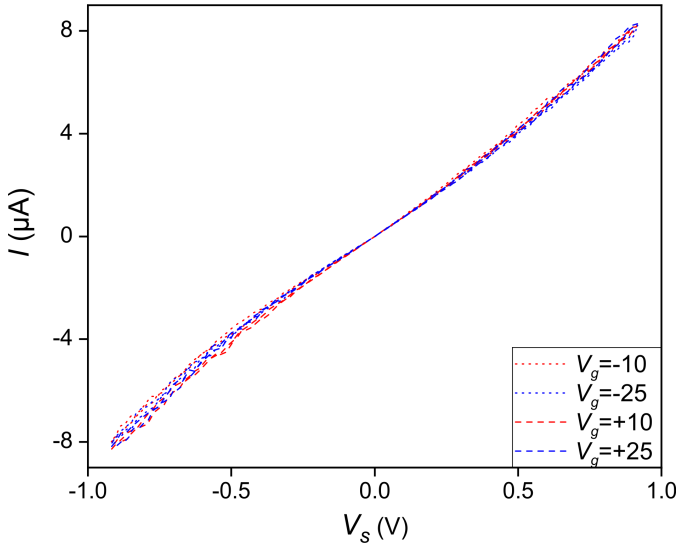

Figure 5.23: IV curves at room temperature when the varying gate voltage across a 15x15 μm cross sample.

Figure 5.23. However, the scale of this effect in relation to the currents observed is far smaller in the control sample, implying that the dependency on V_g is increased by the presence of the deposited molecules between graphene electrodes.

Analysing the dependence of R on V in Figure 5.22(b) shows a non-zero resistance peak. This is due to the effects of doping on the graphene electrodes as shown in Figure 5.24. The bottom graphene electrode is slightly p-doped due to the doping on the SiO_2 substrate used and the top graphene electrode is slightly n doped due to the wet etching process during the creation of the transfer stamp. Negative values of V_g also shift the R peak to higher values of V_s

Due to this, when $V_g = 0$ the bias voltage applied before reaching the peak is required to balance the chemical potentials of the two electrodes as in Figure 5.24(a). The resistance peaks when these are balanced as there are fewer available charge carrier states to be occupied in the second electrode (Figure 5.24(b)), before continuing the

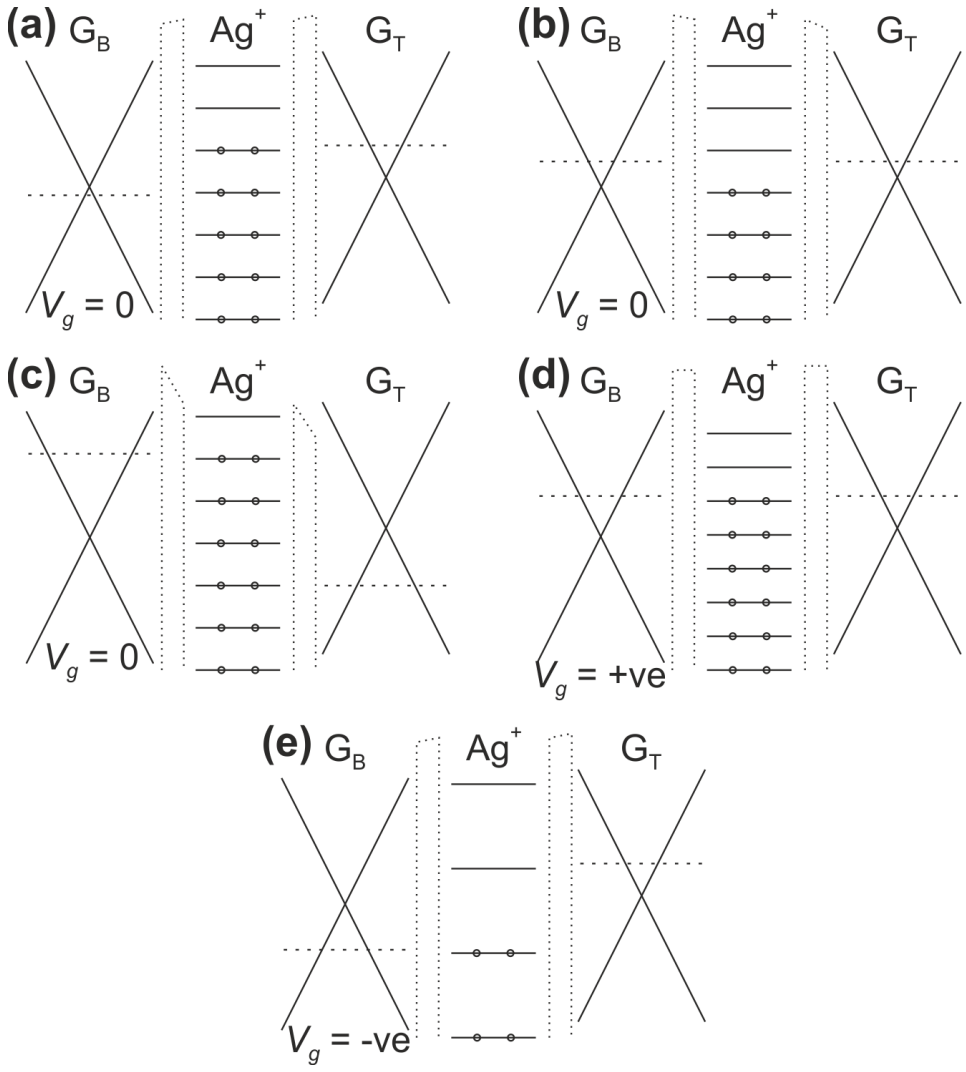

Figure 5.24: Energy level diagram across the of the sample under varying conditions. (a) Low bias voltage, (b) the high point of resistance and (c) high bias voltage for samples where $V_g = 0$. (d) A sample with a positive V_g at low bias voltage. (e) Similar with a negative V_g. Regions contained within the dotted lines are the tunnelling barriers and the dashed lines represent the Fermi energies of the graphene electrodes.

same as in Figure 5.21, shown with Figure 5.24(c). When a positive V_g is applied (Figure 5.24(d)), these two become more balanced until the potential in the bottom electrode is higher than that of the top electrode. Further, both are shifted to levels where there are more electron states available in the Ag^+ ion, decreasing the overall resistance. The reverse is true for negative values of V_g, as represented in Figure 5.24(e).

5.3 Conclusion

In this chapter, the synthesis of a novel electronic device has been described, followed by characterisation of the device and synthesis methods used. The presence and assembly of the tunnelling barrier has been confirmed through use of both Raman spectroscopy and XPS. The success of the top layer graphene transfer using a self-release polymer layer has been improved through multiple steps after identifying flaws in the method used.

Although the completed devices used were on rigid silicon dioxide substrates, the methods used in synthesis should be capable of reproducing such devices on flexible substrates such as polyethylene naphthalate (PEN) or cellulose acetate. While in need of confirmation, this should allow a wider range of applications such as strain sensing for these electronic devices.

High voltage results have shown the presence of a tunnelling barrier, which can be modelled as 5.9 eV in height and 1 nm in width when using a mass of 1 m_e. This remains consistent in both the low and intermediate ranges of Simmons' equations and fits with a possible barrier width when considering the size of molecules between the graphene layers. The barrier properties are similar, but slightly lower for smaller area samples, but larger area samples continue to have a lower resistance. Results at 77 K appear to have lower resistances due

to a changing alignment of the NDI-Py moieties.

Preliminary low voltage results show evidence of a possible Coulomb staircase, implying the presence of a Coulomb blockade within the device. More work is required to confirm if a Coulomb staircase is present both in the range examined and at lower bias voltages. In both the case of this and low temperature, high voltage measurements, more information could be acquired to obtain a deeper understanding by cooling the samples to even lower temperatures. Reducing the temperature to 4 K or similar would allow for a closer inspection and potential confirmation of the Coulomb effects and that the tunnelling resistance again increases once the moieties are flat. Another way to acquire more reliable data about a Coulomb blockade within the devices would be to use samples with smaller active areas where the top and bottom electrodes overlap.

Chapter 6

Conclusions and future work

6.1 Conclusions

This project has detailed the response of GSCs to a calibrated stress perturbation, as well as produced an analysis to aid in the modelling and design of future composite materials of a similar nature. Composite properties such as the viscoelastic creep time and the tunnel barrier height can be extracted by fitting the model to experimental results. The project has also begun progress on development of smaller scale multilayer devices consisting of graphene and adsorbed organic molecules with similar properties to overcome the limitations of GSC materials and for uses where GSCs are not appropriate. Initial results before probing the strain response have been acquired and the tunnel barrier properties extracted. Although the devices produced had limited success, a synthesis method has been developed to speed up production and allow for similarly structured devices of differing properties to be developed.

6.2 Future work

There are several areas in which the research covered in this thesis could be furthered. In this section, some of these suggestions are briefly discussed.

The GSC results could be compared to those using composites of differing mixtures. Some examples of modifications that could be made are altering the size of conducting particle inclusions or changing the silicone rubber in order to vary the parameters of the composite and compare these to the predictions of the model. Use of a matrix with more rigid bonds, such as fluorinated silicone, could alter the movement of the conducting particles and potentially raise the temperature at which the previously observed negative differential conductance region is observed.

In addition to testing the model on these new composites, it could be improved by adding terms to account for the breaking of conducting percolation lines through the material, allowing for a more accurate quantitative fit.

There are still many more things to be done with the multilayer devices. The presence of a Coulomb staircase has yet to be confirmed or ruled out. The current structure has yet to be tested on a flexible substrate for piezoresistance. Some modifications to the transfer process or use of a different device may be required to aid visibility and make this possible. Tests could also be carried out with varying the amount of NDI-Py deposited on the graphene electrodes to vary the tunnelling barrier width. Analysis of NDI-Py to determine its electronic properties would aid further investigations into the multilayer devices. Also, the effects on the IV curves when using lower temperatures such as 4 K or applying magnetic fields to the sample have yet to be explored. Finally, changing the moieties on the NDI molecules used may provide more desired effects in the sample, such as negative

differential conductance.

Bibliography

[1] S. Littlejohn, A. Nogaret, G. M. Prentice, and G. D. Pantos. Pressure sensing and electronic amplification with functionalized graphite-silicone composite. *Advanced Functional Materials*, 23(43):5398–5402, 2013.

[2] C. Y. Yan, J. X. Wang, W. B. Kang, M. Q. Cui, X. Wang, C. Y. Foo, K. J. Chee, and P. S. Lee. Highly stretchable piezoresistive graphene-nanocellulose nanopaper for strain sensors. *Advanced Materials*, 26(13):2022–2027, 2014.

[3] S. H. Bae, Y. Lee, B. K. Sharma, H. J. Lee, J. H. Kim, and J. H. Ahn. Graphene-based transparent strain sensor. *Carbon*, 51:236–242, 2013.

[4] J. Zhao, C. L. He, R. Yang, Z. W. Shi, M. Cheng, W. Yang, G. B. Xie, D. M. Wang, D. X. Shi, and G. Y. Zhang. Ultra-sensitive strain sensors based on piezoresistive nanographene films. *Applied Physics Letters*, 101(6), 2012.

[5] J. Zhao, G. L. Wang, R. Yang, X. B. Lu, M. Cheng, C. L. He, G. B. Xie, J. L. Meng, D. X. Shi, and G. Y. Zhang. Tunable piezoresistivity of nanographene films for strain sensing. *Acs Nano*, 9(2):1622–1629, 2015.

[6] A. D. Smith, F. Niklaus, A. Paussa, S. Vaziri, A. C. Fischer, M. Sterner, F. Forsberg, A. Delin, D. Esseni, P. Palestri,

M. Ostling, and M. C. Lemme. Electromechanical piezoresistive sensing in suspended graphene membranes. *Nano Letters*, 13(7):3237–3242, 2013.

[7] Ashok S. Chauhan, Isaac Taylor-Harrod, Samuel D. Littlejohn, and Alain Nogaret. Ultrafast pressure sensing with transient tunnelling currents. *Nanoscale*, 9(13):4544–4549, 2017.

[8] Samuel Littlejohn, Alain Nogaret, and Simon Crampin. Tunneling negative differential resistance in a flexible active composite. *Advanced Materials*, 23(25):2815–2818, 2011.

[9] Samuel Littlejohn and Alain Nogaret. *Negative Differential Resistance in Graphite-Silicone Polymer Composites*, volume 1399 of *AIP Conference Proceedings*. 2011.

[10] C. Grimaldi and I. Balberg. Tunneling and nonuniversality in continuum percolation systems. *Physical Review Letters*, 96(6):4, 2006.

[11] I. Balberg. Tunnelling and percolation in lattices and the continuum. *Journal of Physics D: Applied Physics*, 42(6):064003, 2009.

[12] G. Ambrosetti, C. Grimaldi, I. Balberg, T. Maeder, A. Danani, and P. Ryser. Solution of the tunneling-percolation problem in the nanocomposite regime. *Physical Review B*, 81(15):12, 2010.

[13] I. Balberg and S. Bozowski. Percolation in a composite of random stick-like conducting particles. *Solid State Communications*, 44(4):551–554, 1982.

[14] D. Toker, D. Azulay, N. Shimoni, I. Balberg, and O. Millo. Tunneling and percolation in metal-insulator composite materials. *Physical Review B*, 68(4), 2003.

[15] Sonia Vionnet-Menot, Claudio Grimaldi, Thomas Maeder, Sigfrid Strässler, and Peter Ryser. Tunneling-percolation origin of nonuniversality: theory and experiments. *Physical Review B*, 71(6):064201, 2005.

[16] L. Britnell, R. V. Gorbachev, A. K. Geim, L. A. Ponomarenko, A. Mishchenko, M. T. Greenaway, T. M. Fromhold, K. S. Novoselov, and L. Eaves. Resonant tunnelling and negative differential conductance in graphene transistors. *Nature Communications*, 4, 2013.

[17] Isaac Taylor-Harrod and Alain Nogaret. Piezoresistance of flexible tunneling-percolation networks. *Physical Review B*, 96(2):024205, 2017.

[18] Jamie H. Warner, Franziska Schäffel, Alicja Bachmatiuk, and Mark H. Rümmeli. *Graphene: Fundamentals and emergent applications*. Graphene. Elsevier, 1 edition, 2013.

[19] H. O. Pierson. *Handbook of Carbon, Graphite, Diamond and Fullerenes - Properties, Processing and Applications*. William Andrew Publishing/Noyes, 1993.

[20] P. Delhaes. *Polymorphism in Carbons and Parent Materials*, pages 3–27. Springer Netherlands, Dordrecht, 2001.

[21] J. D. Bernal. The structure of graphite. *Proceedings of the Royal Society A: Mathematical, Physical and Engineering Sciences*, 106(740):749–773, 1924.

[22] G. E. Bacon. Unit-cell dimensions of graphite. *Acta Crystallographica*, 3(2):137–139, 1950.

[23] Michio Inagaki. *New carbons control of structure and functions*. Amsterdam New York : Elsevier Science, Amsterdam New York, 1st ed. edition, 2000.

[24] S. S. Li, B. H. Northrop, Q. H. Yuan, L. J. Wan, and P. J. Stang. Surface confined metallosupramolecular architectures: Formation and scanning tunneling microscopy characterization. *Accounts of Chemical Research*, 42(2):249–259, 2009.

[25] K. Tahara, S. Furukawa, H. Uji-I, T. Uchino, T. Ichikawa, J. Zhang, W. Mamdouh, M. Sonoda, F. C. De Schryver, S. De Feyter, and Y. Tobe. Two-dimensional porous molecular networks of dehydrobenzo 12 annulene derivatives via alkyl chain interdigitation. *Journal of the American Chemical Society*, 128(51):16613–16625, 2006.

[26] S. Park, H. C. Floresca, Y. Suh, and M. J. Kim. Electron microscopy analyses of natural and highly oriented pyrolytic graphites and the mechanically exfoliated graphenes produced from them. *Carbon*, 48(3):797–804, 2010.

[27] J. Kintigh, B. Diaconescu, Y. Echegoyen, A. Busnaina, K. Pohl, and G. P. Miller. Hydrogenation and exfoliation of graphene using polyamine reagents. *Diamond and Related Materials*, 66:107–112, 2016.

[28] J. S. Y. Chia, M. T. T. Tan, P. S. Khiew, J. K. Chin, and C. W. Siong. A facile one-step green synthesis of graphene by mild solvent exfoliation. *Science of Advanced Materials*, 8(6):1177–1186, 2016.

[29] Ejikeme Raphael Ezeigwe, Chu Joon Sin, Poi Sim Khiew, Chiu Wee Siong, and Michelle T. T. Tan. Cobalt oxide nanoparticles grown on exfoliated graphene for enhanced electrochemical performance. *Materials Chemistry and Physics*, 183(Supplement C):56–64, 2016.

[30] J. C. Slonczewski and P. R. Weiss. Band structure of graphite. *Physical Review*, 109(2):272–279, 1958.

[31] J. C. Charlier, J. P. Michenaud, X. Gonze, and J. P. Vigneron. Tight-binding model for the electronic properties of simple hexagonal graphite. *Physical Review B*, 44(24):13237–13249, 1991.

[32] J. W. McClure. Electron energy band structure and electronic properties of rhombohedral graphite. *Carbon*, 7(4):425–+, 1969.

[33] B. Partoens and F. M. Peeters. From graphene to graphite: Electronic structure around the k point. *Physical Review B*, 74(7):11, 2006.

[34] A. Fasolino, J. H. Los, and M. I. Katsnelson. Intrinsic ripples in graphene. *Nature Materials*, 6:858, 2007.

[35] J. C. Meyer, A. K. Geim, M. I. Katsnelson, K. S. Novoselov, T. J. Booth, and S. Roth. The structure of suspended graphene sheets. *Nature*, 446(7131):60–63, 2007.

[36] L. Brey and H. A. Fertig. Electronic states of graphene nanoribbons studied with the dirac equation. *Physical Review B*, 73(23):235411, 2006.

[37] Verónica Barone, Oded Hod, and Gustavo E. Scuseria. Electronic structure and stability of semiconducting graphene nanoribbons. *Nano Letters*, 6(12):2748–2754, 2006.

[38] F. Ding, H. X. Ji, Y. H. Chen, A. Herklotz, K. Dorr, Y. F. Mei, A. Rastelli, and O. G. Schmidt. Stretchable graphene: A close look at fundamental parameters through biaxial straining. *Nano Letters*, 10(9):3453–3458, 2010.

[39] Yuanbo Zhang, Tsung-Ta Tang, Caglar Girit, Zhao Hao, Michael C. Martin, Alex Zettl, Michael F. Crommie, Y. Ron Shen, and Feng Wang. Direct observation of a widely tunable bandgap in bilayer graphene. *Nature*, 459:820, 2009.

[40] Edward McCann. *Electronic Properties of Monolayer and Bilayer Graphene*, page 237. 2012.

[41] D. C. Elias, R. R. Nair, T. M. G. Mohiuddin, S. V. Morozov, P. Blake, M. P. Halsall, A. C. Ferrari, D. W. Boukhvalov, M. I. Katsnelson, A. K. Geim, and K. S. Novoselov. Control of graphene's properties by reversible hydrogenation: Evidence for graphane. *Science*, 323(5914):610–613, 2009.

[42] Rahul R. Nair, Wencai Ren, Rashid Jalil, Ibtsam Riaz, Vasyl G. Kravets, Liam Britnell, Peter Blake, Fredrik Schedin, Alexander S. Mayorov, Shengjun Yuan, Mikhail I. Katsnelson, Hui-Ming Cheng, Wlodek Strupinski, Lyubov G. Bulusheva, Alexander V. Okotrub, Irina V. Grigorieva, Alexander N. Grigorenko, Kostya S. Novoselov, and Andre K. Geim. Fluorographene: A two-dimensional counterpart of teflon. *Small*, 6(24):2877–2884, 2010.

[43] S. H. Cheng, K. Zou, F. Okino, H. R. Gutierrez, A. Gupta, N. Shen, P. C. Eklund, J. O. Sofo, and J. Zhu. Reversible fluorination of graphene: Evidence of a two-dimensional wide bandgap semiconductor. *Physical Review B*, 81(20):205435, 2010.

[44] Xiaochen Dong, Dongliang Fu, Wenjing Fang, Yumeng Shi, Peng Chen, and Lain-Jong Li. Doping single-layer graphene with aromatic molecules. *Small*, 5(12):1422–1426, 2009.

[45] K. S. Novoselov, A. K. Geim, S. V. Morozov, D. Jiang, Y. Zhang, S. V. Dubonos, I. V. Grigorieva, and A. A. Firsov. Electric field effect in atomically thin carbon films. *Science*, 306(5696):666–669, 2004.

[46] Keith E. Whitener and Paul E. Sheehan. Graphene synthesis. *Diamond and Related Materials*, 46:25–34, 2014.

[47] Yenny Hernandez, Valeria Nicolosi, Mustafa Lotya, Fiona M. Blighe, Zhenyu Sun, Sukanta De, I. T. McGovern, Brendan Holland, Michele Byrne, Yurii K. Gun'Ko, John J. Boland, Peter Niraj, Georg Duesberg, Satheesh Krishnamurthy, Robbie Goodhue, John Hutchison, Vittorio Scardaci, Andrea C. Ferrari, and Jonathan N. Coleman. High-yield production of graphene by liquid-phase exfoliation of graphite. *Nature Nanotechnology*, 3:563, 2008.

[48] Jun Zhu. New solutions to a new problem. *Nature Nanotechnology*, 3:528, 2008.

[49] Cristina Vallés, Carlos Drummond, Hassan Saadaoui, Clascidia A. Furtado, Maoshuai He, Olivier Roubeau, Luca Ortolani, Marc Monthioux, and Alain Pénicaud. Solutions of negatively charged graphene sheets and ribbons. *Journal of the American Chemical Society*, 130(47):15802–15804, 2008.

[50] V. Singh, D. Joung, L. Zhai, S. Das, S. I. Khondaker, and S. Seal. Graphene based materials: Past, present and future. *Progress in Materials Science*, 56(8):1178–1271, 2011.

[51] H. Cheun Lee, Wei-Wen Liu, Siang-Piao Chai, Abdul Rahman Mohamed, Azizan Aziz, Cheng-Seong Khe, N. M. S. Hidayah, and U. Hashim. Review of the synthesis, transfer, characterization and growth mechanisms of single and multilayer graphene. *RSC Advances*, 7(26):15644–15693, 2017.

[52] Mark Hermann Rümmeli, Alicja Bachmatiuk, Felix Börrnert, Franziska Schäffel, Imad Ibrahim, Krzysztof Cendrowski, Grazyna Simha-Martynkova, Daniela Plachá, Ewa Borowiak-Palen, Gianaurelio Cuniberti, and Bernd Büchner. Synthesis of carbon nanotubes with and without catalyst particles. *Nanoscale Research Letters*, 6(1):303–303, 2011.

[53] C. Mattevi, H. Kim, and M. Chhowalla. A review of chemical vapour deposition of graphene on copper. *Journal of Materials Chemistry*, 21(10):3324–3334, 2011.

[54] T. Uchino, K. N. Bourdakos, C. H. de Groot, P. Ashburn, M. E. Kiziroglou, G. D. Dilliway, and D. C. Smith. Metal catalyst-free low-temperature carbon nanotube growth on sige islands. *Applied Physics Letters*, 86(23), 2005.

[55] S. M. Huang, Q. R. Cai, J. Y. Chen, Y. Qian, and L. J. Zhang. Metal-catalyst-free growth of single-walled carbon nanotubes on substrates. *Journal of the American Chemical Society*, 131(6):2094–+, 2009.

[56] A. Bachmatiuk, F. Borrnert, M. Grobosch, F. Schaffel, U. Wolff, A. Scott, M. Zaka, J. H. Warner, R. Klingeler, M. Knupfer, B. Buchner, and M. H. Rummeli. Investigating the graphitization mechanism of sio2 nanoparticles in chemical vapor deposition. *Acs Nano*, 3(12):4098–4104, 2009.

[57] A. Bachmatiuk, F. Borrnert, F. Schaffel, M. Zaka, G. S. Martynkowa, D. Placha, R. Schonfelder, Pmfj Costa, N. Ioannides, J. H. Warner, R. Klingeler, B. Buchner, and M. H. Rummeli. The formation of stacked-cup carbon nanotubes using chemical vapor deposition from ethanol over silica. *Carbon*, 48(11):3175–3181, 2010.

[58] Sukang Bae, Hyeongkeun Kim, Youngbin Lee, Xiangfan Xu, Jae-Sung Park, Yi Zheng, Jayakumar Balakrishnan, Tian Lei, Hye Ri Kim, Young Il Song, Young-Jin Kim, Kwang S. Kim, Barbaros Özyilmaz, Jong-Hyun Ahn, Byung Hee Hong, and Sumio Iijima. Roll-to-roll production of 30-inch graphene films for transparent electrodes. *Nature Nanotechnology*, 5:574, 2010.

[59] K. I. Bolotin, K. J. Sikes, Z. Jiang, M. Klima, G. Fudenberg, J. Hone, P. Kim, and H. L. Stormer. Ultrahigh electron mobility in suspended graphene. *Solid State Communications*, 146:351–355, 2008.

[60] Alfonso Reina, Hyungbin Son, Liying Jiao, Ben Fan, Mildred S. Dresselhaus, ZhongFan Liu, and Jing Kong. Transferring and identification of single- and few-layer graphene on arbitrary substrates. *The Journal of Physical Chemistry C*, 112(46):17741–17744, 2008.

[61] M. J. Allen, V. C. Tung, L. Gomez, Z. Xu, L. M. Chen, K. S. Nelson, C. W. Zhou, R. B. Kaner, and Y. Yang. Soft transfer printing of chemically converted graphene. *Advanced Materials*, 21(20):2098–2102, 2009.

[62] Joshua D. Caldwell, Travis J. Anderson, James C. Culbertson, Glenn G. Jernigan, Karl D. Hobart, Fritz J. Kub, Marko J. Tadjer, Joseph L. Tedesco, Jennifer K. Hite, Michael A. Mastro, Rachael L. Myers-Ward, Charles R. Eddy, Paul M. Campbell, and D. Kurt Gaskill. Technique for the dry transfer of epitaxial graphene onto arbitrary substrates. *ACS Nano*, 4(2):1108–1114, 2010.

[63] Sang Yoon Yang, Joong Gun Oh, Dae Yool Jung, HongKyw Choi, Chan Hak Yu, Jongwoo Shin, Choon-Gi Choi, Byung Jin Cho, and Sung-Yool Choi. Metal-etching-free direct delamination and transfer of single-layer graphene with a high degree of freedom. *Small*, 11(2):175–181, 2015.

[64] J. Y. Choi. Graphene transfer a stamp for all substrates. *Nature Nanotechnology*, 8(5):311–312, 2013.

[65] Jie Song, Fong-Yu Kam, Rui-Qi Png, Wei-Ling Seah, Jing-Mei Zhuo, Geok-Kieng Lim, Peter K. H. Ho, and Lay-Lay Chua. A

general method for transferring graphene onto soft surfaces. *Nat Nano*, 8(5):356–362, 2013.

[66] Moon Kee Choi, Inhyuk Park, Dong Chan Kim, Eehyung Joh, Ok Kyu Park, Jaemin Kim, Myungbin Kim, Changsoon Choi, Jiwoong Yang, Kyoung Won Cho, Jae-Ho Hwang, Jwa-Min Nam, Taeghwan Hyeon, Ji Hoon Kim, and Dae-Hyeong Kim. Thermally controlled, patterned graphene transfer printing for transparent and wearable electronic/optoelectronic system. *Advanced Functional Materials*, 25(46):7109–7118, 2015.

[67] X. L. Liang, B. A. Sperling, I. Calizo, G. J. Cheng, C. A. Hacker, Q. Zhang, Y. Obeng, K. Yan, H. L. Peng, Q. L. Li, X. X. Zhu, H. Yuan, A. R. H. Walker, Z. F. Liu, L. M. Peng, and C. A. Richter. Toward clean and crackless transfer of graphene. *Acs Nano*, 5(11):9144–9153, 2011.

[68] M. Bousa, M. Kalbac, I. Jirka, L. Kavan, and O. Frank. Experimental study of pib-based cvd graphene transfer efficiency, 2015.

[69] Franz Schwabl. *Quantum Mechanics*. Springer Berlin Heidelberg: Berlin, Heidelberg, Berlin, Heidelberg, 2007.

[70] J. G. Simmons. Low-voltage current-voltage relationship of tunnel junctions. *Journal of Applied Physics*, 34(1):238–239, 1963.

[71] J. G. Simmons and G. J. Unterkofler. Potential barrier shape determination in tunnel junctions. *Journal of Applied Physics*, 34(6):1828–1830, 1963.

[72] J. G. Simmons. Generalized formula for electric tunnel effect between similar electrodes separated by a thin insulating film. *Journal of Applied Physics*, 34(6):1793–1803, 1963.

[73] J. G. Simmons. Electric tunnel effect between dissimilar electrodes separated by a thin insulating film. *Journal of Applied Physics*, 34(9):2581–2590, 1963.

[74] E. L. Murphy and R. H. Good. Thermionic emission, field emission, and the transition region. *Physical Review*, 102(6):1464–1473, 1956.

[75] C. H. Shang, J. Nowak, R. Jansen, and J. S. Moodera. Temperature dependence of magnetoresistance and surface magnetization in ferromagnetic tunnel, junctions. *Physical Review B*, 58(6):R2917–R2920, 1998.

[76] D. A. G. Bruggeman. Berechnung verschiedener physikalischer konstanten von heterogenen substanzen. i. dielektrizitätskonstanten und leitfähigkeiten der mischkörper aus isotropen substanzen. *Annalen der Physik*, 416(7):636–664, 1935.

[77] R. Landauer. The electrical resistance of binary metallic mixtures. *Journal of Applied Physics*, 23(7):779–784, 1952.

[78] D. C. Pham and S. Torquato. Strong-contrast expansions and approximations for the effective conductivity of isotropic multiphase composites. *Journal of Applied Physics*, 94(10):6591–6602, 2003.

[79] M. Sahimi, B. D. Hughes, L. E. Scriven, and H. T. Davis. Real-space renormalization and effective-medium approximation to the percolation conduction problem. *Physical Review B*, 28(1):307–311, 1983.

[80] F. Thiel and I. M. Sokolov. Effective-medium approximation for lattice random walks with long-range jumps. *Physical Review E*, 94(1), 2016.

[81] D. J. Bergman and Y. M. Strelniker. Magnetotransport in conducting composite films with a disordered columnar microstructure and an in-plane magnetic field. *Physical Review B*, 60(18):13016–13027, 1999.

[82] D. Stroud. The effective medium approximations: Some recent developments. *Superlattices and Microstructures*, 23(3-4):567–573, 1998.

[83] Scott Kirkpatrick. Percolation and conduction. *Reviews of Modern Physics*, 45(4):574–588, 1973.

[84] E. Thommerel, J. C. Valmalette, J. Musso, S. Villain, J. R. Gavarri, and D. Spada. Relations between microstructure, electrical percolation and corrosion in metal-insulator composites. *Materials Science and Engineering a-Structural Materials Properties Microstructure and Processing*, 328(1-2):67–79, 2002.

[85] N. Johner, P. Ryser, C. Grimaldi, and I. Balberg. Piezoresistivity and tunneling-percolation transport in apparently nonuniversal systems. *Physical Review B*, 75(10), 2007.

[86] G. E. Pike and C. H. Seager. Percolation and conductivity - computer study 1. *Physical Review B*, 10(4):1421–1434, 1974.

[87] A. L. Efros and B. I. Shklovskii. Critical behavior of conductivity and dielectric-constant near metal-non-metal transition threshold. *Physica Status Solidi B-Basic Research*, 76(2):475–485, 1976.

[88] Junjie Wu and D. S. McLachlan. Percolation exponents and thresholds obtained from the nearly ideal continuum percolation system graphite-boron nitride. *Physical Review B*, 56(3):1236–1248, 1997.

[89] I. Balberg. Limits on the continuum-percolation transport exponents. *Physical Review B*, 57(21):13351–13354, 1998.

[90] I. Balberg. Tunneling and nonuniversal conductivity in composite-materials. *Physical Review Letters*, 59(12):1305–1308, 1987.

[91] N. L. Lavrik and V. P. Voloshin. Calculation of mean distances between the randomly distributed particles in the model of points and hard spheres (the method of voronoi polyhedra). *The Journal of Chemical Physics*, 114(21):9489–9491, 2001.

[92] G. Ambrosetti, N. Johner, C. Grimaldi, T. Maeder, P. Ryser, and A. Danani. Electron tunneling in conductor-insulator composites with spherical fillers. *Journal of Applied Physics*, 106(1):016103, 2009.

[93] Alchemie Ltd. Technical data sheet alchemix rtv 137, 2014.

[94] M. Ohring. *The Materials Science of Thin Films*. 2002.

[95] S. C. Hunter. *Mechanics of continuous media*. Chichester : Ellis Horwood, Chichester New York London, 1976.

[96] Samuel Littlejohn. *Electrical Properties of Graphite Nanoparticles in Silicone: Flexible Oscillators and Electromechanical Sensing*. Thesis, 2012.

[97] Y. Gu, X. W. Wang, W. Gu, Y. J. Wu, T. Li, and T. Zhang. Flexible electronic eardrum. *Nano Research*, 10(8):2683–2691, 2017.

[98] J. Tolvanen, J. Hannu, and H. Jantunen. Hybrid foam pressure sensor utilizing piezoresistive and capacitive sensing mechanisms. *Ieee Sensors Journal*, 17(15):4735–4746, 2017.

[99] S. Gong, W. Schwalb, Y. W. Wang, Y. Chen, Y. Tang, J. Si, B. Shirinzadeh, and W. L. Cheng. A wearable and highly sensitive pressure sensor with ultrathin gold nanowires. *Nature Communications*, 5:8, 2014.

[100] P. M. Kogut and J. P. Straley. The bicritical macroscopic conductivity exponent in dimensionalities two, three and infinity. *Journal of Physics C: Solid State Physics*, 12(1):1, 1979.

[101] B. L. Lu and S. Torquato. Nearest-surface distribution-functions for polydispersed particle-systems. *Physical Review A*, 45(8):5530–5544, 1992.

[102] S. Torquato, B. Lu, and J. Rubinstein. Nearest-neighbor distribution-functions in many-body systems. *Physical Review A*, 41(4):2059–2075, 1990.

[103] A. A. Barlian, W. T. Park, J. R. Mallon, A. J. Rastegar, and B. L. Pruitt. Review: Semiconductor piezoresistance for microsystems. *Proceedings of the Ieee*, 97(3):513–552, 2009.

[104] A. Dehe, K. Fricke, K. Mutamba, and H. L. Hartnagel. A piezoresistive gaas pressure sensor with gaas/algaas membrane technology. *Journal of Micromechanics and Microengineering*, 5(2):139–142, 1995.

[105] E. Ungersboeck, S. Dhar, G. Karlowatz, V. Sverdlov, H. Kosina, and S. Selberherr. The effect of general strain on the band structure and electron mobility of silicon. *Ieee Transactions on Electron Devices*, 54(9):2183–2190, 2007.

[106] T. J Lyon, J. Sichau, A. Dorn, A. Centeno, A. Pesquera, A. Zurutuza, and R. H Blick. Probing electron spin resonance in monolayer graphene. *Physical Review Letters*, 119(6):066802, 2017.

[107] Y. Tsukada, K. Hirao, and J. Mizuguchi. N,n '-bis 2-(4-pyridyl)ethyl naphthalene-1,8 : 4,5-bis(dicarboximide). *Acta Crystallographica Section E-Structure Reports Online*, 63:O3872–U3600, 2007.

[108] A. C. Ferrari, J. C. Meyer, V. Scardaci, C. Casiraghi, M. Lazzeri, F. Mauri, S. Piscanec, D. Jiang, K. S. Novoselov, S. Roth, and A. K. Geim. Raman spectrum of graphene and graphene layers. *Physical Review Letters*, 97, 2006.

[109] C. Casiraghi, S. Pisana, K. S. Novoselov, A. K. Geim, and A. C. Ferrari. Raman fingerprint of charged impurities in graphene. *Applied Physics Letters*, 91(23):3, 2007.

[110] I. E. Itskevich, T. Ihn, A. Thornton, M. Henini, T. J. Foster, P. Moriarty, A. Nogaret, P. H. Beton, L. Eaves, and P. C. Main. Resonant magnetotunneling through individual self-assembled inas quantum dots. *Physical Review B*, 54(23):16401–16404, 1996.

[111] Daeha Joung, Lei Zhai, and Saiful I. Khondaker. Coulomb blockade and hopping conduction in graphene quantum dots array. *Physical Review B*, 83(11):115323, 2011.

[112] Lorcan J. Brennan, Finn Purcell-Milton, Barry McKenna, TrystanM Watson, Yurii K. Gun'ko, and Rachel C. Evans. Large area quantum dot luminescent solar concentrators for use with dye-sensitised solar cells. *Journal of Materials Chemistry A*, 6(6):2671–2680, 2018.

[113] Shinya Kano, Tsukasa Tada, and Yutaka Majima. Nanoparticle characterization based on stm and sts. *Chemical Society Reviews*, 44(4):970–987, 2015.